



People's Democratic Republic of Algeria
Ministry of Higher Education and Scientific Research
Frères Mentouri Constantine 1 University
Faculty of Technology Sciences
Department of Electronics

Order N°:

Series:

A Thesis

**Submitted in Partial Fulfillment of the Requirements for
the Degree of Doctorat Troisième Cycle in
Electronics**

Option: Signaux et Systèmes de Télécommunication

THEME

**Modélisation et Estimation des Paramètres d'un Fouillis
Non-Gaussien**

By

Nouh GUIDOUM

Committee Members:

Chairman:	Atef FARROUKI	<i>Prof.</i>	Université des Frères Mentouri Constantine 1
Supervisor:	Faouzi SOLTANI	<i>Prof.</i>	Université des Frères Mentouri Constantine 1
Examiners:	Abdelfatah CHAREF	<i>Prof.</i>	Université des Frères Mentouri Constantine 1
	Tarek FORTAKI	<i>Prof.</i>	Université Batna 2
	Khaled BELARBI	<i>Prof.</i>	Ecole Nationale Polytechnique de Constantine

Acknowledgment

In the Name of Allah, the Most Gracious and the Most Merciful

First and foremost, all praises to **Allah** for giving me the opportunity, ability, strength, and motivation to accomplish this work. I faced a lot of difficulties, not only on the academic side but also on the personality side, without you, my **Allah**, this thesis would not have seen the light.

Second, I would like to sincerely thank my supervisor **Prof. Faouzi SOLTANI** for his guidance, understanding, patience and most importantly, he has provided positive encouragement and a warm spirit to finish this thesis. I have benefited greatly from his extensive knowledge and valuable advice. It has been a great pleasure and honor for me to be under his supervision. I would like to thank and express my special gratitude to **Prof. Amar MEZACHE**, **Dr. Souad CHABBI**, **Dr. Amel AISSAOUI**, **Prof. Atef FARROUKI**, **Prof. Mohamed Taoufik BENHABILES**, **Prof. Zoheir HAMMOUDI** and **Prof. Toufik LAROUSSE**, for their valuable advice and support throughout the work period, "may **Allah** bless you and give you more success and happiness throughout your life".

I would also like to thank the committee members, **Prof. Atef FARROUKI**, Frères Mentouri Constantine 1 University, **Prof. Abdelfatah CHAREF**, Frères Mentouri Constantine 1 University, **Prof. Tarek FORTAKI**, Université Batna 2 and **Prof. Khaled BELARBI**, Ecole Nationale Polytechnique de Constantine, who agreed to be the examiners of this thesis and whose remarks and comments will certainly allow me to improve the quality of this thesis.

Dedications

With Deep Gratitude and Sincere Words

This thesis is sincerely dedicated to my dear parents "**Boudjemaa and Fatima Zohra SEGHRAOUI**", who were my inspiration and gave me the strength when I thought about giving up, who continuously provide their moral, spiritual, emotional, and financial support. Thank you both for giving me the strength to make my dream come true.

This thesis is also dedicated to my sisters "**Khadidja**" and "**Nousseiba**", my brother "**Brahim**" and his wife "**Imen KERMICHE**", my dear uncle "**Abd al Hafid SEGHRAOUI**", my dear grandfather "**Mohamed Tahar GUIDOUM**", may "**Allah**" have mercy on him. Finally, to all the family, friends and to all those who are dear to me.

Abstract

Accurate detection of maritime targets in all adverse weather conditions requires detailed knowledge and a correct understanding of the signals reflected by the sea surface and its environment. The first objective proposed in this thesis is to find a statistical model that accurately describes the behavior of the intensive sea echo "Clutter", and provides a precise long tail. Under this context, two approximate Weibull models with thermal noise are proposed to describe high-resolution sea clutter. For the first model, we derive the expressions of the PDF and CCDF for single and multiple pulses. For the second model, we also derive the expression of the CCDF for single as well as multiple pulses. In addition, we provide the formula of the moments. The parameters estimation for each model is conducted using the PCFE method of the CCDF function based on the N-M algorithm. The simulations were carried out on synthesized sea data as well as on real sea data collected by the McMaster IPIX radar. All the results obtained from synthesized and real IPIX data with a different range resolution (60, 30, 15, 9, and 3 meters) and different polarization modes (HH, VV, HV, and VH) confirmed that the proposed models provide the best-fit performance for sea data, especially in the tail regions, outperforming the CG models with additive thermal noise in most cases. The second work in this thesis is based on the mixture of a proposed Weibull models. In all cases studied, the proposed model provides an accurate fit to the actual IPIX sea data and shows a precise tail, outperforming the mixture of the CG models. Finally, in the context of maritime radar detection, two novel CFAR detectors are suggested for Weibull and CG models with the presence of thermal noise and interfering targets. The proposed detectors have been studied on the basis of synthesized data and real IPIX data. All the results show a high probability of detection as well as an excellent false alarm rate regulation, especially in the case of the presence of spiky clutter.

ملخص

يتطلب الاكتشاف الدقيق للأهداف البحرية في جميع الظروف الجوية السيئة معرفة مفصلة وفهمًا صحيحًا للإشارات المنعكسة من سطح البحر ومحيطه. الهدف الأول المقترح في هذه الأطروحة هو إيجاد نموذج إحصائي يصف بدقة سلوك فوضى البحر المكثف (Clutter)، ويوفر ذيلًا طويلًا دقيقًا. تحت هذا السياق، تم اقتراح نموذجين تقريبيين من Weibull مع وجود الضوضاء الحرارية لوصف فوضى البحر عالية الدقة. بالنسبة للنموذج الأول، نشق تعبيرات PDF و CCDF للنبضة الأحادية والمتعددة. بالنسبة للنموذج الثاني، نشق أيضًا تعبير CCDF للنبضة الأحادية والمتعددة، بالإضافة إلى ذلك، نقدم معادلة اللحظات. يتم إجراء تقدير المعلمات لكل نموذج باستخدام طريقة PCFE لوظيفة CCDF بناءً على خوارزمية N-M. تم إجراء عمليات المحاكاة على بيانات بحرية مركبة بالإضافة إلى بيانات بحرية حقيقية تم جمعها بواسطة رادار McMaster IPIX. أكدت جميع النتائج التي تم الحصول عليها من البيانات المركبة ومن البيانات IPIX الحقيقية مع دقة مختلفة المدى (30، 60، 9، 15، 3 متر) ووضع استقطاب مختلف (VH، HV، HH، VV) أن النماذج المقترحة توفر أفضل ملائمة للبيانات البحرية، خاصة في منطقة الذيل، متوقعة على نماذج CG مع الضوضاء الحرارية في معظم الحالات. يعتمد العمل الثاني في هذه الأطروحة على دمج نماذج Weibull المقترحة. في جميع الحالات التي تمت دراستها، يوفر النموذج المقترح ملائمة دقيقة للبيانات البحرية الحقيقية ويظهر ذيلًا دقيقًا متفوقًا على نماذج CG المدمجة. في سياق كشف الرادار البحري غير المتناسق، تم اقتراح جهازي كشف CFAR جديدين لنماذج Weibull و CG مع وجود الضوضاء الحرارية والأهداف المتداخلة. تمت دراسة الكواشف المقترحة على أساس البيانات المركبة وبيانات IPIX الحقيقية. تظهر جميع النتائج احتمالية عالية للكشف بالإضافة إلى تنظيم ممتاز لمعدل الإنذار الخاطئ خاصة في حالة وجود فوضى الشائكة.

Résumé

La détection précise des cibles maritimes dans toutes les conditions météorologiques défavorables nécessite des connaissances détaillées et une compréhension correcte des signaux réfléchis par la surface de la mer et de son environnement. Le premier objectif proposé dans cette thèse est de trouver un modèle statistique qui décrit avec précision le comportement de l'écho marin intensif "Fouillis" et qui fournit une longue queue précise. Dans ce contexte, deux modèles approximatifs de Weibull avec le bruit thermique sont proposés pour décrire le fouillis maritime à haute résolution. Pour le premier modèle, nous obtenons les expressions de la fonction de PDF et de la CCDF pour une impulsion et des impulsions multiples. Pour le deuxième modèle, nous obtenons également l'expression du CCDF pour une impulsion et des impulsions multiples. De plus, nous fournissons la formule des moments. L'estimation des paramètres pour chaque modèle est réalisée à l'aide de la méthode PCFE de la fonction CCDF basée sur l'algorithme N-M. Les simulations ont été réalisées sur des données maritime synthétiques ainsi que sur des données maritime réelles collectées par le radar McMaster IPIX. Tous les résultats obtenus à partir de données synthétiques et de données IPIX réelles avec différentes plages de résolution (60, 30, 15, 9 et 3 mètres) et différent mode de polarisation (HH, VV, HV et VH) ont confirmé que les modèles proposées offrent le meilleur ajustement pour les données maritimes, en particulier dans les régions de la queue, surpassant les modèles CG avec un bruit thermique additif dans la plupart des cas. Le deuxième travail de cette thèse est basé sur une combinaison des modèles de Weibull proposées. Dans tous les cas étudiés, le modèle proposé fournit un ajustement précis aux données marines réelles IPIX et montre une queue précise, surpassant la combinaison des modèles CG. Enfin, dans le cadre de la détection radar maritime, deux nouveaux détecteurs CFAR non-cohérents sont proposés pour les modèles Weibull et CG avec la présence du bruit thermique et des cibles parasites. Les deux détecteurs proposés ont été étudiés sur la base de données synthétisées et de données IPIX réelles. Tous les résultats montrent une forte probabilité de détection ainsi qu'une excellente régulation du taux de fausses alarmes, en particulier dans le cas de la présence de fouillis intense.

Contents

Abstract	iii
List of Abbreviations	ix
List of Symbols	xi
List of Figures	xiii
List of Tables	xviii
1 General Introduction	1
1.1 Introduction	2
1.2 Motivations and Contributions	3
1.2.1 Clutter Modeling	3
1.2.2 CFAR Detection in Maritime Environment	4
1.3 Thesis Organization	4
2 Radar Concept	5
2.1 Radar Basics	6
2.2 Detection Process	7
2.3 Information Extracted From the Radar Echo	7
2.3.1 Range	8
2.3.2 Radial Velocity	8
2.3.3 Angular Direction	9
2.4 Radar Cross Section	9
2.5 Radar Equation Form	10
2.6 Types of Radar Systems	12
2.6.1 Classification by Frequency Band	12
2.6.2 Classification by Waveform and Pulse Rate	13
2.6.3 Primary and Secondary Surveillance Radar	14
2.6.4 Monostatic, Bistatic, Multistatic and MIMO Radar	14
2.6.5 Tracking and Acquisition Radar	15
2.6.6 Instrumentation Radar	15
2.6.7 Synthetic Aperture Radar	16

2.6.8	Weather Radar	16
2.6.9	Maritime Navigation Radar	17
2.7	Radar Clutter	18
2.8	Sea Clutter	19
2.8.1	Sea Surface	20
2.8.2	Sea Clutter Reflectivity	21
2.9	Sea Clutter Modeling	22

3 Modeling of High-Resolution Radar Sea Clutter Using Two Approximate Weibull

	Distributions plus Thermal Noise	25
3.1	Introduction	26
3.2	Generalized Compound Model without Thermal Noise	27
3.2.1	R Distribution	29
3.2.2	E Distribution	29
3.2.3	K Distribution	30
3.2.4	Γ Distribution	30
3.2.5	$G\Gamma$ Distribution	30
3.2.6	GK Distribution	31
3.2.7	W Distribution	31
3.2.8	WG Distribution	32
3.2.9	LN Distribution	32
3.2.10	GH Distribution	33
3.3	Generalized Compound Model with Thermal Noise	35
3.4	First Weibull Model plus Thermal Noise	35
3.4.1	The WN1 Model for a Single Pulse	35
3.4.2	The WN1 Model for Multiple Pulse	36
3.5	Second Weibull Model plus Thermal Noise	36
3.5.1	The WN2 Model for Single Pulse	37
3.5.2	The WN2 Model for Multiple Pulse	37
3.5.3	The Compound Gaussian plus Noise Models	38
3.6	Simulation Results and Discussions	39
3.6.1	Parameter Estimation by the PCFE Method	39
3.6.1.1	The MSE Criterion	40
3.6.1.2	The CS Criterion	40
3.6.2	Fitting via Synthetic Data	41
3.6.3	Modeling Using Real Sea IPIX Data	43
3.6.3.1	Range Resolutions 60, 30 and 15m	45
3.6.3.2	Range Resolutions 9 and 3m	55
3.7	Conclusions	66

4	Sea Clutter Modeling Using Mixtures of Two Approximate Weibull Distributions plus Thermal Noise	67
4.1	Introduction	68
4.2	Mixture Models	68
4.2.1	Mixture of WN1 and WN2 Model for Single Pulse	69
4.2.2	Mixture of WN1 and WN2 Model for Multiple Pulse	69
4.2.3	Mixture of The Compound Gaussian plus Noise Models	70
4.3	Simulation Results and Discussions	71
4.3.1	Range Resolutions 60, 30 and 15m	71
4.3.2	Range Resolutions 9, and 3m	78
4.4	Conclusions	84
5	Two Novel Radar Detectors for Spiky Sea Clutter With the Presence of Thermal Noise and Interfering Targets	85
5.1	Introduction	86
5.2	Radar Hypothesis Test and CFAR Detectors	86
5.3	Proposed Detectors: The Var-Max-Min Detector and The Max-Min Detector	89
5.4	Simulation Results and Discussions	90
5.4.1	False Alarm Regulation	90
5.4.2	False Alarm Regulation in the Presence of Two Interfering Targets .	94
5.4.3	Probability of Detection	97
5.4.4	Experimental Results Using Real Sea IPIX Data	102
5.5	Conclusions	105
6	General Conclusions	106
6.1	Summary and Main Results	107
6.2	Perspectives and Future Work	108
	Bibliography	109

List of Abbreviations

AMTI	Airborne MTI
BMNS	British Meteorological Navy Service
CFAR	Constant False Alarm Rate
CNR	Clutter-to-Noise Ratio
CUT	Cell Under Test
CIG	Compound Inverse Gaussian
CDF	Cumulative Distributed Function
CCDF	Complementary CDF
CG	Compound Gaussian
CA-CFAR	Cell-Averaging CFAR
CS-CFAR	Censored CFAR
CW	Continuous Wave
DSTO	Defense Science Technology Organization
FMCW	Frequency Modulated Continuous Wave
GP	Generalized Pareto
$G\Gamma$	Generalized gamma
GO-CFAR	Greatest-Of CFAR
GC	Generalized Compound
GH	Generalized Hyper-Geometric
GHz	Giga Hertz
HF	High Frequency Hertz
IPIX	Intelligent PIXel processing X-band
IF	Intermediate Frequency
ICR	Interfering-to-Clutter Ratio
IID	Identically and Independent Distributed
IRF	Inter Pulse Frequency

MSE	Mean Square Error
MLE	Maximum Likelihood Estimate
N-M	Nelder-Mead
MTI	Moving Target Indication
MIMO	Multiple Input Multiple Output
NP	Neyman Pearson
NRL	Naval Research Laboratory
OS-CFAR	Order Statistics CFAR
PCFE	Parametric Curve Fitting Estimation
PDF	Probability Density Function
PFA	Probability of False Alarm
PD	Probability of Detection
PRF	Pulse Repetition Frequency
PSR	Primary Surveillance Radar
PRF	Pulse Repetition Frequency
RADAR	RADio Detection And Ranging
RCS	Radar Cross Section
SNR	Signal to Noise Ratio
SCR	Signal-to-Clutter Ratio
SO-CFAR	Smallest-Of CFAR
STAP	Space-Time Adaptive Processing
SSR	Secondary Surveillance Radar
SAR	Synthetic Aperture Radar
T/R	Transmitter/Receiver
TM	Trimmed Mean
US	United States
UHF	Ultra High Frequency
VHF	Very High Frequency
WMO	World Meteorological Organization
WSR	Weather Surveillance Radar

List of Symbols

Chapter 2

R	Range
c	Speed of light
σ	Target cross section
E_i	The incident electric field strength at target
P_t	Transmitted power
\hat{P}	Power density
P_r	Received Power
G	Antenna gain
R_{max}	Maximum radar range
A_e	Antenna effective aperture
τ	Pulse width
σ^0	Area reflectivity

Chapter 3 and 4

a	Scale parameter of the GC distribution
$v_{1,2}$	Shape parameters of the GC distribution
$b_{1,2}$	Power parameters of the generalized gamma GF
$K_{\nu,1}(2cx)$	Modified Bessel function
${}_pF_q$	Generalized Hyper-geometric functions
β	Scale parameter of the Weibull, WN1, and WN2 models
c	Shape parameter of the Weibull, WN1, and WN2 models
b	Scale parameter of the K-distribution
ν	Shape parameter of the K-distribution
α	Shape parameter of the Generalized Pareto distribution
b	Scale parameter of the Generalized Pareto distribution
λ	Shape parameter of the inverse Gaussian distribution
μ	Mean power of the inverse Gaussian distribution
$\hat{\cdot}$	Estimated parameter

n	Moment's order
N	Number of integrated pulses
σ	Standard deviation
p_n	Noise power
T	Detection threshold
P_{FA}	Probability of False Alarm
θ	Vector of unknown parameters
K	Weighting factor

Chapter 5

H_0, H_1	Binary Hypothesis
T_h	Detection threshold
P_{FA}	Probability of False Alarm
P_D	Probability of Detection
P_M	Probability of miss
b	Scale parameter of the K-distribution
ν	Shape parameter of the K-distribution
λ	Shape parameter of the inverse Gaussian distribution
μ	Mean power of the inverse Gaussian distribution
σ	Standard deviation
p_n	Noise power

List of Figures

2.1	Principle of a radar system.	6
2.2	Train of transmitted and received pulses.	13
2.3	Sea radar scan and various sources of clutter.	19
3.1	Special cases of GC PDF and existing clutter models.	26
3.2	CCDF curves via synthetic data for CNR = -5 dB, $c = 1$, $\beta = 0.3466$ and $p_n = 1.1543$	41
3.3	PDF curves via synthetic data for CNR = -5 dB and $c = 1$, $\beta = 0.3466$ and $p_n = 1.1543$	42
3.4	CCDF curves via synthetic data for CNR = 10 dB and $c = 1$, $\beta = 0.6742$ and $p_n = 0.0165$	42
3.5	PDF curves via synthetic data for CNR = 10 dB and $c = 1$, $\beta = 0.6742$ and $p_n = 0.0165$	43
3.6	CCDF curves, 60m, HH polarization, 4 th range cell, Azimuth resolution = 0.3571°	45
3.7	PDF curves, 60m, HH polarization, 4 th range cell, Azimuth resolution = 0.3571°	46
3.8	CCDF curves, 60m, VV polarization, 4 th range cell, Azimuth resolution = 0.3571°	46
3.9	PDF curves, 60m, VV polarization, 4 th range cell, Azimuth resolution = 0.3571°	47
3.10	CCDF curves, 30m, HH polarization, 20 th range cell, Azimuth resolution = 16.1499°	48
3.11	PDF curves, 30m, HH polarization, 20 th range cell, Azimuth resolution = 16.1499°	48
3.12	CCDF curves, 30m, VV polarization, 6 th range cell, Azimuth resolution = 16.1499°	49
3.13	PDF curves, 30m, VV polarization, 6 th range cell, Azimuth resolution = 16.1499°	49
3.14	CCDF curves, 15m, HH polarization, 18 th range cell, Azimuth resolution = 0.2966°	51

3.15 PDF curves, 15m, HH polarization, 18 th range cell, Azimuth resolution = 0.2966°	51
3.16 CCDF curves, 15m, VV polarization, 2 nd range cell, Azimuth resolution = 0.2966°	52
3.17 PDF curves, 15m, VV polarization, 2 nd range cell, Azimuth resolution = 0.2966°	52
3.18 CCDF curves, 15m, VH polarization, 3 rd range cell, Azimuth resolution = 0.2966°	54
3.19 PDF curves, 15m, VH polarization, 3 rd range cell, Azimuth resolution = 0.2966°	54
3.20 CCDF curves, 9m, HH polarization, 24 th range cell, Azimuth resolution = 0.3241°	55
3.21 PDF curves, 9m, HH polarization, 24 th range cell, Azimuth resolution = 0.3241°	56
3.22 CCDF curves, 9m, VV polarization, 24 th range cell, Azimuth resolution = 0.3241°	56
3.23 PDF curves, 9m, VV polarization, 24 th range cell, Azimuth resolution = 0.3241°	57
3.24 CCDF curves, 9m, HV polarization, 2 nd range cell, Azimuth resolution = 0.3241°	57
3.25 PDF curves, 9m, HV polarization, 2 nd range cell, Azimuth resolution = 0.3241°	58
3.26 CCDF curves, 9m, VH polarization, 28 th range cell, Azimuth resolution = 0.3241°	58
3.27 PDF curves, 9m, VH polarization, 28 th range cell, Azimuth resolution = 0.3241°	59
3.28 CCDF curves, 3m, HH polarization, 3 rd range cell, Azimuth resolution = 44.8956°	59
3.29 CCDF curves, 3m, VV polarization, 17 th range cell, Azimuth resolution = 44.8956°	61
3.30 CCDF curves, 3m, HV polarization, 12 th range cell, Azimuth resolution = 44.8956°	61
3.31 CCDF curves, 3m, VH polarization, 23 rd range cell, Azimuth resolution = 44.8956°	62
3.32 CCDF curves, 3m, HH polarization, 2 nd range cell, Azimuth resolution = 329.87°	62
3.33 CCDF curves, 3m, VV polarization, 2 nd range cell, Azimuth resolution = 329.87°	64
3.34 CCDF curves, 3m, HV polarization, 26 th range cell, Azimuth resolution = 0.3131°	64

3.35	CCDF curves, 3m, VH polarization, 26 th range cell, Azimuth resolution = 0.3131°	65
4.1	CCDF curves, 60m, HH polarization, 17 th range cell, Azimuth resolution = 0.3571°	72
4.2	PDF curves, 60m, HH polarization, 17 th range cell, Azimuth resolution = 0.3571°	72
4.3	CCDF curves, 60m, VH polarization, 17 th range cell, Azimuth resolution = 0.3571°	73
4.4	PDF curves, 60m, VH polarization, 17 th range cell, Azimuth resolution = 0.3571°	73
4.5	CCDF curves, 30m, VV polarization, 20 th range cell, Azimuth resolution = 16.1499°	74
4.6	PDF curves, 30m, VV polarization, 20 th range cell, Azimuth resolution = 16.1499°	74
4.7	CCDF curves, 30m, HV polarization, 17 th range cell, Azimuth resolution = 16.1499°	75
4.8	PDF curves, 30m, HV polarization, 17 th range cell, Azimuth resolution = 16.1499°	75
4.9	CCDF curves, 15m, HH polarization, 11 th range cell, Azimuth resolution = 0.2966°	77
4.10	PDF curves, 15m, HH polarization, 11 th range cell, Azimuth resolution = 0.2966°	77
4.11	CCDF curves, 15m, VV polarization, 22 nd range cell, Azimuth resolution = 0.2966°	78
4.12	PDF curves, 15m, VV polarization, 22 nd range cell, Azimuth resolution = 0.2966°	78
4.13	CCDF curves, 9m, VV polarization, 15 th range cell, Azimuth resolution = 0.3241°	79
4.14	PDF curves, 9m, VV polarization, 15 th range cell, Azimuth resolution = 0.3241°	79
4.15	CCDF curves, 9m, HV polarization, 3 rd range cell, Azimuth resolution = 0.3241°	80
4.16	PDF curves, 9m, HV polarization, 3 rd range cell, Azimuth resolution = 0.3241°	80
4.17	CCDF curves, 3m, HH polarization, 6 th range cell, Azimuth resolution = 44.8956°	82
4.18	PDF curves, 3m, HH polarization, 6 th range cell, Azimuth resolution = 44.8956°	82
4.19	CCDF curves, 3m, VV polarization, 17 th range cell, Azimuth resolution = 44.8956°	83

4.20	PDF curves, 3m, VV polarization, 17 th range cell, Azimuth resolution = 44.8956°	83
5.1	The concept of threshold detection.	87
5.2	Block diagram of the two proposed detectors.	89
5.3	Variation of P_{FA} of the Max-Min detector versus the threshold factor τ using the Weibull distribution.	91
5.4	Variation of P_{FA} of the Max-Min detector versus the threshold factor τ using the K distribution.	91
5.5	Variation of P_{FA} of the Max-Min detector versus the threshold factor τ using the CIG distribution.	92
5.6	Variation of P_{FA} of the Var-Max-Min detector versus the threshold factor τ using the Weibull distribution.	92
5.7	Variation of P_{FA} of the Var-Max-Min detector versus the threshold factor τ using the K distribution.	93
5.8	Variation of P_{FA} of the Var-Max-Min detector versus the threshold factor τ using the CIG distribution.	93
5.9	Variation of P_{FA} of the Max-Min detector versus the threshold factor τ using the Weibull distribution plus two interfering targets.	94
5.10	Variation of P_{FA} of the Max-Min detector versus the threshold factor τ using the K distribution plus two interfering targets.	95
5.11	Variation of P_{FA} of the Max-Min detector versus the threshold factor τ using the CIG distribution plus two interfering targets.	95
5.12	Variation of P_{FA} of the Var-Max-Min detector versus the threshold factor τ using the Weibull distribution plus two interfering targets.	96
5.13	Variation of P_{FA} of the the Var-Max-Min detector versus the threshold factor τ using the K distribution plus two interfering targets.	96
5.14	Variation of P_{FA} of the Var-Max-Min detector versus the threshold factor τ using the CIG distribution plus two interfering.	97
5.15	P_D of the Max-Min detector versus the SCR using the Weibull distribution.	98
5.16	P_D of the Max-Min detector versus the SCR using the K distribution.	98
5.17	P_D of the Max-Min detector versus the SCR using the CIG distribution.	99
5.18	P_D of the Var-Max-Min detector versus the SCR using the Weibull distribution.	99
5.19	P_D of the Var-Max-Min detector versus the SCR using the K distribution.	100
5.20	P_D of the Var-Max-Min detector versus the SCR using the CIG distribution.	100
5.21	Comparison of P_D between the two detectors using the Weibull distribution.	101
5.22	Comparison of P_D between the two detectors using the K distribution.	101
5.23	Comparison of P_D between the two detectors using the CIG distribution.	102
5.24	Variation of P_{FA} of the Max-Min detector versus the threshold factor τ using the actual sea data IPIX.	103

5.25	Variation of P_{FA} of the Var-Max-Min detector versus the threshold factor τ using the actual sea data IPIX.	103
5.26	P_D of the Max-Min detector versus the SCR using the actual sea data IPIX.	104
5.27	P_D of the Var-Max-Min detector versus the SCR using the actual sea data IPIX.	104

List of Tables

2.1	Radar frequency bands and usages.	13
2.2	Douglas sea scale.	21
3.1	The GC model and its derived distributions.	28
3.2	Characteristics of the analyzed files.	44
3.3	Characteristics of the analyzed files.	44
3.4	The estimated parameters for each model for range resolutions 60 and 30m, using PCFE method.	50
3.5	The estimated parameters for each model for range resolution 15m, using PCFE method.	53
3.6	The estimated parameters for each model for range resolution 9m, using PCFE method.	60
3.7	The estimated parameters for each model for range resolution 3m, using PCFE method.	63
3.8	The estimated parameters for each model for range resolution 3m, using PCFE method.	65
4.1	The estimated parameters for each model for range resolutions 60 and 30m, using PCFE method, and the metric tests.	76
4.2	The estimated parameters for each model for range resolutions 15 and 9m, using PCFE method.	81
4.3	The estimated parameters for each mixture model for range resolutions 3m, using PCFE method.	84

Chapter 1

General Introduction

Contents

1.1	Introduction	2
1.2	Motivations and Contributions	3
1.3	Thesis Organization	4

Abstract

This chapter is introductory and informative, it includes a historical overview of the radar system and its importance in maritime and coastal surveillance. This chapter also includes the main motivations and problems addressed in this thesis. Finally, it provides a reading plan for this manuscript.

1.1 Introduction

We could start this thesis, like many studies and scientific research that preceded us and were interested in research topics similar to ours. A RADAR (**RA**dio **D**etection **A**nd **R**anging) operates by radiating electromagnetic energy and detecting the echo returned from reflecting objects. The earliest roots of radar can be associated with the theoretical work of the Scottish physicist James Maxwell who developed equations describing the behavior of electromagnetic wave propagation in 1864. The experimental work of German physicist Heinrich Hertz confirmed Maxwell's theory in 1886 and demonstrated that radio waves could be reflected by physical objects called targets. This fundamental fact forms the basis by which radar can perform the process of detection by sensing the presence of a reflected wave. In 1903, the German engineer Christian Hulsmeyer used this effect to demonstrate the detection of ships at sea and to avoid collisions. Also, in 1922 Marconi applied the same idea in Britain to avoid ship collisions. The U.S. Navy, through the Naval Research Laboratory (NRL), began investigating the use of radio waves for ship detection in 1922 after noting signal interruptions in ship-to-ship and ship-to-shore communications. However, there was not much official interest in this topic and many years passed before systematic experiments in radio detection began. Early work used Continuous Wave (CW) transmissions and was based on interference between a transmitted wave and the Doppler-shifted signal received from a moving target. The first detection of an aircraft by radar occurred accidentally in 1930 with an NRL CW-bistatic system doing direction finding experiments and detecting an aircraft two miles away on the ground, by 1932 NRL radar demonstrated the detection of flying aircraft to distances of 50 miles. This radar can detect the presence of aircraft and can also indicate the direction but cannot give a range. The practical development of pulse radar began in 1930 in the U.S and Britain, but also in several other countries. Both the theory and the technology of radar were developed with great urgency during the second World War [1]. Since 1945 the pace has been slow but steady, radar has found wide-ranging civilian applications, including air traffic control, meteorology, road monitoring, and measuring swarms of insects. The basic principles of radar do not change, but there have been continuous improvements in hardware and system design. There has also been a major increase in the use of digital techniques and intelligent systems for radar signal processing [1]. Today, maritime and coastal surveillance has become a strategic issue for almost all countries of the world in order to curb all types of trafficking, such as smuggling, illegal immigration, and drug trafficking, as well as combating piracy and organized terrorism, or carrying out rescue missions and monitoring the safety and security of property and people. All these tasks require the authorities to detect the presence of small vessels over long distances and certainly require the use of more appropriate monitoring systems and more efficient to detect, locate and classify potential targets. This has increased the demand for radar echo modeling, the development of automatic detectors and sensors based on advanced signal/image processing methods and/or artificial intelligence techniques.

1.2 Motivations and Contributions

The successful optimization of the detection performance of maritime surveillance radars requires detailed knowledge and understanding of both forward and backscattering from the sea surface. When the statistical model does not describe the evolution of the reflected echos "Clutter", the performances obtained are far from those expected. This results in an increase in the false alarm rate and/or a degradation in detection performance. The problem is to find a statistical model which accurately describes the behavior of the clutter and offers better performance in terms of detection. For this reason, many studies have been conducted and are still ongoing to model the sea clutter as accurately as possible. Initially, the radar operators chose the Gaussian model to describe the statistics of the sea clutter, but it quickly became clear that this model did not correctly describe the clutter when operating the radar at a small grazing angle and/or with high-resolution. Indeed, the high amplitude returns generally extend the tail of the sea clutter distribution and thus lead to a deviation from Gaussian statistics. From 1960, several non-Gaussian distributions were proposed to treat this problem and to accurately describe the statistical differences of the reflected signals from the sea surface (Weibull, Log-Normal, Pareto, K, etc...). One of the most common and simplest models comes is the Spherically Invariant Random Vectors model (SIRV), this model has been widely studied in the radar literature, as it contains an excellent synthesis of its properties created for the various models of probability. The appearance of non-Gaussian models led to new theoretical problems that complicate the detection task and must be resolved. Among them, the choice of the best model to describe the intensive sea clutter, especially in the tail region. Also, the estimation of the parameters of non-Gaussian models is one of the widely studied problems, especially when one wants to develop detection strategies based on these models. On the basis of the motivations in terms of sea clutter modeling mentioned above, the proposed contributions of this thesis are mainly based on the following points:

1.2.1 Clutter Modeling

The first contribution in this work concerns the modeling of sea radar clutter using two approximate models of Weibull plus additive thermal noise which are considered as compound models with a speckle and a texture following a Weibull distribution. First, the overall Probability Density Function (PDF) and the Complementary Cumulative Distribution Function (CCDF) are derived in the integral form as well as the expression of the moments. The parameters estimation for each model is conducted using the Parametric Curve Fitting Estimation (PCFE) method of the CCDF function based on the Nelder-Mead (N-M) algorithm and the moments matching method. The proposed Weibull models are evaluated using the synthetic sea data and actual Intelligent PIXel processing X-band (IPIX) sea data. The modeling experiments are worked out and showed that the proposed Weibull models can accurately match the sea clutter, especially in the tail region, outperforming three of the Compound Gaussian (CG) models. The second contribution is considered as a continuation of the first

work, in which we studied the robustness of the mixture of the proposed Weibull approximations to model the sea clutter. In all cases, the proposed mixture model provides an accurate fit to real IPIX data, outperforming the mixture of the CG models.

1.2.2 CFAR Detection in Maritime Environment

In the third contribution two Constant False Alarm Rate (CFAR) decision rules are suggested for Weibull and two CG clutter models. The proposed decision rules are then modified to deal with the presence of thermal noise and interfering targets. The obtained results exhibit a high probability of detection as well as an excellent false alarm rate regulation especially for spiky clutter.

1.3 Thesis Organization

Given the importance of the presentation of this thesis, we have structured this manuscript around six chapters:

Chapter 2 presents some of the radar concepts, such as their operations, classifications, and applications. This chapter also provides an overview of radar clutter modeling.

Chapter 3 is devoted to the modeling of high-resolution radar sea clutter using two approximate Weibull distributions plus thermal noise. This chapter also presents all the mathematical derivations for each function, as well as, simulations and experimental results using synthetic and real IPIX sea data.

Chapter 4 is an extension of Chapter 3, it presents the modeling of sea clutter using a mixture of the proposed Weibull approximations. This chapter presents the mathematical function of the mixture method for each model, simulations and experimental results using real IPIX sea data.

Chapter 5 presents two novel radar detectors for spiky sea clutter with the presence of thermal noise and interfering targets. The suggested detectors were found using the trial and error method. This chapter also presents simulations and experimental results using synthetic and real IPIX sea data.

Chapter 6 recalls the main work of this thesis, contributions and presents the main conclusions. Also, this chapter lists the possible views and suggestions that could serve as an extension of the work proposed in this thesis.

Chapter 2

Radar Concept

Contents

2.1	Radar Basics	6
2.2	Detection Process	7
2.3	Information Extracted From the Radar Echo	7
2.4	Radar Cross Section	9
2.5	Radar Equation Form	10
2.6	Types of Radar Systems	12
2.7	Radar Clutter	18
2.8	Sea Clutter	19
2.9	Sea Clutter Modeling	22

Abstract

This chapter is not intended to provide an in-depth description of the radar system, but to provide the necessary information that helps to understand the proposed work in the following chapters. For more details, the interested reader is invited to review the general literature on radar systems such as [2, 3].

2.1 Radar Basics

Radar is an electrical system that transmits radio frequency electromagnetic waves to an area of interest and receives and detects these waves when reflected from objects in that area. Figure 2.1 illustrates the main components and steps involved in mono static radar, including the process of sending radar signals, the propagation of these signals through the atmosphere, reflection of the signals from the targets, and receiving the reflected signals. Although details of the radar system are different, the main subsystems must include a transmitter, an antenna, a receiver, and a signal processor. The system may be significantly simpler or more complex than that shown in Figure 2.1. The subsystem that generates the electromagnetic waves is the transmitter, the antenna is the subsystem that takes these waves from the transmitter and introduces them into the atmosphere. The transmitter is connected to the antenna via a Transmitter Receiver device (T/R) usually a switch, the function of this subsystem is to provide a connection point so that the transmitter and receiver can be connected simultaneously to the antenna and at the same time provide isolation between transmission and reception. The transmitted waves propagate through the atmosphere towards the target so that it produces currents on the surface, these currents are then reflected. The receiving antenna receives a portion of the reflected waves from the target. The reception circuits amplify and convert the radio frequency signal to an Intermediate Frequency (IF), then the signal is fed into the detector to remove the carrier wave from the modulated signal, and then apply the signal to an Analog to Digital converter (A/D), and to the signal processor to extract the required information, such as the presence, absence, speed and range of the target [3].

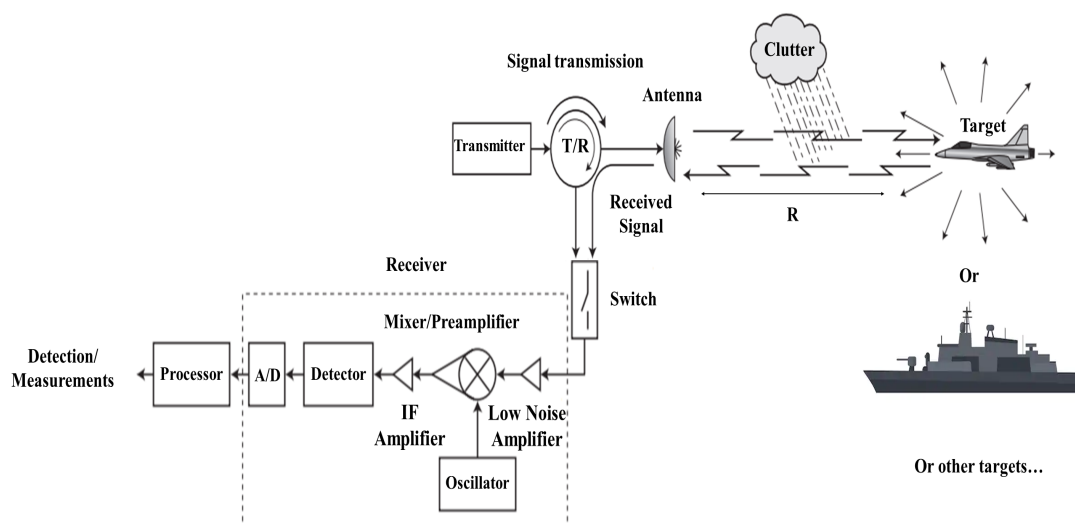


Figure 2.1 – Principle of a radar system.

2.2 Detection Process

The main task of the radar system is to automatically detect the presence of a target and distinguish the true target signal from other unwanted signals. In search mode, the radar system is programmed to change the position of the antenna beam in a specific sequence to scan every possible position in space in search of a target. The detection is a process by which the echo signal of each potential target location is compared to an estimated threshold level from its surroundings to determine whether the signal is sufficiently high to be considered as a target of interest. The echo signal exists alongside interfering signals called "clutter" which comes in many forms, such as electromagnetic waves reflected from uninteresting objects (land, atmosphere, sea, clouds, rain, birds, insects...). Clutter can also come in the form of unintentional external electromagnetic waves from other artificial sources, or waves emitted by special systems to mask the targets that the radar can detect, and internal and external thermal noise. Considering the fact that the clutter is statistically non-stationary and has unknown powers due to the random fluctuation of electrical energy, crossing the detection threshold can be subject to errors and false alarms, which greatly affects the detection performance, especially in conventional radars that use fixed detection thresholds. We define the Probability of False Alarm (PFA) the probability of crossing the threshold by clutter or thermal noise alone. The Probability of Detection (PD) is defined as the probability of crossing the threshold by the signal from the potential target alone or with clutter. To reduce PFA caused by unwanted strong signals and improve PD performance, modern radars use adaptive threshold strategies to maintain a CFAR, this process is performed just before the detection decision is made. In adverse weather conditions, clutter becomes the dominant source and its amplitude may be greater than the target signal, in this case, spectral signal processing such as Moving Target Indication (MTI) is often used to reduce the noise level below that of the target signal. In cases where the dominant interference is jamming and its level exceeds that of the target, the angle of arrival processing can often be used. The systems that undergo a significant clutter and jamming interference may use a combination of both MTI and angle of arrival processing, called Space Time Adaptive Processing (STAP) [2]. In addition, optimal detection strategies, such as Bayes or Neyman Pearson (NP), must be developed based on an accurate modeling of echo signals, capable of operating at all times and in all conditions regardless of the environment in which the radar is operating.

2.3 Information Extracted From the Radar Echo

Although the name of the radar is derived from the radio detection and ranging, the radar is able to provide more information about the target than that indicated by its name. The detection of a target means discovering its presence, detection can be considered independently of the information extraction process, but it is rare that we are interested in knowing only that a target is present without knowing anything about its location in space and its nature.

Extracting useful information on the target is an important part of the operation of the radar system. Information extraction generally requires appropriate filters for optimal processing. The more information we already know about a target, the more effective the detection. For example, if the target location is known, the antenna can be pointed in the correct direction, and there is no need to waste electrical power or time searching in empty space. Or, if the relative velocity is known, the receiver can set the correct reception frequency, eliminating the need to find the frequency range in which a Doppler shift can occur. The rate of change in the target location can also be measured from the change in distance and angle over time, by which the path can be established, in many radar applications the detection does not occur until its path is determined. Radar of sufficient accuracy in one or more coordinates can determine the size and shape of the target. Polarization mode allows a measurement of the symmetry of a target. In practice, the radar can also measure the surface roughness of a target and determine something from its properties [3].

2.3.1 Range

The ability to define a range by measuring the time for the radar signal to propagate to the target and return is perhaps the most important distinguishing feature of conventional radar. There is no other sensor that can measure the distance as accurately as the radar especially under adverse weather conditions. Radar has shown its ability to measure distances between planets with an accuracy limited to only the accuracy with which the velocity of propagation is known. In the case of modest distances, the measurements of range can be made with a precision of a few centimeters. The usual radar waveform for determining range is the short pulse, The shorter the pulse, the more accurate the measurement, a shorter pulse has a wide spectral width (bandwidth). CW with frequency or phase modulation can also provide accurate distance measurement. It is also possible to measure the range of a single target by comparing the phase difference between two or more CW frequencies. Distance measurement with CW waveform has been widely used, as is the case with radar altimeters and aircraft scanners. The range of target R is calculated by measuring the delay Δt required for a pulse to travel in the bidirectional path between the radar and the target, since electromagnetic waves travel at the speed of light $c = 3 \times 10^8 m/sec$, then :

$$R = \frac{c\Delta t}{2} \quad (2.1)$$

where, R is in meters and Δt is in seconds.

2.3.2 Radial Velocity

From successive distance measurements, it is possible to obtain the rate of change of distance or radial velocity. The Doppler frequency shift of the echo signal of a moving target also provides a measure of radial velocity. However, the measurement of Doppler frequency in many pulse radars is highly ambiguous, reducing its utility as a direct measurement of radial

velocity. When it can be used, it is often better to use successive measurements because it provides more accurate measurements in a shorter time. Any speed measurement, whether by the rate of range change or by the Doppler frequency shift, takes time, the longer the observation takes, the more precise the speed measurement can be. A longer observation time can also increase the Signal to Noise Ratio (SNR), another factor that results in increased accuracy. Although Doppler frequency shift is used in some applications to measure radial speeds, such as police speedometer and satellite surveillance, it is widely used as the basis for sorting out moving targets from unwanted echoes, as in MTI and AMTI (Airborne MTI) and CW radars.

2.3.3 Angular Direction

The direction of the target is determined by detecting the angle at which the returning wavefront arrives at the radar. This is achieved usually by using a directional antenna, with a narrow beam. The angle of arrival is defined by comparing the reflected echo signal with the transmitted signal. The direction in which the antenna points when the received signal is a maximum indicates the direction of the target. This, as well as other methods for measuring angle, assumes that the atmosphere does not perturb the straight-line propagation of the electromagnetic waves. The direction of the incident waveform can also be determined by measuring the phase difference between two separate receiving antennas. The angle of arrival accuracy depends on the aperture range of the antenna, the wider the antenna, the narrower the beamwidth, and the better the accuracy. The determination of the angle basically involves only the one-way path, however, angle measurement is an integral part of most surveillance and tracking radars. Other important information can be extracted from the echo signal, such as size, shape, and tangential velocity.

2.4 Radar Cross Section

The radar range equation expresses the range at which a target may be detected with a given probability by a radar having a given set of parameters. This equation includes the Radar Cross Section (RCS) of an equivalent isotropic radiator, an important parameter that defines the scattering efficiency of a target, another term for RCS is echo area. The purpose of the RCS is to characterize the target, knowledge of the RCS is essential in the calculations of radar range and the SNR. The target's RCS may be viewed as a comparison of the strength of the reflected signal from a target to the reflected signal from a perfectly smooth sphere of the cross sectional area of $1m^2$. In fact, the RCS is defined as an equivalent cross section of the target producing the same amount of energy returned to the radar as would be produced by an isotropic radiator. The RCS and the physical area of the target are not directly related through some simple equations [4].

The RCS of a target is a measure of its ability to reflect electromagnetic energy in the direction of the radar receiver, and its value is expressed as an area. This reflected energy is dependent on a multitude of parameters such as:

- The radar transmitters frequency
- The direction of the illuminating radar
- Target geometry
- The material of which the target is made
- The absolute size of the target
- The incident angle (angle at which the radar beam hits a particular portion of the target, which depends upon the shape of the target and its orientation to the radar source)
- The polarization of the transmitted and the received radiation with respect to the orientation of the target

The RCS, denoted by the symbol σ , is the area intercepting that amount of power which, when scattered equally in all directions, produces an echo signal at the radar equal to that from the target. In other terms:

$$\sigma = \frac{\text{power reflected back to receiver per unit solid angle}}{(\text{incident power density intercepted by the target})/4\pi} = \lim_{R \rightarrow +\infty} 4\pi R^2 \left| \frac{E_r}{E_i} \right|^2 \quad (2.2)$$

where R is the distance between the radar and target, E_r is the reflected electric field strength at radar, and E_i is the incident electric field strength at target. For most common types of radar targets such as aircraft, ships, and terrain, the RCS does not necessarily have a simple relationship to the physical area, except that the larger the target, the greater the probability that the cross section is larger. More information and details about RSC are available in [5].

2.5 Radar Equation Form

The radar equation relates the range of the radar to the characteristics of the transmitter, receiver, antenna, target, propagation path, and environment [2, 3]. It is useful not just as a means for determining the maximum distance from the radar to the target, but it can serve both as a tool for understanding radar operation and as a basis for radar design. In this section, the simple form of the radar equation is derived. If the power of the radar transmitter is denoted by P_t and if an isotropic antenna is used, which radiates the electromagnetic energy uniformly in all directions.

The power density \hat{P}' at a distance R from the radar is equal to the transmitter power divided by the surface area $4\pi R^2$ of an imaginary sphere of radius R , this expressed as:

$$\text{Power density from isotropic antenna} = \frac{P_t}{4\pi R^2} \quad (2.3)$$

Radars use directional antennas to channel the radiated power P_t into some particular direction. The gain G of an antenna is a measure of the increased power radiate in the direction of the target as compared with the power that would have been radiated from an isotropic antenna. It can be defined as the ratio of the maximum radiation intensity from the antenna to the radiation intensity from a lossless isotropic antenna with the same power input. The radiation intensity is the power radiated per unit solid angle in a given direction. The power density at the target from an antenna with a transmitting gain G is given by:

$$\text{Power density from directive antenna} = \frac{P_t G}{4\pi R^2} \quad (2.4)$$

The target intercepts a portion of the incident power and re-radiates it in various directions. The measure of the amount of incident power intercepted by the target and re-radiated back in the direction of the radar is denoted as the radar cross section RCS σ , as we mentioned above, and is defined by the relation:

$$\text{Power density of echo signal at radar} = \frac{P_t G}{4\pi R^2} \frac{\sigma}{4\pi R^2} \quad (2.5)$$

If all of the incident radar energy on the target were reflected equally in all directions, then the RCS would be equal to the cross section of the target as seen by the transmitter. In practice, some energy is absorbed and the reflected energy is not distributed equally in all directions. Therefore, the RCS is quite difficult to estimate and is normally determined by measurement. The radar antenna captures a portion of the echo power, if the effective area of the receiving antenna is denoted A_e , the power P_r received by the radar is given by:

$$P_r = \frac{P_t G}{4\pi R^2} \frac{\sigma}{4\pi R^2} A_e = \frac{P_t G A_e \sigma}{(4\pi)^2 R^4} \quad (2.6)$$

The maximum radar range R_{max} is the distance beyond which the target cannot be detected. It occurs when the received echo signal power P_r just equals the minimum detectable signal S_{min} . Therefore:

$$R_{max} = \left[\frac{P_t G A_e \sigma}{(4\pi)^2 S_{min}} \right]^{1/4} \quad (2.7)$$

The important antenna parameters are the transmitting gain and the receiving effective area. Antenna theory gives the relationship between the transmitting gain and the receiving effective area of an antenna as:

$$G = \frac{4\pi A_e}{\lambda^2} \quad (2.8)$$

Since radars generally use the same antenna for both transmission and reception, Eq (2.8) can be substituted into Eq (2.7), first for A_e then for G , to give two other forms of the radar equation:

$$R_{max} = \left[\frac{P_t G^2 \lambda^2 \sigma}{(4\pi)^3 S_{min}} \right]^{1/4} \quad (2.9)$$

$$R_{max} = \left[\frac{P_t A_e^2 \sigma}{4\pi \lambda^2 S_{min}} \right]^{1/4} \quad (2.10)$$

This is the basic form of some of the radar equations. More information is available in [2].

2.6 Types of Radar Systems

Since the fundamental radar functions are search, detection, tracking, and imaging, many remote sensing applications can be satisfied by the use of radar technology. There are many different types of radar systems. The method for classifying a particular radar depends on the specific characteristics of the radar such as the radar mission, the type of antenna, the frequency range, the specific measurements to be performed, the waveform it uses, and the physical environment in which it should operate. The radar applications represented here are some of the most common, but there are many more.

2.6.1 Classification by Frequency Band

Although radars usually use a radio frequency between 220 and 35 000 MHz, they can also function in any spectral region. A few types of radar are found in the lower band, except where particular propagation and target characteristics dictate their use. Early in the development of radar, a letter code was employed to designate the radar frequency band. At the upper frequency end of the spectrum, L-band, S-band, C-band, and X-band radars are used where the size of the antenna constitutes a physical limitation. The other higher frequency bands (K_u , K , and K_a) suffer severe weather and atmospheric attenuation. Further information on common use and applications of the radar frequency bands, as defined by IEEE, are summarized in Table 2.1.

Band	Frequency (GHz)	Usage
HF	0.003–0.03	OTH surveillance
VHF	0.03–0.3	Very long-range surveillance
UHF	0.3–1	Very long-range surveillance
L	1–2	Long-range military and air traffic control search
S	2–4	Medium range surveillance, and meteorological
C	4–8	Search and fire control radars, weather detection
X	8–12.5	Short-range tracking, missile guidance, marine radar
K_u (under K band)	12.5–18	High-resolution mapping, satellite altimetry
K	18–26.5	Police speed-measuring, airport surface detection
K_a (above K band)	26–40	Very high-resolution mapping, airport surveillance
MM-Wave	40–300	Laser range finders and optical targeting systems. Experiments

Table 2.1 – Radar frequency bands and usages.

2.6.2 Classification by Waveform and Pulse Rate

One of the most important technical characteristics of a radar system is the type of transmission waveform it uses. Radars are classified according to two types of waveform that they transmit. The first type comprises the radar pulse "pulsed radar" in which the radar emits a pulse and waits for the return, in general, radar of this type using a pulse train as shown in Figure 2.2.

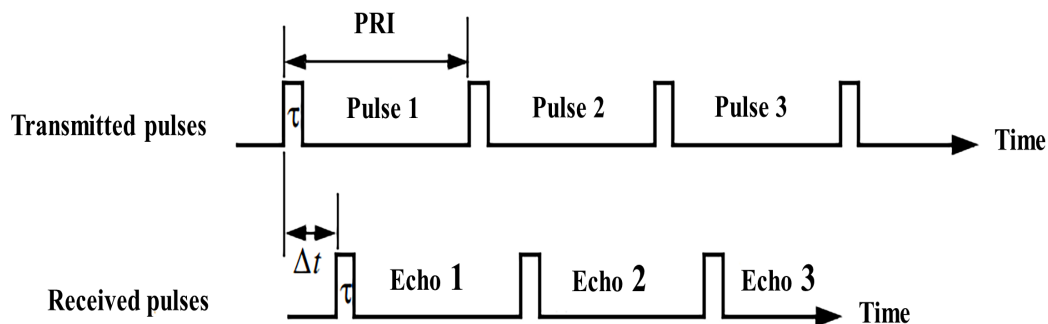


Figure 2.2 – Train of transmitted and received pulses.

where, PRI is the Pulse Repetition Interval, and τ is the duration or width of the pulse. The PRI is often referred to as the Inter Pulse Period (IPP). There are two types of pulses: short pulses (from 1 to 60 μs) used for short range monitoring, and long pulses (100 to 500 μs) used for long range surveillance, moreover, they can be classified, depending on the Pulse Repetition Frequency (PRF) into low, medium, and high PRF radars. Low PRF radars are mainly used to measure the distance of the target whose speed is not taken into account and high PRF radars are used to measure the target speed. The second type of classification includes CW radars, where the radar continuously emits electromagnetic energy from an antenna and receives using a second antenna separate from the first, this type is used to track and guide missiles. Unmodulated CW radars can accurately measure target radial velocity

and angular position, utilizing some form of time variant modulation, the range information can be extracted [4] .

2.6.3 Primary and Secondary Surveillance Radar

A Primary Surveillance Radar (PSR) is a conventional radar sensor that illuminates a large portion of space with an electromagnetic wave and receives back the reflected waves from targets within that space. The advantages of the primary radar are no onboard equipment in the target to perform the detection process, and can be used to monitor the movement of vehicles on the ground. The disadvantages are that the relationship between the echo strength and the range presents a major problem for long range detection. It is also very difficult to determine the altitude of an aircraft accurately using primary radars. Secondary Surveillance Radar (SSR) is a lot more complex than the PSR, it does not rely on reflected pulse technology and requires cooperation from the target, unlike the PSR. The target needs to carry a special equipment as well, this equipment is called a transponder, it is called a transponder because it responds to the interrogation from the secondary radar. The SSR generates a beam of pulse in the horizontal direction for the interrogation, while the target or the aircraft transmits back omnidirectionally. There are three main modes of interrogation, mode A, mode C and mode S. The physical differences between the two types, the PSR is that huge rotating parabolic plate, and the SSR is much smaller and can be seen hoisted at times on top the primary radar, it looks like a horizontal metal sheet [4].

2.6.4 Monostatic, Bistatic, Multistatic and MIMO Radar

The physical configuration of the transmit and receive antennas also classify radars into monostatic, bistatic, and multistatic radars. Those radars where the same antenna is used for both transmission and reception or where the separate transmit and receive antennas are in essentially the same location are monostatic. On the other hand, in bistatic and multistatic radars the transmit and receive antennas are geographically placed in two or more different locations where the distance of separation between them is/are significant. This type of radar is useful in CW or Frequency Modulated Continuous Wave (FMCW) to achieve less spillover interference. The functions of the elements in bistatic/multistatic radars are the same as monostatic radars, with the major difference being in the absence of the duplexer. A synchronization link between the transmitter and the receiver is necessary to maximize the receiver knowledge of the transmitted signal, frequency and phase reference synchronization can also be maintained. A Multiple Input Multiple Output (MIMO) radar system, a subset of multistatic radar, is a system of multiple antennas in which each transmit antenna radiates an arbitrary waveform independently of the other transmitting antennas and each receiving antenna can receive these signals. Due to the different waveforms, the echo signals can be reassigned to a single transmitter [4].

2.6.5 Tracking and Acquisition Radar

Tracking radar system measures the coordinates of a target and provides data which may be used to determine the target path and to predict the future position. All or only part of the available radar data, range, elevation, azimuth angle, and Doppler frequency shift may be used in predicting the future position. Almost any radar can be considered a tracking radar provided its output information is processed properly. But, in general, it is the method by which angle tracking is accomplished that distinguishes the tracking radar from any other radar. It is customary to distinguish between a continuous tracking radar and a track while scan radar. The continuous tracking radar provides continuous tracking data on a particular target, while the track while scan radar provides sampled data on one or more targets to apply in sophisticated smoothing and prediction filters, namely Kalman filters. The tracking radar utilizes a very narrow beam to find its target before it can track. Some radars operate in search mode to find the target before switching to a track mode. When a single radar is used for both search and tracking functions, it usually results in certain operational limitations. Obviously, when it uses the radar in tracking mode, it has no knowledge of other potential targets. Also, if the antenna pattern is a narrow pencil beam and if the search volume is large, a relatively long time might be required to find a target. Thus many radars of the tracking system use a separate search radar to provide the information needed to place the tracker on the target. The search radar, when used for this purpose, is called the acquisition radar. The acquisition radar identifies targets for the tracking radar by providing the coordinates of where to find the target. Target tracking finds important applications in military radars as well as in most civilian radars, including in fire control, missile guidance, and airport traffic control for incoming and departing airplanes [4].

2.6.6 Instrumentation Radar

It is a single pulse system that operates in the C range and has been designed to test rockets, missiles, ammunition as well as to test aircraft performance. This radar can track incoherent or transponder modes, the transponder is installed in the missile and receives the radar pulse and re-transmits a single pulse or a double pulse on a different frequency, depending on the transponder settings. A transponder is used when it is necessary to ensure that the radar is tracking the correct object, and for more precise or longer range tracking. The input and output specifications of the transponder depend on the specific test requirements.

2.6.7 Synthetic Aperture Radar

Synthetic Aperture Radar (SAR) is an earth observation technology that takes pictures of both the land and the sea, without the need for sunlight or the need for a clear sky. Typically SAR is implemented by mounting on a moving platform such as an aircraft or spacecraft. A single-beam antenna through which the target scene is repeatedly illuminated with pulses of microwaves at wavelengths anywhere from a meter down to millimeters. The various echo waveform received successively at the different antenna positions are coherently detected and stored and then post-processed together to resolve elements in an image of the target region. SAR resolution is approximately equal to one-half the length of the actual antenna and does not depend on platform altitude (distance). High range resolution is achieved through pulse compression techniques. Signal processing uses the magnitude and phase of the received signals over successive pulses from elements of a synthetic aperture to create an image. As the line of sight direction changes along the radar platform trajectory, a synthetic aperture is produced by signal processing that has the effect of lengthening the antenna. In general the larger the antenna, the more unique information you can obtain about a particular viewed object. With more information, you can create a better image of that object (improved resolution). Placing very large radar antennas in space is prohibitively expensive, so researchers found another way to obtain fine resolution data. They use spacecraft motion and advanced signal processing techniques to simulate a larger antenna. The SAR's ability to pass relatively unaffected through clouds, illuminating the Earth's surface with its own signals, and accurately measuring distances makes it particularly useful for the following applications: sea ice monitoring, cartography, forest cover mapping, urban planning, coastal surveillance, and monitoring disasters such as forest fires, floods, volcanic eruptions, and oil spills. The radio waves used in SAR typically range from approximately 3 cm up to a few meters in wavelength, which is much longer than the wavelength of visible light, used in making optical images. One of the most fundamental characteristics of a SAR system is its operating frequency, with frequencies ranging from 3 MHz to 300 GHz [5].

2.6.8 Weather Radar

Weather radar is also known as Doppler weather radar and Weather Surveillance Radar (WSR), the main distinction between weather radar and other types of radars is the nature of the targets. Weather radars play a crucial role, the information they provide enables meteorologists to issue warnings and early alerts of severe or extreme weather events, which save countless lives and reduce damage. Weather radars can provide information on precipitation intensities and wind speeds, providing a three-dimensional view of storms and allowing detailed location and characterization of associated severe weather conditions. Information from weather radars is used to predict the formation of typhoons, hurricanes, tornadoes, and other severe weather events and to track their course. They also are used in predicting the potential for flash floods, high winds and lightning potential. All meteorological radars op-

erate by transmitting radio signals and measuring the returned signal. Only a tiny fraction of emitted energy is reflected or back-scattered by atmospheric constituents such as raindrops, therefore, weather radar receivers are very sensitive instruments. Any disturbance within the same frequency band reduces or destroys the usability of their measurements. This radar uses Doppler shifts to calculate wind speed and to observe the movement of dangerous weather elements (tornadoes and severe thunderstorms). Also, they use dual-polarization to identify the types of precipitation (rain, snow, hail, etc.). There are three frequency bands commonly used for weather radars [6]:

- S-band: (2700–2900 MHz), deployed mostly in tropical and temperate climate areas, for example, in areas where hurricanes, tornadoes, large hail, and monsoon or heavy rain are common.
- C-band: (mainly 5600-5650 MHz band), used in climates where attenuation (weakening of radar return signal) by intervening in heavy rain or large hail is a very minor issue.
- X-band: (9300-9500 MHz), used in meteorological applications such as short-range urban.

2.6.9 Maritime Navigation Radar

The radar is one of the most important elements of marine electronics on any ship, it is designed to detect and track sea targets at a great distance, it goes without saying that it is of great practical value to mariners. Its main purpose is to help prevent a collision when navigating in darkness, fog, or other situations with limited visibility. Radar is also useful for monitoring the position and movement of ships when crossing narrow lanes or congested waterways, regardless of visibility. The radar also helps determine the position of ships in relation to landmasses or islands, even when you are out of sight with the naked eye. The two fundamental characteristics of a marine radar are the transmitter power and beam angle. The power can vary between 4 and 25 kilowatts, the power is an essential factor in determining the performance of a radar in bad weather. The higher the power of a radar, the better the transmitter can see through dense fog and rain, and the farther the signal can reach. The beam angle is determined by the size of a radar antenna. A long antenna emits a narrow beam which can better distinguish objects close to each other than a shorter antenna. On the other hand, a short antenna produces a wider beam angle which allows the radar to scan a larger area than a long antenna at a time. The specific environment for maritime surveillance radars is sea clutter, the characterization of unwanted echoes reflected from the sea surface, is an important step in the performance analysis of different remote sensing systems, for many applications [7]:

- Detection, recognition and identification of objects present on the sea surface (periscope, low-flying plane or missile) to ensure coastal safety.
- Identification of small boats, buoys, icebergs or oil slicks.
- Surveillance and intervention on vessels operating in illegal fishing.
- The exploitation of signals reflected from the sea surface to obtain oceanographic characteristics of seawater.

2.7 Radar Clutter

Radar clutter is defined as any unwanted radar echo that can disrupt radar output and make it difficult to detect the desired target. The existence of clutter always degrades radar performance because clutter returns compete with target returns in the radar detection process. When clutter echoes are sufficiently intense and extensive, they can impose serious limitations in the performance of radar operations, and in such circumstances, the optimum radar waveform and receiver design can be quite different than when receiver noise alone is the dominant effect. Radar echoes from land, sea, rain, birds, and other such objects are not always undesired. Reflections from storms and clouds, for example, can be a nuisance to radar searching for aircraft, but this is what a radar meteorologist wants to see in order to measure precipitation rates over a larger area. The reflected signals from land can degrade the performance of many radars, but it is the target of interest for a ground mapping radar. Thus, the same object may be the desired target in one application and an unwanted echo in another. Clutter may be divided into sources distributed over a surface, within a volume, or concentrated at discrete points. Ground or sea returns are typical surface clutter. Returns from geographical landmasses are generally stationary, however, the effect of wind on trees, means that the target can introduce a Doppler shift to the radar return. In the air, the most significant problem is weather clutter, which can be produced from rain or snow and can have a significant Doppler content. Windmills and individual tall buildings are typical point clutter and are not extended in nature. Birds and insects produce clutter, which can be very difficult to remove because the characteristics are very much like aircraft. Clutter can be fluctuating or non-fluctuating, ground clutter is generally non-fluctuating in nature because the physical features are normally static. On the other hand, weather clutter is mobile under the influence of wind and is generally considered fluctuating in nature. Clutter can be defined as homogeneous if the density of all the returns is uniform. Most types of surface and volume clutter are analyzed on this basis, however, in practice this simplification does not hold true in all cases. Non-homogeneous clutter is non-uniform clutter where the amplitude of the clutter varies significantly from cell to cell [4]. Figure 2.3 illustrates different types of clutter radar sources.

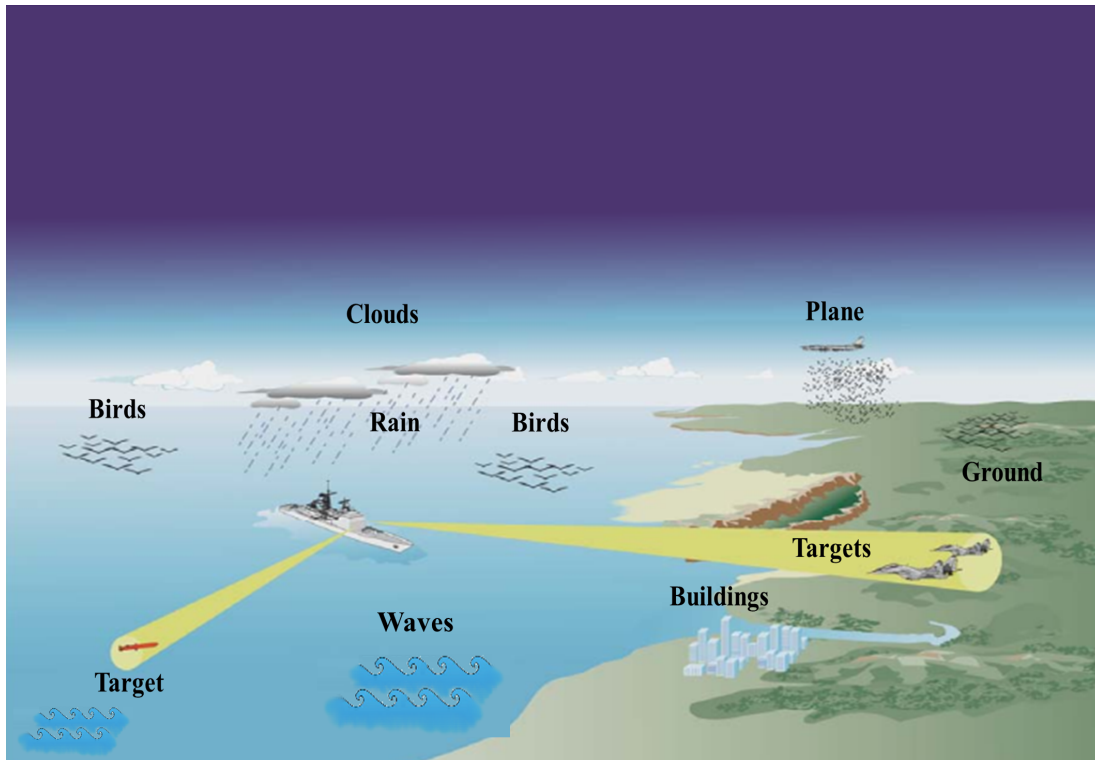


Figure 2.3 – Sea radar scan and various sources of clutter.

Due to the distributed nature of the clutter, the measurement of backscatter echo from such clutter is generally given in terms of RCS density. For surface clutter, we define an RCS per unit area:

$$\sigma = \frac{\sigma_c}{A_c} \quad (2.11)$$

where σ_c is the RCS from the area A_c . The advantage of using this expression to describe distributed surface clutter is that it is usually independent of area A_c . For volume distributed clutter a cross section per unit volume, or reflectivity is defined as:

$$\eta = \frac{\sigma_c}{V_c} \quad (2.12)$$

where σ_c in this case is the radar cross section from the volume V_c .

2.8 Sea Clutter

Sea clutter depends on wave height, wind speed, length of time, distance the wind blows, wave direction, and tides. The sea clutter also depends on radar parameters such as frequency, polarization, grazing angle, and to some extent the size of the area observed. Although there is much that is known about the nature of sea clutter, the quantitative, and sometimes even the qualitative, the effects of many of the factors mentioned above are not known at the required level. There is a range of information regarding radar echoes from the

sea, some of which will be briefly mentioned in this section. A number of features are used to describe the sea clutter including [7]:

- The area reflectivity σ
- The amplitude distribution of the clutter or power
- The spectrum of the clutter returns
- The spatial variation of the clutter return
- The polarization scattering matrix
- The discrete clutter spikes

The amplitude statistics of sea clutter are described using families of PDFs, and their derived functions. The manner in which these amplitude fluctuations vary with time is characterized by the spectrum of the returns.

2.8.1 Sea Surface

Observations of sea clutter are generally associated with particular features of the sea surface and the environment, such as sea waves, sea swell, and wind speed. Some of the basic terms used to describe the sea surface are presented here [7]:

- Wind wave: a wave resulting from the action of the wind on a water surface.
- Gravity wave: a wave whose velocity of propagation is controlled primarily by gravity, water waves of a length greater than 5 cm are considered gravity waves.
- Capillary wave also called ripple or capillary ripple: a wave whose speed of propagation is controlled primarily by the surface tension of the liquid in which the wave is traveling, water waves of a length of less than 2.5 cm are considered capillary waves.
- Fetch also called generating area: an area of ocean, sea, or lake surface over which the wind blows in an essentially constant direction, thus generating waves.
- Duration: the length of time the wind blows in essentially the same direction over the fetch.
- Fully developed sea also called a fully arisen sea: the maximum height at which ocean waves can be generated by a given wind force blowing a sufficient amount, regardless of the duration.
- Sea state: a description of the properties of sea surface waves at a given time and place, it is related to the Beaufort scale which describes the state of the sea.

The description of sea state (wave height) is a common source of confusion in the specification of radar performance. The Beaufort wind scale is often used to estimate wave heights, but this method only gives a reliable estimate of wave height if the duration and the fetch are known. Another measurement estimate for wave height is the Douglas sea scale invented by the English Admiral H.P. Douglas in 1917, while he was head of the British Meteorological Navy Service (BMNS). The Douglas sea scale is expressed in one of 10 degrees (Table 2.2). Other descriptions of sea state are also used, such as the World Meteorological Organization Sea State (WMOST).

Douglas Sea Scale Degrees	Wave height (m)	Wave height (ft)	Description
0	No wave	No wave	Calm (Glassy)
1	0–0.10	0.00–0.33	Calm (Rippled)
2	0.1–0.5	0.33–1.64	Smooth
3	0.5–1.25	1.64–4.10	Slight
4	1.25–2.50	4.10–8.20	Moderate
5	2.5–4.0	8.20–13.10	Rough
6	4.0–6.0	13.10–19.70	Very rough
7	6.0–9.0	19.70–29.50	High
8	9.0–14.0	29.50–45.90	Very high
9	Over 14.00	Over 45.90+	Phenomenal

Table 2.2 – Douglas sea scale.

2.8.2 Sea Clutter Reflectivity

Sea clutter is derived from a complex interaction between incident electromagnetic waves and the sea surface. The essential feature of radar sea clutter, and important for radar performance evaluations, is its apparent reflectivity. Sea clutter reflectivity depends on many factors, including sea state, wind velocity, grazing angle, polarization, radar frequency and many other factors. Empirical models often present reflectivity as a function of the sea state. However, this is not always a reliable indicator as it is dominated by the wave height of long waves and sea swell. Local winds cause surface roughness of small scale, which quickly responds to changes in wind speed and back scattering change. A strong swell without a local wind gives low reflectivity, while a strong local wind gives a strong backscatter from a relatively flat sea. Further deviation from a simple sea state trend may be caused by propagation effects such as ducting, which can affect the illumination grazing angle. There are many theoretical models for back-scatter based on different descriptions of the rough surface and approximations to the scattering mechanism. Specific models for the reflectivity of sea clutter are discussed in chapter 3. For more details on the characteristics of sea chaos, can be found in [7].

2.9 Sea Clutter Modeling

All maritime radars inevitably encounter sea clutter, whether the radar is used for long-range surveillance, detection of aircraft, or very small targets such as periscopes of submarines. Radars on board, whether used for navigation or for air and maritime surveillance, must deal with and eliminate unwanted sea clutter. Modeling and simulation are essential parts of almost all aspects of the engineering design and development of complex systems, modern radar is no exception. The main reason for radar clutter modeling is to provide information for the development of radar systems that respond to the operational needs of their users. Correct and precise modeling of sea clutter provides a solid and reliable basis for the detection process. Initially, the classical statistical description of sea clutter based on a representation of slopes and wave heights in terms of random Gaussian distribution on each of the two channels in-phase and quadrature-phase of the radar receiver. This model can be applied very efficiently in the low-resolution radar systems at low angles of incidence, where the pulse width is greater than $0.5\mu\text{s}$ [7]. On the other hand, in some environments, the clutter becomes impulsive or spiky echoes of high amplitudes, so the use of high-resolution radar is essential, in this case, the statistics of the sea clutter deviate very quickly from the Gaussian model [7]. In addition, the returns have a high amplitude and generally lead to the appearance of the target of interest in the tail of the clutter distribution, where detectors operating in Gaussian environments become ineffective. Therefore, modern radar needs more fitted models with longer tails such as Log-Normal [8] and Weibull [9] distributions, where these models provided a good description of the sea clutter statistics. Non-Gaussian statistical models have been proposed, chosen mainly for their analytical convenience. Sea clutter is determined by two components of amplitude, speckle and texture fluctuations, one related to the intrinsic properties of the sea surface, which is a rapidly fluctuating component associated with capillary waves, the other to its average inclination which is a component of slow fluctuations, associated with gravity waves, respectively [7]. For seventy years, classical distributions have been supplanted by the compound Gaussian model and associated models. This class of models was introduced, in the context of maritime radar clutter, by Jakeman and Pusey [10], these authors relied on analogies between microwave scattering and optical wavelengths. It has been shown that the K distribution shows a detailed analysis of sea clutter in the work of Ward [7]. This approach highlights the usefulness of the compound representation of the clutter process, this made it possible to systematically analyze the effects of thermal noise and the spatio-temporal correlation properties displayed by the clutter and their impact on the maritime surveillance radar [11]. Oliver has developed similar ideas in the context of the SAR system, which contributed significantly to the interpretation of two-dimensional imaging radar [12]. These developments in the application of the K distribution in the microwave field have been supplemented by work at optical wavelengths [13].

Few years later, several non-Gaussian models were suggested to model sea clutter, such as the Pareto [14, 15] distribution and its extended version with thermal noise [16]. Also, the Compound Inverse Gaussian (CIG) and CIG plus noise distribution [17]. All of these distributions were examined for modeling actual sea clutter, where it turns out that when the resolution becomes finer and/or when the HH antenna polarization mode is used, in some cases these models provide a poor fit in the tail region [18]. The Generalized Compound (GC) model has been proposed to model sea clutter at high-resolution and is used to describe the deviation of the speckle component from Rayleigh to Weibull or other models with a long tail. The GC distribution can be used to accurately model sea clutter [19]. Also, Helstrom *et al* proposed an approximate method for calculating the PDF of the amplitude of the sum of Weibull clutter and thermal noise [20]. In the context of sea clutter modeling, a lot of work has been done. Watts proposed the K distribution model with additive thermal noise, which used the actual Cumulative Density Function (CDF) curves to estimate the shape parameter, this model provides a good match with the actual data [21]. Using the Maximum Likelihood Estimator (MLE), Weinberg analyzed the performance of the Pareto distribution to fit high-resolution clutter by the INGARA database, it has been shown that this model is superior in performance on the distributions K and KK [15]. Watts *et al* in [22] extended the KA distribution proposed by Ward and Tough in [23] to include thermal noise, this model provides a precise fit in the tail region of sea clutter outperforming the K model. Ollila *et al* suggested a long-tailed CG model with an inverse Gaussian texture distribution, this model showed a precise clutter fit, outperforming the K and t distributions [24]. For the high-resolution sea clutter modeling, Greco *et al* compared the fit of LN PDF, Weibull, K, and Generalized K (GK) to real sea data. The results show that for all polarization modes with resolutions of 60, 30 and 15 meters, the GK PDF accurately adjusts the sea data. However, for range resolutions of 3 and 9m, in all polarized data the compound model fails to provide a good fit, only for 9m data and VH mode, the GK model shows precise fit in almost all cells. They also showed using the cumulants method that for resolutions of 3 and 9 m, the speckle deviates from the Gaussian distribution [25]. Farina *et al* performed a detailed analysis of experimental sea data. The results showed that the VV data corresponds exactly to the K model, while the HH data correspond well to a LN model and the cross-HV data by the K model plus thermal noise, especially in the tail region [26]. Also, to this end, Carretero *et al* presented a statistical analysis of sea noise data, collected with a high-resolution Ka-band radar on the south coast of Spain. The results showed that the GK model with LN texture (GK-LNT) provides a precise fit to the empirical PDF [27]. Farshchian and Posner analyzed the sea clutter using a database collected on the coast of Kauai, Hawaii. The Pareto distribution and the two mixture distributions WW and KK offer the best fit to the real sea data than the LN, Weibull and K distributions [28]. For the K model plus thermal noise, Mezache *et al* proposed a method for estimating parameters using the PCFE method based on the N-M algorithm developed by Lagariass *et al* [29]. This method gives the best estimate of the spiky clutter parameter [30].

Also, Mezache *et al* used the PCFE method to model and estimate CIG parameters plus thermal noise and showed that this model provides a good fit to real amplitude of sea clutter [31]. Numerous works in this context demonstrate that there is agreement on the validity of the CG model, and different results have been reported for the appropriate amplitude PDF [18], [32, 33, 34, 35].

Chapter 3

Modeling of High-Resolution Radar Sea Clutter Using Two Approximate Weibull Distributions plus Thermal Noise

Contents

3.1	Introduction	26
3.2	Generalized Compound Model without Thermal Noise	27
3.3	Generalized Compound Model with Thermal Noise	35
3.4	First Weibull Model plus Thermal Noise	35
3.5	Second Weibull Model plus Thermal Noise	36
3.6	Simulation Results and Discussions	39
3.7	Conclusions	66

Abstract

This chapter is considered as the main work proposed in this thesis. It proposes statistical modeling of high-resolution sea clutter based on two approximate Weibull distribution plus thermal noise. In the first part, we recall the statistical description of the Generalized Compound distribution (GC) without and with thermal noise, and its derived models. Next, we give the mathematical steps to derive the proposed models. Finally, we evaluate the fitting performance of the proposed models to sea data using synthetic data as well as the IPIX database collected by the McMaster university radar on the east coast of Canada.

3.1 Introduction

Sea clutter modeling is characterized mainly at the tail of the distribution. When the maritime radar operates at high-resolution and adverse weather conditions, it turns out that the Gaussian model proposed previously can no longer correctly model the amplitude of sea clutter, and the speckle deviates to longer tail distributions as mentioned in chapter 2. Among the proposed models to solve this problem and model the sea clutter with precision is the GC distribution. The GC model is a multi-parameter PDF which is built up using the Generalized Gamma ($G\Gamma$) distribution. Both the speckle and texture component of the compound clutter are described using the $G\Gamma$ PDF. The model lacks a closed-form expression and consequently only integral representation is provided. It turns out that all the statistical models used in the radar literature are special cases of GC distribution, most of these models can be obtained from specific values of its parameters. Table 3.1 illustrates the procedure for obtaining each model, Also, a graphical demonstration of this procedure and the obtained models is shown in Figure 3.1. The GC distribution can be used advantageously to model a high-resolution radar clutter and to deal with the inefficiencies of existing compound models [19].

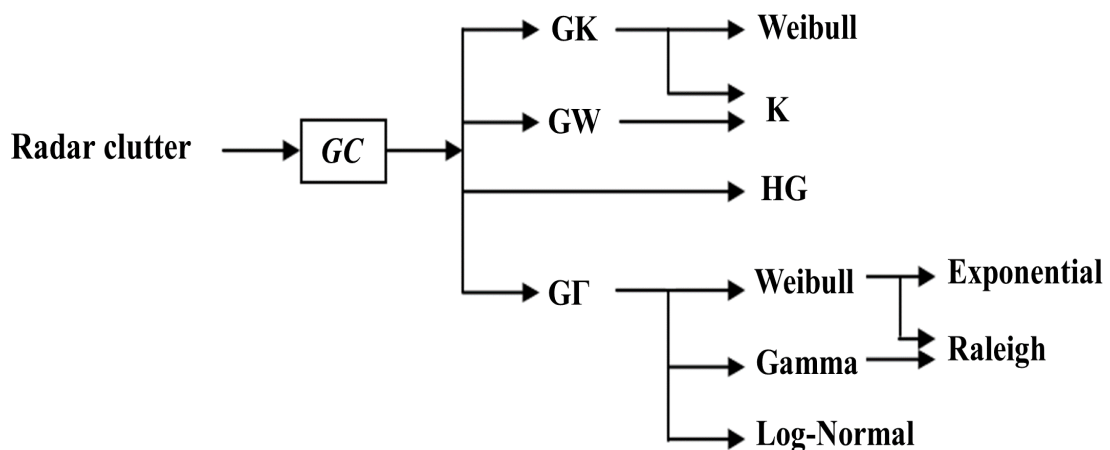


Figure 3.1 – Special cases of GC PDF and existing clutter models.

Moreover, new distributions can be derived from the GC model, the case of our proposed work. First, we start with a detailed description of the GC model without and with thermal noise which will support much of our further analysis, then a statistical description of the proposed models in this thesis.

3.2 Generalized Compound Model without Thermal Noise

The distributions of the speckle and texture components are represented respectively by two distributions of Γ . The PDF of the GC model is given by [19]:

$$f_{GC}(x) = \int_0^{\infty} f_{\Gamma}(x|s)f_{\Gamma}(s)ds \quad (3.1)$$

where $f_{\Gamma}(x|s)$ is the PDF of the speckle, it is described by the Γ distribution given by [19]:

$$f_{\Gamma}(x|s) = \frac{b_1}{a\Gamma(v_1)} \left(\frac{x}{s}\right)^{b_1 v_1 - 1} \exp \left[- \left(\frac{x}{s}\right)^{b_1} \right] \quad (3.2)$$

where b_1 is the power parameter, v_1 is the shape parameter, and s is the scale parameter. The texture is a random variable that also follows the Γ distribution given by the PDF:

$$f_{\Gamma}(s) = \frac{b_2}{a\Gamma(v_2)} \left(\frac{s}{a}\right)^{b_2 v_2 - 1} \exp \left[- \left(\frac{s}{a}\right)^{b_2} \right] \quad (3.3)$$

where b_2 is the power parameter, v_2 is the shape parameter, and a is the scale parameter. Substituting (3.2) and (3.3) into (3.1), we obtain the representation of the PDF- Γ in an integral form.

$$f_{GC}(x) = \frac{b_1 b_2}{\Gamma(v_1)\Gamma(v_2)} \frac{x^{b_1 v_1 - 1}}{a^{b_2 v_2}} \int_0^{\infty} s^{b_2 v_2 - b_1 v_1 - 1} \exp \left[- \left(\frac{x}{s}\right)^{b_1} - \left(\frac{s}{a}\right)^{b_2} \right] ds \quad (3.4)$$

where a is the scale parameter, $b_{1,2}$ are the power parameters, $v_{1,2}$ are the shape parameters. The CDF of the GC distribution is obtained as follows:

$$F_{GC}(x) = 1 - \int_T^{\infty} f_{GC}(x)dx \quad (3.5)$$

$$F_{GC}(x) = 1 - \int_T^{\infty} \left[\int_0^{\infty} f_{\Gamma}(x|s)f_{\Gamma}(s)ds \right] dx \quad (3.6)$$

$$F_{GC}(x) = 1 - \int_0^{\infty} f_{\Gamma}(s) \left[\int_T^{\infty} f_{\Gamma}(x|s)dx \right] ds \quad (3.7)$$

$$F_{GC}(x) = 1 - \int_0^{\infty} f_{\Gamma}(s) [1 - F_{\Gamma}(x|s)] ds \quad (3.8)$$

$F_{\Gamma}(x|s)$ is the CDF of the distribution Γ given by:

$$F_{\Gamma}(x|s) = \frac{\gamma(v_1, (\frac{x}{s})^{b_1})}{\Gamma(v_1)} \quad (3.9)$$

where $(\nu_1, (\frac{x}{s})^{b_1})$ is the incomplete Gamma function.

Finally, the CDF of the GC model without thermal noise is given in integral form by:

$$F_{GC}(x) = 1 - \frac{b_2}{a^{b_2} \nu_2 \Gamma(\nu_2)} \int_0^\infty s^{b_2 \nu_2 - 1} \left[1 - \frac{\gamma(\nu_1, (\frac{x}{s})^{b_1})}{\Gamma(\nu_1)} \right] \exp \left[- \left(\frac{s}{a} \right)^{b_2} \right] ds \quad (3.10)$$

The moments of order n of the GC distribution are obtained from:

$$\langle x^n \rangle = \int_0^\infty x^n f_{GC}(x) dx \quad (3.11)$$

After a few manipulations, $\langle x^n \rangle$ becomes:

$$\langle x^n \rangle = a^n \frac{\Gamma\left(\frac{n}{b_1} + \nu_1\right) \Gamma\left(\frac{n}{b_2} + \nu_2\right)}{\Gamma(\nu_1) \Gamma(\nu_2)} \quad (3.12)$$

Most of the distributions used to model radar clutter can be obtained from the GC model from specific values of its parameters. The procedure for obtaining each distribution is illustrated in table 3.1. The description of each distribution is described below.

Models	Abbreviation	Parameters	Nature		
			Simple	Compound	
				Speckle	Texture
Generalized Compound	GC	$a, \nu_1, \nu_2, b_1, b_2$			
Rayleigh	R	$b_1 = b_2 = 4$ $\nu_1 = 1$ $\nu_2 = 0.5$	*		
Exponential	E	$b_1 = b_2 = 2$ $\nu_1 = 1$ $\nu_2 = 0.5$	*		
K	K	$b_1 = b_2 = 2$ $\nu_1 = 1$ $\nu_2 = \nu$		R	G
Generalized-K	GK	$b_1 = b_2 = b$		$G\Gamma$	$G\Gamma$
Gamma	Γ	$b_1 = b_2 = 2$ $\nu_1 = 1$ $\nu_2 = 0.5$	*		
Generalized Gamma	$G\Gamma$	b_1, b_2 : Integer values	*		
Weibull	W	$b_1 = b_2 = b$ $\nu_1 = 1$ $\nu_2 = 0.5$	*		
Weibull-Gamma	WG	$b_1 = b$ $b_2 = 2$ $\nu_1 = 1$ $\nu_2 = \nu$		W	G
Log-Normal	LN	$b_1 = b_2 = b \rightarrow 0$ $\nu_1 = \nu \rightarrow \infty$ $\nu_2 = 0.5$		$G\Gamma$	$G\Gamma$
Generalized Hyper-geometric.	GH	$b_1 = b_2 = b$	*		

Table 3.1 – The GC model and its derived distributions.

3.2.1 R Distribution

The R distribution is a special case of the GC distribution. It is obtained from the GC model when $b_1 = b_2 = 4$, $v_1 = 1$, and $v_2 = 0.5$. The PDF of the R distribution is given by:

$$f_R(x) = \frac{8}{a\Gamma(0.5)} \left(\frac{x}{a}\right)^2 K_{-0.5} \left(2\left(\frac{x}{a}\right)\right)^2 \quad (3.13)$$

It is also given by the equation:

$$f_R(x) = \frac{4x}{a^2} \exp\left(2\left(\frac{x}{a}\right)\right)^2 \quad (3.14)$$

The CDF of the R distribution is given by:

$$F_R(x) = 1 - \exp\left(2\left(\frac{x}{a}\right)\right)^2 \quad (3.15)$$

Finally, the moments of order n are obtained as:

$$\langle x_R^n \rangle = \left(\frac{a}{\sqrt{2}}\right)^n \Gamma\left(\frac{n}{2} + 1\right) \quad (3.16)$$

3.2.2 E Distribution

The E distribution is a special case of the GC distribution. The E distribution is obtained when $b_1 = b_2 = 2$, $v_1 = 1$, and $v_2 = 0.5$, its PDF is given by:

$$f_E(x) = \frac{4}{a\Gamma(0.5)} \sqrt{\frac{x}{a}} K_{-0.5} \left(\frac{2x}{a}\right) \quad (3.17)$$

It is also given by the equation:

$$f_E(x) = \frac{2}{a} \exp\left(-\frac{2x}{a}\right) \quad (3.18)$$

The CDF of the E distribution is given by:

$$F_E(x) = 1 - \exp\left(-\frac{2x}{a}\right) \quad (3.19)$$

The moments of order n are obtained as:

$$\langle x_E^n \rangle = \left(\frac{a}{2}\right)^n \Gamma(n+1) = \left(\frac{a}{2}\right)^n n! \quad (3.20)$$

3.2.3 K Distribution

This model is mainly presented for high-resolution sea clutter modeling. The K model is a composite Gaussian distribution formed from two components speckle and texture, which are represented respectively by a Rayleigh and Gamma distribution. This model can be obtained from the GC distribution when $b_1 = b_2 = 2$, $v_1 = 1$, and $v_2 = v$. Its PDF is given by:

$$f_K(x) = \frac{4}{a\Gamma(v)} \left(\frac{x}{a}\right)^v K_{v-1}\left(\frac{2x}{a}\right) \quad (3.21)$$

Its CDF is given by:

$$F_K(x) = 1 - \frac{2}{\Gamma(v)} \left(\frac{x}{a}\right)^v K_v\left(\frac{2x}{a}\right) \quad (3.22)$$

The moments of order n are obtained as:

$$\langle x_K^n \rangle = a^n \frac{\Gamma\left(\frac{n}{2} + 1\right) \Gamma\left(\frac{n}{2} + v\right)}{\Gamma(v)} \quad (3.23)$$

3.2.4 Γ Distribution

The Γ distribution is also a special case of the GC distribution. It is obtained from the GC distribution when $b_1 = b_2 = 2$, $v_1 = v$, and $v_2 = 0.5$, its PDF is given by:

$$f_G(x) = \frac{2}{a\Gamma(v)} \left(\frac{2x}{a}\right)^{v-1} \exp\left(-\frac{2x}{a}\right) \quad (3.24)$$

The CDF of distribution Γ is given by:

$$F_G(x) = \frac{\gamma\left(v, \frac{2x}{a}\right)}{\Gamma(v)} \quad (3.25)$$

The moments of order n are obtained from:

$$\langle x_G^n \rangle = \left(\frac{a}{2}\right)^n \frac{\Gamma(n+v)}{\Gamma(v)} \quad n > v \quad (3.26)$$

3.2.5 $G\Gamma$ Distribution

This distribution can be obtained from the GC model when $b_1 = b_2 = b$, $v_1 = v$, and $v_2 = 0.5$, its PDF is given by:

$$f_{G\Gamma}(x) = \frac{b}{2p\Gamma(v)} \left(\frac{x}{p}\right)^{\frac{b}{2}v-1} \exp\left(-\frac{x}{a}\right)^{\frac{b}{2}} \quad (3.27)$$

where $p = a2^{-\frac{b}{2}}$

The function of the CDF is given by:

$$F_{G\Gamma}(x) = \frac{\gamma\left(\nu, \left(\frac{2x}{p}\right)^{\frac{b}{2}}\right)}{\Gamma(\nu)} \quad (3.28)$$

The moments of order n are obtained from:

$$\langle x_{G\Gamma}^n \rangle = p^n \frac{\Gamma\left(\frac{2n}{b} + \nu\right)}{\Gamma(\nu)} \quad (3.29)$$

3.2.6 GK Distribution

For the GK model, the texture component is represented by a $G\Gamma$ distribution. This model is obtained from the GC distribution when $b_1 = b_2 = b$.

The PDF function is provided by:

$$f_{GK}(x) = \frac{2b}{a\Gamma(\nu_1)\Gamma(\nu_2)} \left(\frac{x}{a}\right)^{\frac{b}{2}(\nu_1+\nu_2)-1} K_{\nu_2-\nu_1} \left(2\left(\frac{x}{a}\right)^{\frac{b}{2}}\right) \quad (3.30)$$

where $K_\nu(\cdot)$ is the modified Bessel function of the second kind.

The CDF of the GK distribution is given by:

$$F_{GK}(x) = 1 - \frac{2}{\Gamma(\nu_2)} \left(\frac{x}{a}\right)^{\frac{b}{2}\nu_2} \sum_{q=0}^{\nu_1-1} \frac{1}{q!} \left(\frac{x}{a}\right)^{\frac{b}{2}q} K_{\nu_2-q} \left(2\left(\frac{x}{a}\right)^{\frac{b}{2}}\right) \quad (3.31)$$

The moments of order n are obtained as:

$$\langle x_K^n \rangle = a^n \frac{\Gamma\left(\frac{n}{2} + 1\right) \Gamma\left(\frac{n}{2} + \nu\right)}{\Gamma(\nu_1)\Gamma(\nu_2)} \quad (3.32)$$

3.2.7 W Distribution

This distribution is due to the Swedish mathematician Waloddi Weibull. It is a law of probability which depends on two parameters, and also it is a special case of the GC distribution when $b_1 = b_2 = b$, $\nu_1 = 1$, and $\nu_2 = 0.5$.

Its PDF is given by:

$$f_W(x) = \frac{2b}{a\Gamma(0.5)} \left(\frac{x}{a}\right)^{\frac{3}{4}b-1} K_{0.5} \left(2\left(\frac{x}{a}\right)^{\frac{b}{2}}\right) \quad (3.33)$$

It is also given by the equation:

$$f_W(x) = \frac{b}{2p} \left(\frac{x}{p}\right)^{\frac{b}{2}-1} \exp\left(-\frac{x}{p}\right)^{\frac{b}{2}} \quad (3.34)$$

where $p = a2^{-\frac{b}{2}}$.

The function of the CDF is given by:

$$F_W(x) = 1 - \exp\left(-\frac{x}{p}\right)^{\frac{b}{2}} \quad (3.35)$$

The moments of order n are obtained as:

$$\langle x_W^n \rangle = a^n \frac{\Gamma\left(\frac{n}{b} + 1\right) \Gamma\left(\frac{n}{b} + 0.5\right)}{\Gamma(0.5)} \quad (3.36)$$

It is also given by the equation:

$$\langle x_W^n \rangle = p^n \Gamma\left(\frac{2n}{p} + 1\right) \quad (3.37)$$

3.2.8 WG Distribution

The WG distribution is composed of a speckle distributed according to Weibull and a texture distributed according to Gamma. It is more general than the K distribution with regard to the speckle. The WG model is obtained from the GC distribution when $b_1 = b, b_2 = 2, v_1 = 1,$ and $v_2 = v,$ its PDF is given by:

$$f_{WG}(x) = \frac{2\pi}{2\Gamma(v)} \left(\frac{x}{a}\right)^{b-1} \sum_{k=0}^{\infty} \frac{\frac{(-1)^k}{k!} \left(\frac{x}{a}\right)^{bz_1}}{\Gamma(z_1 + 1) \sin[\pi(z_1 + 1)]} + \frac{b\pi}{a\Gamma(v)} \left(\frac{x}{a}\right)^{2v-1} \sum_{k=0}^{\infty} \frac{\frac{(-1)^k}{k!} \left(\frac{x}{a}\right)^{bz_2}}{\Gamma(z_2 + 1) \sin[\pi(z_2 + 1)]} \quad (3.38)$$

where $z_1 = \frac{2v-b+2k}{b}$ and $z_2 = \frac{b-2v+kb}{2}$.

The function of the CDF of the WG distribution is given by:

$$F_{WG}(x) = 1 - \left(\frac{2}{a^{2v}\Gamma(v)}\right) \int_0^{\infty} s^{2v-1} \left(1 - \gamma\left(1, \left(\frac{x}{s}\right)^b\right)\right) \exp\left(-\left(\frac{s}{a}\right)^2\right) ds \quad (3.39)$$

The moments of order n are obtained from:

$$\langle x_{WG}^n \rangle = a^n \frac{\Gamma\left(\frac{n}{b} + 1\right) \Gamma\left(\frac{n}{2} + v\right)}{\Gamma(v)} \quad (3.40)$$

3.2.9 LN Distribution

The LN distribution has been developed to be applied in a wide variety of real situations of the sea and land clutter at a low angle and high-resolution radars. The LN distribution is obtained from the GC distribution when: $b_1 = b_2 = b \rightarrow 0, v_1 = v \rightarrow \infty,$ and $v_2 = 0.5,$ its

PDF is given by:

$$f_{LN}(x) = \frac{1}{x\sigma_{LN}\sqrt{2\pi}} \exp \left[-\frac{1}{2} \left(\frac{\log(x) - \mu_{LN}}{\sigma_{LN}} \right)^2 \right] \quad (3.41)$$

where $\mu_{LN} = \log(a2^{-\frac{2}{b}}) + \frac{2}{b}\log(v)$ and $\sigma_{LN} = \frac{2}{b\sqrt{v}}$.

The CDF of the LN distribution is given by:

$$F_{LN}(x) = \frac{1}{2} \left[1 + \operatorname{erf} \left(\frac{\log(x) - \mu_{LN}}{\sigma_{LN}\sqrt{2}} \right) \right] \quad (3.42)$$

The moments of order n are obtained from:

$$\langle x_{LN}^n \rangle = \exp \left(n\mu_{LN} + \frac{(n\sigma_{LN})^2}{2} \right) \quad (3.43)$$

3.2.10 GH Distribution

Other special cases of GC model can be obtained when b_1 et b_2 take integer values by using the Hyper-geometric Generalized functions. We present here two special cases, $b_1 = 1$, $b_2 = 2$, and $b_1 = 2$, $b_2 = 1$. The same procedure can be followed for any pair [19]. In the first case, we assume that $b_1 = 1$, so the speckle is Gamma distributed, and $b_2 = 2$. In this case, we denote the distribution GH by GH1, its PDF is given by:

$$\begin{aligned} f_{GH1}(x) = & A_1 \left(\frac{x}{a} \right)^{2\nu_2-1} {}_0F_2 \left(\nu_2 - \frac{\nu_1}{2} + 0.5; \nu_2 - \frac{\nu_1}{2} + 1; - \left(\frac{x}{2a} \right)^2 \right) \\ & + A_2 \left(\frac{x}{a} \right)^{\nu_1-1} {}_0F_2 \left(0.5; -\nu_2 + \frac{\nu_1}{2} + 1; - \left(\frac{x}{2a} \right)^2 \right) \\ & + A_3 \left(\frac{x}{a} \right)^{\nu_1} {}_0F_2 \left(1.5; -\nu_2 + \frac{\nu_1}{2} + 1.5; - \left(\frac{x}{2a} \right)^2 \right) \end{aligned} \quad (3.44)$$

where the A_i are quantities depending on ν_1, ν_2 , and a . ${}_pF_q$ are the Generalized Hyper-geometric functions.

$$A_1 = \frac{2\pi}{a\Gamma(\nu_1)\Gamma(\nu_2)\Gamma(2\nu_2 - \nu_1 + 1)\sin[\pi(2\nu_2 - \nu_1 + 1)]} \quad (3.45)$$

$$A_2 = \frac{\pi^{1.5}}{a\Gamma(\nu_1)\Gamma(\nu_2)\Gamma(\frac{1}{2})\Gamma(-\nu_2 + \frac{\nu_1}{2} + 1)\sin[\pi(-\nu_2 + \frac{\nu_1}{2} + 1)]} \quad (3.46)$$

$$A_3 = \frac{\pi^{1.5}}{2a\Gamma(\nu_1)\Gamma(\nu_2)\Gamma(\frac{3}{2})\Gamma(-\nu_2 + \frac{\nu_1}{2} + \frac{3}{2})\sin[\pi(-\nu_2 + \frac{\nu_1}{2} + \frac{1}{2})]} \quad (3.47)$$

The CDF of the GH1 distribution is given by:

$$F_{GH_1}(x) = 1 - \frac{2}{a^{2\nu_2}\Gamma(\nu_2)} \int_0^\infty s^{2\nu_2-1} \left(1 - \frac{\gamma(\nu_1, \frac{x}{s})}{\Gamma(\nu_1)} \right) \exp\left(-\left(\frac{s}{a}\right)^2\right) ds \quad (3.48)$$

The moments of order n are obtained from:

$$\langle x_{GH_1}^n \rangle = a^n \frac{\Gamma(n + \nu_1) \Gamma\left(\frac{n}{2} + \nu_2\right)}{\Gamma(\nu_1)\Gamma(\nu_2)} \quad (3.49)$$

In the second case, we assume that $b_1 = 2$ and $b_2 = 1$. In this case, we denote the distribution GH by GH2, its PDF is given by:

$$\begin{aligned} f_{GH_2}(x) = & B_1 \left(\frac{x}{a}\right)^{2\nu_2-1} {}_0F_2\left(\nu_1 - \frac{\nu_2}{2} + 0.5; \nu_1 - \frac{\nu_2}{2} + 1; -\left(\frac{x}{2a}\right)^2\right) \\ & + B_2 \left(\frac{x}{a}\right)^{\nu_2-1} {}_0F_2\left(0.5; -\nu_1 + \frac{\nu_2}{2} + 1; -\left(\frac{x}{2a}\right)^2\right) \\ & + B_3 \left(\frac{x}{a}\right)^{\nu_2} {}_0F_2\left(1.5; -\nu_1 + \frac{\nu_2}{2} + 1.5; -\left(\frac{x}{2a}\right)^2\right) \end{aligned} \quad (3.50)$$

where the B_i are quantities depending on ν_1, ν_2 , and a .

$$B_1 = \frac{2\pi}{a\Gamma(\nu_1)\Gamma(\nu_2)\Gamma(2\nu_1 - \nu_2 + 1)\sin[\pi(2\nu_1 - \nu_2 + 1)]} \quad (3.51)$$

$$B_2 = \frac{\pi^{1.5}}{a\Gamma(\nu_1)\Gamma(\nu_2)\Gamma\left(\frac{1}{2}\right)\Gamma(-\nu_1 + \frac{\nu_2}{2} + 1)\sin[\pi(-\nu_1 + \frac{\nu_2}{2} + 1)]} \quad (3.52)$$

$$B_3 = \frac{\pi^{1.5}}{2a\Gamma(\nu_1)\Gamma(\nu_2)\Gamma\left(\frac{3}{2}\right)\Gamma(-\nu_1 + \frac{\nu_2}{2} + \frac{3}{2})\sin[\pi(-\nu_1 + \frac{\nu_2}{2} + \frac{1}{2})]} \quad (3.53)$$

The CDF of the GH2 distribution is given by:

$$F_{GH_2}(x) = 1 - \frac{1}{a^{2\nu_2}\Gamma(\nu_2)} \int_0^\infty s^{\nu_2-1} \left(1 - \frac{\gamma\left(\nu_1, \left(\frac{x}{s}\right)^2\right)}{\Gamma(\nu_1)} \right) \exp\left(-\left(\frac{s}{a}\right)^2\right) ds \quad (3.54)$$

The moments of order n are obtained from:

$$\langle x_{GH_2}^n \rangle = a^n \frac{\Gamma(n + \nu_2) \Gamma\left(\frac{n}{2} + \nu_1\right)}{\Gamma(\nu_1)\Gamma(\nu_2)} \quad (3.55)$$

3.3 Generalized Compound Model with Thermal Noise

In the case of the presence of thermal noise, the speckle and texture components of the GC clutter are modeled by different PDFs. For this reason, the speckle distribution (3.2) has been adjusted to include thermal noise, and noted GFN.

$$f_{GFN}(x|s) = \frac{b_1}{\Gamma(v_1)} \frac{x^{b_1 v_1 - 1}}{\sqrt{s^2 + 2\sigma^2}^{b_1 v_1}} \exp \left[-\left(\frac{x}{\sqrt{s^2 + 2\sigma^2}} \right)^{b_1} \right] \quad (3.56)$$

Therefore, the PDF model GC plus thermal noise (GCN) is given by:

$$f_{GCN}(x) = \frac{b_1 b_2}{\Gamma(v_1) \Gamma(v_2)} \frac{x^{b_1 v_1 - 1}}{a^{b_2 v_2}} \int_0^\infty \frac{s^{b_2 v_2 - 1}}{\sqrt{s^2 + 2\sigma^2}^{b_1 v_1}} \exp \left[-\left(\frac{x}{\sqrt{s^2 + 2\sigma^2}} \right)^{b_1} - \left(\frac{s}{a} \right)^{b_2} \right] ds \quad (3.57)$$

After some mathematical simplifications, the CDF function is given by:

$$F_{GCN}(x) = 1 - \frac{b_2}{a^{b_2 v_2} \Gamma(v_2)} \int_0^\infty s^{b_2 v_2 - 1} \left[1 - \frac{\gamma \left(v_1, \left(\frac{x}{\sqrt{s^2 + 2\sigma^2}} \right)^{b_1} \right)}{\Gamma(v_1)} \right] \exp \left[-\left(\frac{s}{a} \right)^{b_2} \right] ds \quad (3.58)$$

The moments are given by:

$$\langle x^n_{GCN} \rangle = \frac{b_2 \Gamma \left(\frac{n}{b_1} + v_1 \right)}{\Gamma(v_1) \Gamma(v_2) a^{b_2 v_2}} \int_0^\infty \sqrt{s^2 + 2\sigma^2}^n s^{b_2 v_2 - 1} \exp \left[-\left(\frac{s}{a} \right)^{b_2} \right] ds \quad (3.59)$$

As mentioned above, new distributions can be derived from the GC model. In our work, we derive the CCDF of the Weibull model with additive thermal noise based on the GC distribution, as detailed below.

3.4 First Weibull Model plus Thermal Noise

The first approximate Weibull plus noise model referred to as WN1 is based on the GCN. It is obtained for $b_1 = b_2 = b$, $v_1 = 1$, and $v_2 = 0.5$ [19]. For this model, we derive the expressions of the CCDF for single as well as multiple pulses.

3.4.1 The WN1 Model for a Single Pulse

The PDF of the WN1 for a single pulse is given by:

$$f_{WN1}(x) = \frac{b^2}{\sqrt{\pi}} \frac{x^{b-1}}{a} \int_0^\infty \left(\frac{s}{a} \right)^{\frac{b}{2}-1} \frac{1}{\sqrt{s^2 + 2\sigma^2}^b} \exp \left[-\left(\frac{x}{\sqrt{s^2 + 2\sigma^2}} \right)^b - \left(\frac{s}{a} \right)^b \right] ds \quad (3.60)$$

After some simplifications, the CCDF of the WN1 model for a single pulse is expressed by:

$$CCDF_{WN1} = Prob(x > T) = \frac{b}{a^{\frac{b}{2}} \sqrt{\pi}} \int_0^{\infty} s^{\frac{b}{2}-1} \left[1 - \gamma \left(1, \left(\frac{T}{\sqrt{s^2 + 2\sigma^2}} \right)^b \right) \right] \exp \left[-\left(\frac{s}{a} \right)^b \right] ds \quad (3.61)$$

Using a detection threshold T ($T = \alpha \langle x \rangle$), the probability that clutter returns exceed the threshold is given as the CCDF, where α is a factor which is set to achieve the desired value of (P_{FA}). The shape and scale parameters are given respectively by:

$$c = 0.5b, \text{ and } \beta = a2^{-2/b} [19].$$

The expression of the moments of the WN1 distribution is called MoM-WN1 and is given by [19]:

$$\langle x_{WN1}^n \rangle = \frac{\Gamma(\frac{n}{b} + 1)^b}{\sqrt{\pi} a^{\frac{b}{2}}} \int_0^{\infty} \left(\sqrt{w^2 + 2\sigma^2} \right)^n s^{\frac{b}{2}-1} \exp \left(-\left(\frac{s}{a} \right)^b \right) ds \quad (3.62)$$

3.4.2 The WN1 Model for Multiple Pulse

Based on the PDF approximation of the sum of N Weibull distribution mentioned in [36], where the approximation is of $G\Gamma$ type:

$$f(x) = \frac{Rbc^N}{\Gamma(N)} (Rx)^{Nb-1} \exp \left(-c(Rx)^b \right) \quad (3.63)$$

$$R = \frac{\Gamma(N + \frac{1}{b})}{N\Gamma(N)\Gamma(1 + \frac{1}{b})} \quad (3.64)$$

We can write the formula of the sum of N PDF of the WN1 model:

$$Nf_{WN1}(x) = \frac{Rb^2(Rx)^{Nb-1}}{\Gamma(N)a\sqrt{\pi}} \int_0^{\infty} \left(\frac{s}{a} \right)^{\frac{b}{2}-1} \frac{1}{\sqrt{s^2 + 2\sigma^2}^{Nb}} \exp \left[-\left(\frac{Rx}{\sqrt{s^2 + 2\sigma^2}} \right)^b - \left(\frac{s}{a} \right)^b \right] ds \quad (3.65)$$

After some simplifications, the sum of N CCDF of WN1 is expressed by:

$$NCCDF_{WN1} = Prob(x > T) = \frac{b}{a^{\frac{b}{2}} \sqrt{\pi}} \int_0^{\infty} s^{\frac{b}{2}-1} \left[1 - \frac{\gamma \left(N, \left(\frac{RT}{\sqrt{s^2 + 2\sigma^2}} \right)^b \right)}{\Gamma(N)} \right] \exp \left[-\left(\frac{s}{a} \right)^b \right] ds \quad (3.66)$$

Putting $N = 1$ leads to the WN1 model for a single pulse (3.60) and (3.61).

3.5 Second Weibull Model plus Thermal Noise

The second approximate Weibull plus noise model referred to as WN2 is based on the PDF model provided in [20]. For the WN2 model, we derive the expression of the CCDF for single as well as multiple pulses, and we provide the expression of the moments.

3.5.1 The WN2 Model for Single Pulse

The PDF of the WN2 model is given by [20]:

$$f_{WN2}(x) = \frac{2b}{x\sqrt{\pi}} \varepsilon \alpha \int_0^{\infty} \frac{1}{(w^{\frac{4}{b}} + 1)^{\frac{b}{2}}} \exp \left[-\frac{\varepsilon}{(w^{\frac{4}{b}} + 1)^{\frac{b}{2}}} - (\alpha^2 w^2) \right] dw \quad (3.67)$$

where $\varepsilon = (x^2/2\sigma^2)^{\frac{b}{2}}$ and $\alpha = (2\sigma^2/a^2)^{\frac{b}{4}}$. The shape and scale parameters are given respectively by:

$$c = 0.5b, \beta = a2^{-2/b}.$$

The CCDF of the WN2 model is derived in the same manner as for the WN1 model. After some mathematical manipulations, the CCDF for a single pulse is expressed in the integral form as follows:

$$CCDF_{WN2} = Prob(x > T) = \frac{2\alpha}{\sqrt{\pi}} \int_0^{\infty} \exp \left[-\frac{T^b}{(2\sigma^2)^{\frac{b}{2}}(w^{\frac{4}{b}} + 1)^{\frac{b}{2}}} - (\alpha^2 w^2) \right] dw \quad (3.68)$$

The expression of the moments of the WN2 model is referred to as MoM-WN2 can be obtained, using the conventional definition and (3.67) as follows:

$$\langle x^n \rangle = \int_0^{\infty} x^n f_{WN2}(x) dx \quad (3.69)$$

Integrating with respect to x , we obtain after some manipulations the following expression in the integral form:

$$\langle x^n \rangle = \frac{2\alpha}{\sqrt{\pi} 2^{\frac{b}{2}} \sigma^b} \Gamma\left(\frac{n}{b} + 1\right) \int_0^{\infty} \left[2^{\frac{b}{2}} \sigma^b (w^{\frac{4}{b}} + 1)^{\frac{b}{2}} \right]^{\frac{n}{b} + 1} \frac{\exp(-\alpha^2 w^2)}{(w^{\frac{4}{b}} + 1)^{\frac{b}{2}}} dw \quad (3.70)$$

3.5.2 The WN2 Model for Multiple Pulse

Based on the approximation (3.63), the formula of the sum of N PDF is given by:

$$Nf_{WN2}(x) = \frac{2b\alpha}{\Gamma(N)x\sqrt{\pi}} \left(\frac{R^2 x^2}{2\sigma^2} \right)^{\frac{Nb}{2}} \int_0^{\infty} \frac{1}{(w^{\frac{4}{b}} + 1)^{\frac{Nb}{2}}} \exp \left[-\frac{\left(\frac{R^2 x^2}{2\sigma^2} \right)^{\frac{b}{2}}}{(w^{\frac{4}{b}} + 1)^{\frac{b}{2}}} - (\alpha^2 w^2) \right] dw \quad (3.71)$$

After some mathematical manipulations, the expression of the sum of N CCDF is expressed by:

$$NCCDF_{WN2} = Prob(x > T) = \frac{2R^{Nb} \alpha (2\sigma^2)^{\frac{b}{2}}}{\Gamma(N) \sqrt{\pi} (2\sigma^2)^{\frac{Nb}{2}}} \int_0^{\infty} \frac{(w^{\frac{4}{b}} + 1)^{\frac{b}{2}}}{(w^{\frac{4}{b}} + 1)^{\frac{Nb}{2}}} \exp \left[-\frac{R^b T^b}{(2\sigma^2)^{\frac{b}{2}} (w^{\frac{4}{b}} + 1)^{\frac{b}{2}}} - (\alpha^2 w^2) \right] dw \quad (3.72)$$

Putting $N = 1$ leads to the WN2 model for a single pulse (3.67) and (3.68)

3.5.3 The Compound Gaussian plus Noise Models

To assess the performance of the proposed models to fit sea clutter amplitudes, three important CG distributions plus noise are recalled here and used for comparison purposes and are considered among the most suitable models to describe the sea clutter. The fitting performance of these models has been studied and discussed by Mezache *et al* in [31]. The first model is the K distribution plus noise (KN). The overall PDF and CCDF are given by:

$$f_{KN}(x) = \int_0^\infty \frac{x}{\sigma^2 + 2y^2/\pi} \exp\left[-\frac{x^2}{2\sigma^2 + 4y^2/\pi}\right] \frac{2b^{2\nu}y^{2\nu-1}}{\Gamma(\nu)} \exp(-b^2y^2) dy \quad (3.73)$$

$$CCDF_{KN} = Prob(x > T) = \int_0^\infty \exp\left[-\frac{T^2}{2\sigma^2 + 4y^2/\pi}\right] \frac{2b^{2\nu}y^{2\nu-1}}{\Gamma(\nu)} \exp(-b^2y^2) dy \quad (3.74)$$

where ν is the shape parameter, b is the scale parameter, $2\sigma^2$ is the power of thermal noise, and T is the detection threshold as mentioned above. The second model is the GP distribution plus thermal noise (GPN). Its PDF and CCDF are expressed respectively by:

$$f_{GPN}(x) = \int_0^\infty \frac{x}{\sigma^2 + 2y^2/\pi} \exp\left[-\frac{x^2}{2\sigma^2 + 4y^2/\pi}\right] \frac{b^\alpha y^{-\alpha-1}}{\Gamma(\alpha)} \exp\left[-\frac{b}{y}\right] dy \quad (3.75)$$

$$CCDF_{GPN} = Prob(x > T) = \int_0^\infty \exp\left[-\frac{T^2}{2\sigma^2 + 4y^2/\pi}\right] \frac{b^\alpha y^{-\alpha-1}}{\Gamma(\alpha)} \exp\left[-\frac{b}{y}\right] dy \quad (3.76)$$

where α is the shape parameter, b is the scale parameter, and $2\sigma^2$ is the power of thermal noise. The last model is the CIG distribution plus thermal noise (CIGN). Its PDF and CCDF are given respectively by:

$$f_{CIGN}(x) = \int_0^\infty \frac{x}{\sigma^2 + 2y^2/\pi} \exp\left[-\frac{x^2}{2\sigma^2 + 4y^2/\pi}\right] \frac{\lambda^{\frac{3}{2}}}{\sqrt{2\pi}y^{\frac{3}{2}}} \exp\left[-\lambda \frac{(y-\mu)^2}{2\mu^2y}\right] dy \quad (3.77)$$

$$CCDF_{CIGN} = Prob(x > T) = \int_0^\infty \exp\left[-\frac{T^2}{2\sigma^2 + 4y^2/\pi}\right] \frac{\lambda^{\frac{3}{2}}}{\sqrt{2\pi}y^{\frac{3}{2}}} \exp\left[-\lambda \frac{(y-\mu)^2}{2\mu^2y}\right] dy \quad (3.78)$$

where λ is the shape parameter, μ is mean, and $2\sigma^2$ is the power of thermal noise.

3.6 Simulation Results and Discussions

As mentioned in chapter 2, the statistics of the sea clutter deviate from the Gaussian model and the returns have a high amplitude which generally lead to the appearance of the target of interest in the tail of the clutter distribution. Therefore, modern radars need more fitted models with longer tails. In the field of radar clutter design and modeling, it is essential to verify and validate new models using synthetic and real data. Without this step, there is no guarantee that the results will have any value. Several real radar databases are used as part of high-resolution sea clutter modeling, among them is the database collected by the IPIX radar from McMaster University. This database offers a wide possibility to model, test and analyze sea clutter in different resolution ranges and different conditions. In this section, For a single pulse, we assess the performance of the proposed models to fit sea clutter. Two types of sea clutter data are used, synthetic data and real IPIX data. The estimated parameters of each model are obtained using the PCFE method based on the N-M simplex algorithm.

3.6.1 Parameter Estimation by the PCFE Method

The detection process is related to the parameters of the clutter model used in the radar system. In reality, the true values of these parameters are unknown, they are only estimates and should be calculated optimally or at least be close to their theoretical values, in order to improve detection performance. Since the nature of the clutter can only provide partial information about reality, the estimated values will inevitably encounter errors, where they should be reduced as much as possible. Due to the complexity of parameter estimation according to the proposed models, the PCFE method based on the N-M algorithm is used here to reach the estimation parameters. The N-M algorithm is often referred to as the simplex method, this algorithm was published in 1965 by John Nelder and Roger Mead, and since then it has become one of the most common unconstrained nonlinear optimization methods. The algorithm is quite simple to understand and very easy to use. For these reasons it is very popular in many fields of science and technology. The algorithm tends to minimize a nonlinear scalar function of N parameters without the use of derivative, which makes it suitable for problems with non-smooth functions. It is widely used to solve parameter estimation, where the function values are unknown. It can also be used for problems with discontinuous functions, which frequently arise in statistics and experimental mathematics. The main steps of the PCFE method based on the N-M algorithm are summarized as follows [30]:

Step 1: Estimate the real CCDF (P_{FA}) of the recorded IPIX data.

Step 2: Initialize the method.

Step 3: Compute the initial working N-M simplex.

Step 4: Evaluate the summed square of residuals at each vertex of the working N-M simplex.

Step 5: Repeat the following steps until the termination test is satisfied.

- Calculate the termination test information.
- If the termination test is satisfied then, accept the best vertex of the working N-M simplex and go to next step, otherwise transform the working N-M simplex and go to step 4.

Step 6: Return the best vertex of the working N-M simplex and the associated fitness function.

In addition, if the best fit curve is reached, we can accept the estimated parameters. Otherwise, we may have to take more steps to improve the estimation quality, for instance, we may look for an adequate region to improve curve fitting or repeat the data collection process to get better results. It is clear that choosing the best model from a group of candidates for a particular set of data is not an easy task. The most suitable model gives predicted values close to the observed data values. Although often overlooked, the metric used to assess the effectiveness of a model in predicting outcomes is very important and can influence conclusions. Currently, there are several criteria in the literature to choose the model that best matches the data. Among them are the Mean Squared Error (MSE) and the Chi-Square goodness-of-fit (CS) test. The MSE criterion is used here to assess the goodness of fit of theoretical CCDFs to actual CCDFs, and the CS criterion to assess the goodness of fit between theoretical and actual PDFs.

3.6.1.1 The MSE Criterion

MSE is probably the most widely used quantitative criterion for comparing calculated and observed values. For each observation we take the difference between the calculated value and the observed value (this is the error of the model), we take the square, and finally we take the average of the squares over all the observations. the MSE criterion is defined as follows:

$$MSE = \frac{1}{N} \sum_{i=1}^N (CCDF_{real_i} - CCDF_i)^2 \quad (3.79)$$

3.6.1.2 The CS Criterion

The CS adjustment test can be defined as:

$$CS = \sum_{i=1}^N (PDF_{real_i} - PDF_i)^2 / PDF_i \quad (3.80)$$

3.6.2 Fitting via Synthetic Data

In this subsection, we illustrate the results of clutter modeling when the distribution is selected in advance. For that, we generate sea clutter distributed according to the Weibull

model plus additive thermal noise which depends on the shape parameter and the CNR.

$$CNR = \frac{\beta^2 \Gamma(1 + \frac{2}{c})}{p_n} \quad (3.81)$$

where β is the scale parameter, c is the shape parameter, and $p_n = 2\sigma^2$ is the power of thermal noise.

In Figures 3.2 and 3.3, the Weibull distributed data were obtained assuming $CNR = -5$ dB, $c = 1$, and 60 000 samples (we chose this number as the same number of samples for each range of cells of the IPIX database, as described in the next subsection). We clearly observe that the proposed CCDFs of WN1 and WN2 models follow exactly the curve synthesized from the simulated data and provide accurate tails. Moreover, the PDF curves offer a good fit to the simulated PDF, but with less accurately than the proposed CCDFs. The same performance is observed in Figures 3.4 and 3.5 with $CNR = 10$ dB, and $c = 1$. For MoM-WN1 and MoM-WN2 curves, the estimated parameters are obtained using the moments matching method given by expression (3.62) and the proposed expression (3.70) corresponding to WN1 and WN2 models respectively. Three order moments are used 1, 0.5 and 0.1. The use of low order moments allows reaching a better accuracy, the CCDF curves are very close to that obtained from synthetic data especially in the tail region. According to the obtained results, we can conclude that the two proposed CCDFs WN1 and WN2 provide a good approximation for the Weibull plus thermal noise distribution and offer a better fit than the PDF models.

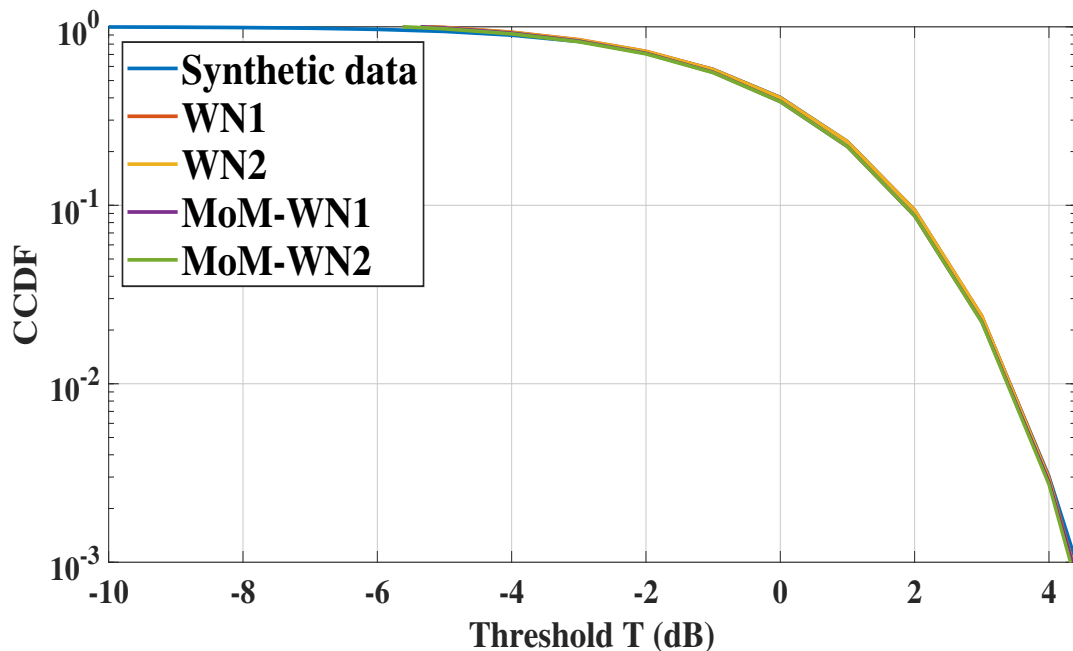


Figure 3.2 – CCDF curves via synthetic data for $CNR = -5$ dB, $c = 1$, $\beta = 0.3466$ and $p_n = 1.1543$.

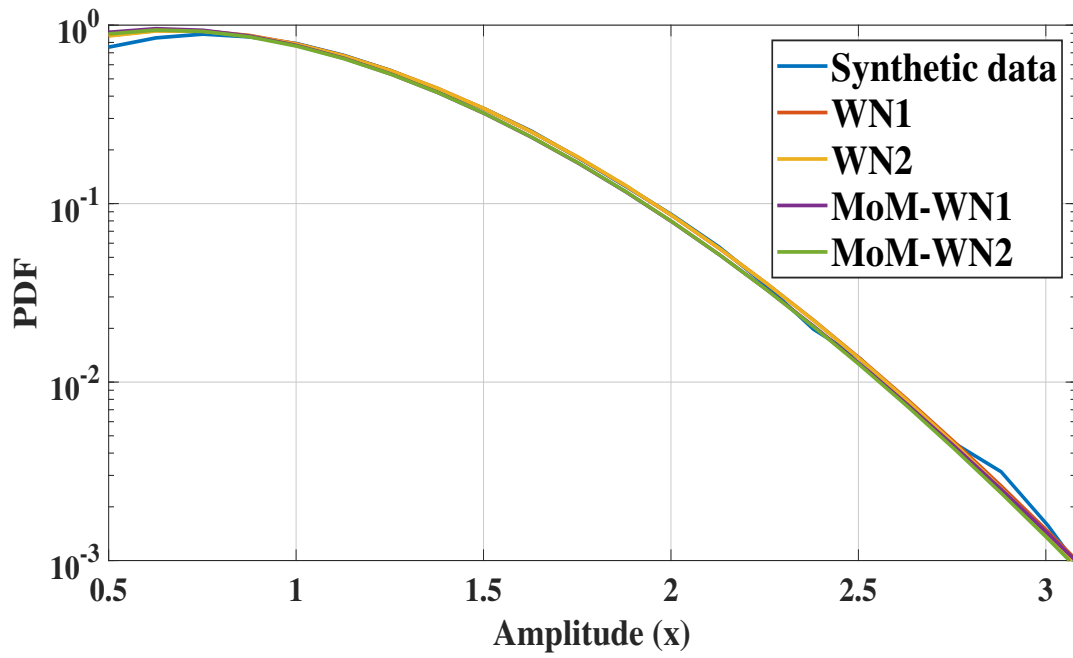


Figure 3.3 – PDF curves via synthetic data for $\text{CNR} = -5$ dB and $c = 1$, $\beta = 0.3466$ and $p_n = 1.1543$.

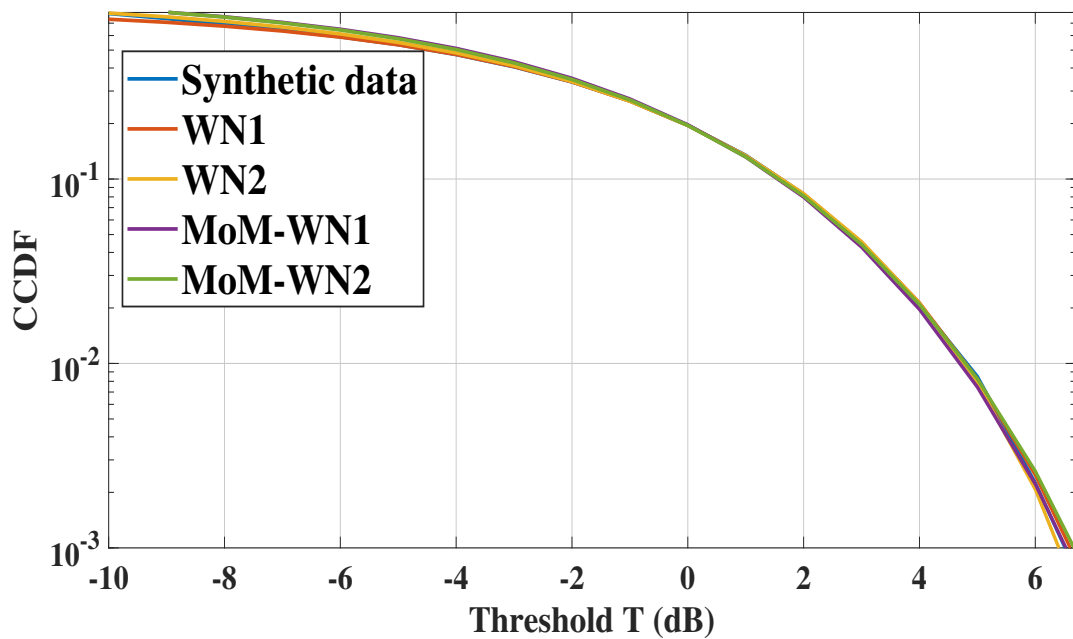


Figure 3.4 – CCDF curves via synthetic data for $\text{CNR} = 10$ dB and $c = 1$, $\beta = 0.6742$ and $p_n = 0.0165$.

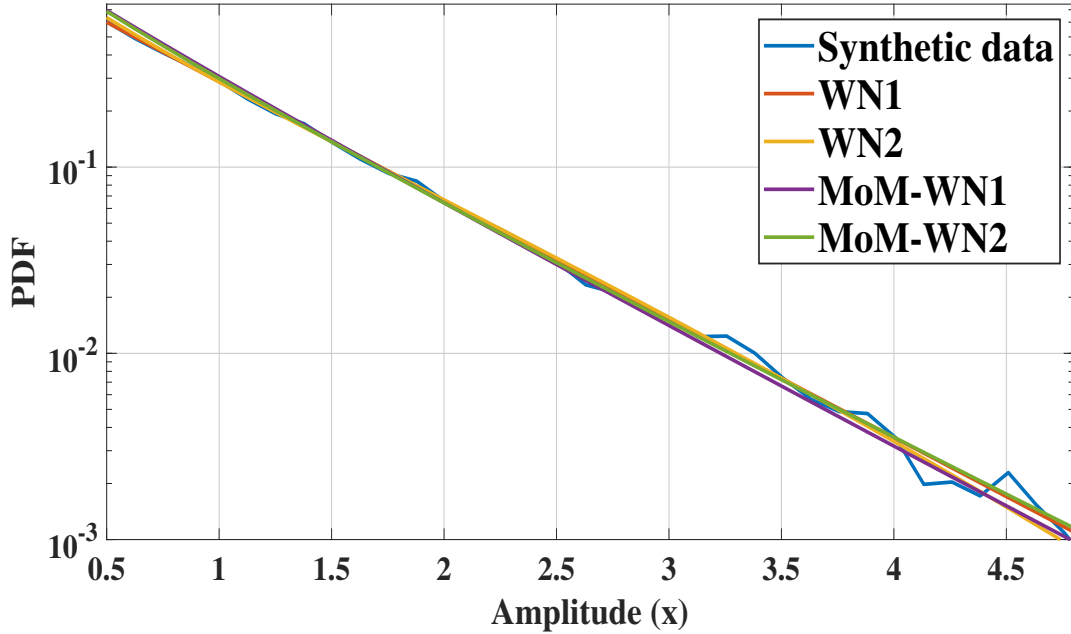


Figure 3.5 – PDF curves via synthetic data for CNR = 10 dB and $c = 1$, $\beta = 0.6742$ and $p_n = 0.0165$.

3.6.3 Modeling Using Real Sea IPIX Data

In this subsection, we assess the fitting performance of the proposed models WN1 and WN2 to real sea data, by comparing the real CCDFs and PDFs with the estimated CCDFs and PDFs using the PCFE method. Also, we compare these results with those obtained by the CG models KN, GPN and CIGN studied in [31]. The sea data processed in this work were collected by the McMaster University IPIX radar on the east coast of Canada, Place Polonaise, Grimsby, Ontario (latitude 43.2114° N, longitude 79.5985° W) at a height of 20 meters [37]. The data are stored in 222 files, there are like-polarization mode, VV and HH (Lpol), and cross-polarization mode, VH and HV (Xpol), with coherent reception, offer four values of I (in-phase) and Q (quadrature) components for each range. In this work, we have selected seven files at a different range of resolutions 60, 30, 15, 9 and 3 meters with four polarization modes. The number of range cells is 27, 28 and 34 depending on the file with 60 000 pulses for each range. The amplitude of the sea clutter is calculated from I and Q components $x = \sqrt{I^2 + Q^2}$. The data has already been processed to eliminate DC offset and phase imbalance due to hardware defects [38]. We use the Kernel smoothing density estimation method to calculate the real PDF [39]. The parameters of the radar system and the characteristics of each file used in this work are available in Table 3.2 and 3.3, All details on the parameters of the radar system are available in [37]. The IPIX radar files are stored in Unidata's NetCDF (Network Common Data Form) file format, this format is ideal for efficient storage of multidimensional array data.

NetCDF is a set of software libraries and machine independent data formats that support the creation, access, and sharing of array oriented scientific data. The Unidata program center supports and maintains NetCDF programming interfaces for C, C++, Java, and Fortran, programming interfaces are also available for Python, IDL, MATLAB, R, Ruby, and Perl. The IPIX data are easily imported into MATLAB using the SNCTOOLS (MexCDF toolbox). Where the SNCTOOLS is a collection of MATLAB codes that were written to provide read, write and access to NetCDF files. To combine SNCTOOLS with Matlab to open, read, and extract IPIX data, must follow the steps mentioned in [37, 40].



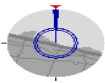
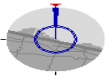
Name of the data set	19980204_221307_ANTSTEP	19980204_194537_ANTSTEP	19980204_221700_ANTSTEP	19980204_221908_ANTSTEP
Data collection date	1998/02/04 22:13:07	1998/02/04 19:45:37	1998/02/04 22:17:00	1998/02/04 22:19:08
Range resolution	60m	30m	15m	9m
Numbre of range cells	28	28	28	28
Cell samples	60 000	60 000	60 000	60 000
PRF	1 KHz	1 KHz	1 KHz	1 KHz
Frequency PRF	9.39 GHz	9.39 GHz	9.39 GHz	9.39 GHz
Pulse length	400 ns	200 ns	100 ns	60 ns
Azimuth resolution	0.3571°	16.1499°	0.2966°	0.3241°
Unambig velocity	7.9872 m/s	7.9872 m/s	7.9872 m/s	7.9872 m/s
Radar and wave geometry				

Table 3.2 – Characteristics of the analyzed files.


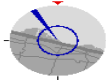
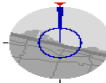
Name of the data set	19980205_185111_ANTSTEP	19980223_190901_ANTSTEP	19980204_222110_ANTSTEP
Data collection date	1998/02/05 18:51:11	1998/02/23 19:09:01	1998/02/04 22:21:10
Range resolution	3m	3m	3m
Numbre of range cells	27	34	27
Cell samples	60 000	60 000	60 000
PRF	1 KHz	1 KHz	1 KHz
Frequency PRF	9.39 GHz	9.39 GHz	9.39 GHz
Pulse length	20 ns	20 ns	20 ns
Azimuth resolution	44.8956°	329.87°	0.31311°
Unambig velocity	7.9872 m/s	7.9872 m/s	7.9872 m/s
Radar and wave geometry			

Table 3.3 – Characteristics of the analyzed files.

3.6.3.1 Range Resolutions 60, 30 and 15m

First, we perform the fitting performance when the radar operates at a low resolution of 60m, using (19980204_221307_ANTSTEP) file, in which the azimuth resolution is set 0.3571° . For HH polarization mode and 4th range cells. Figures 3.6 and 3.7 show the real and the estimated CCDFs and PDFs respectively. A very good fit was achieved by all models to real IPIX data, especially in the tail region, where the CCDFs of the proposed WN1 and WN2 models provide the best approximation with the smallest MSE values, (Table 3.4). On the contrary, all the PDF models show less accurate performance than the CCDFs models. Similar results are obtained for the same range cells and VV polarization mode, as shown in Figures 3.8 and 3.9. Also in this case, the proposed CCDFs produce the best performance.

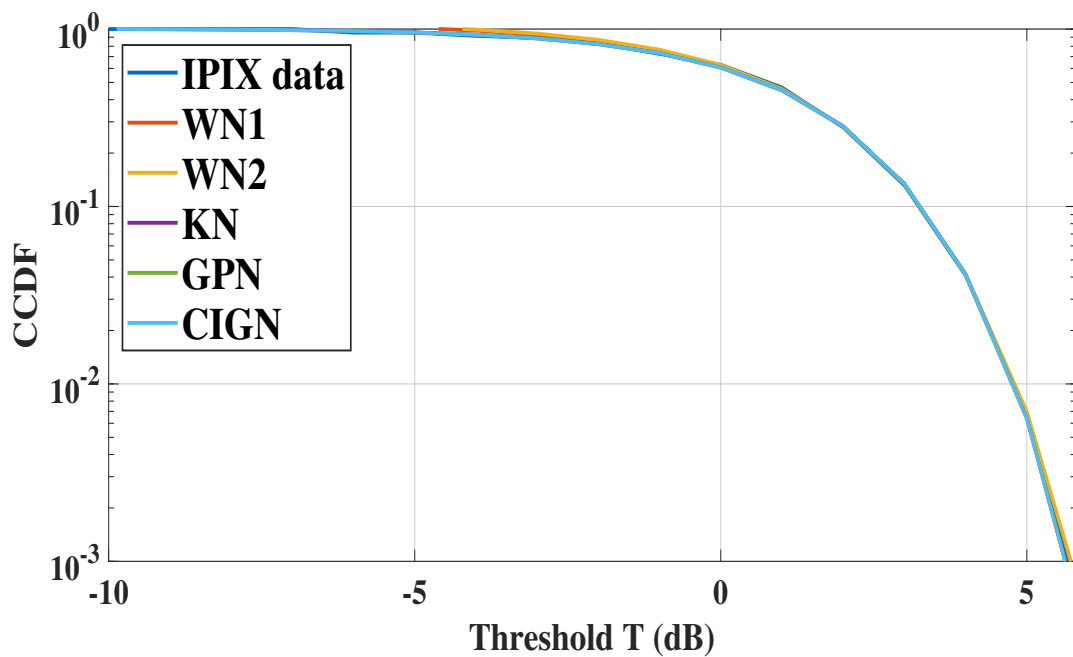


Figure 3.6 – CCDF curves, 60m, HH polarization, 4th range cell, Azimuth resolution = 0.3571° .

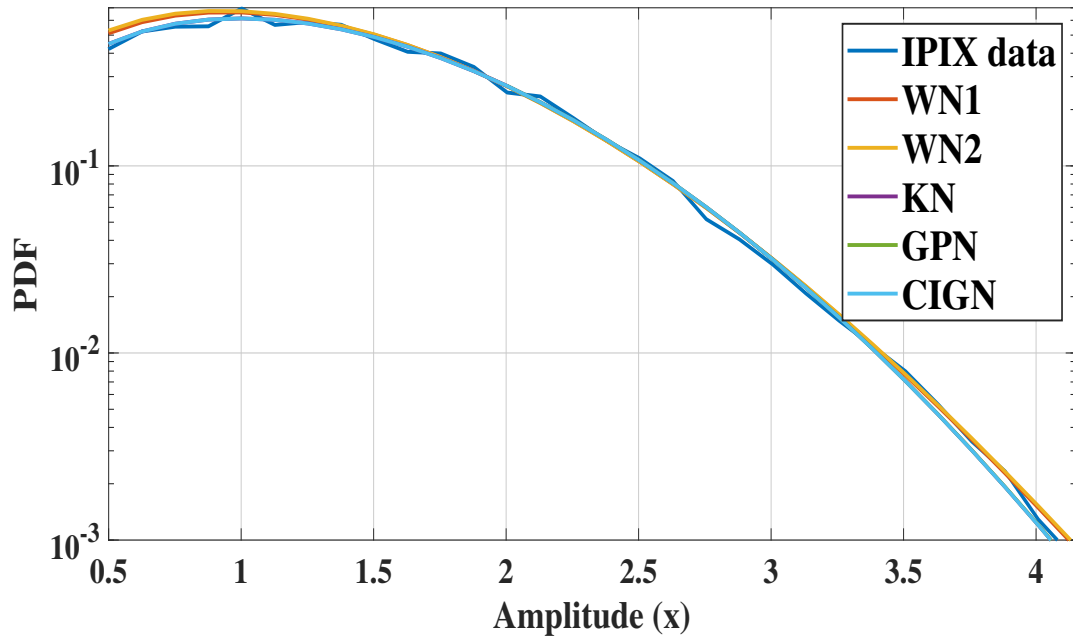


Figure 3.7 – PDF curves, 60m, HH polarization, 4th range cell, Azimuth resolution = 0.3571° .

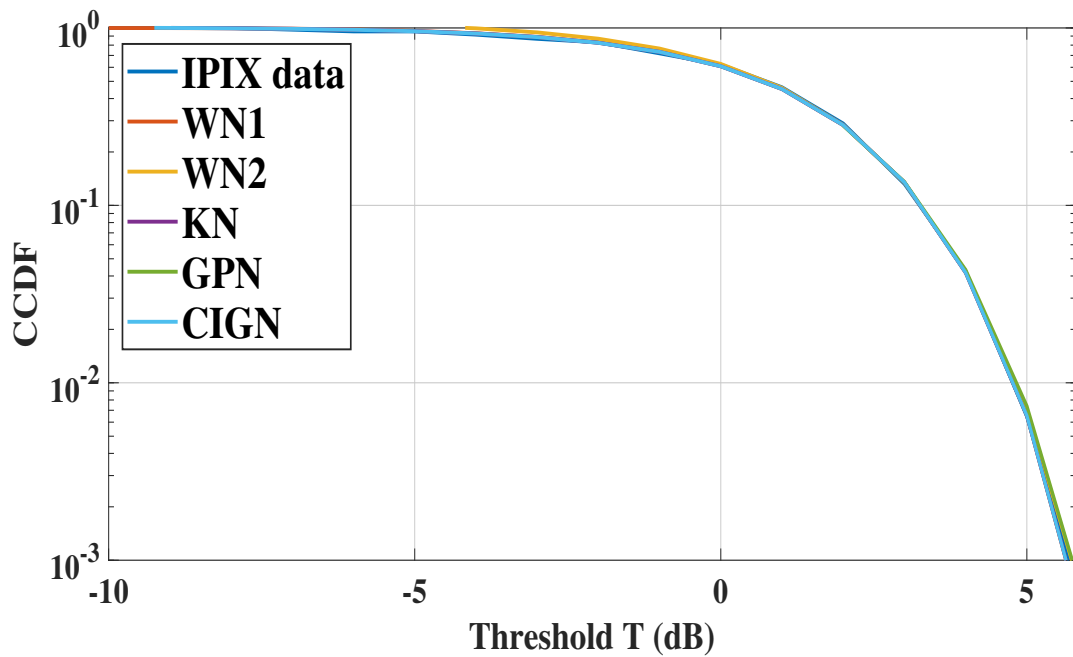


Figure 3.8 – CCDF curves, 60m, VV polarization, 4th range cell, Azimuth resolution = 0.3571° .

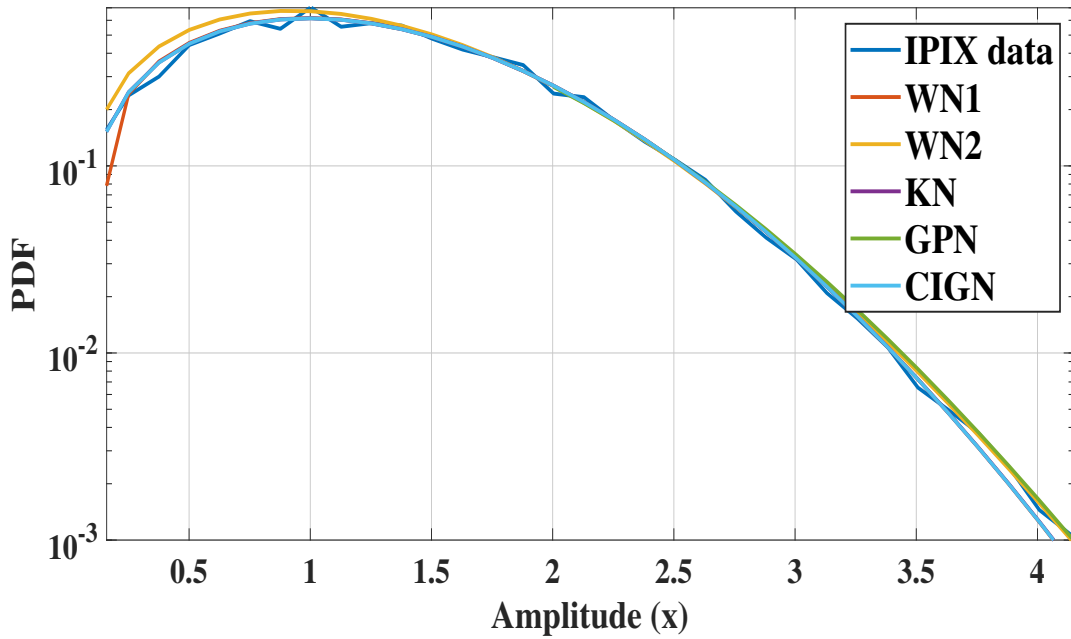


Figure 3.9 – PDF curves, 60m, VV polarization, 4th range cell, Azimuth resolution = 0.3571° .

We repeat the fitting performance of the proposed models by increasing the radar resolution to 30m. There are 163 files of 30m resolution in the IPIX Grimsby database, which offer us a large number of analyzes. One of them is the (19980204_194537_ANTSTEP) file, 20th range cells, HH polarization mode and azimuth resolution set to 16.1499° . We observe in Figure 3.10 that all models exhibit a good fit in the body and in the tail region of real IPIX data, where the WN2 model produce the best results with the smallest MSE values, (Table 3.4). In this case, all PDF models show deviations from the real data, (Figure 3.11). To avoid the similarity of results when conducting tests in the same range cells for the VV data, we chose the 6th range cells. We observe in Figure 3.12 that the CG CCDFs exhibit very long tails, where the GPN and KN models produce the worst results. Globally, the proposed CCDFs of the WN1 and WN2 models are much closer to the IPIX sea data and provide the best approximation in the tail region with the smallest MSE values, (Table 3.4). Also, in this case, all PDF models exhibit very long tails, (Figure 3.13).

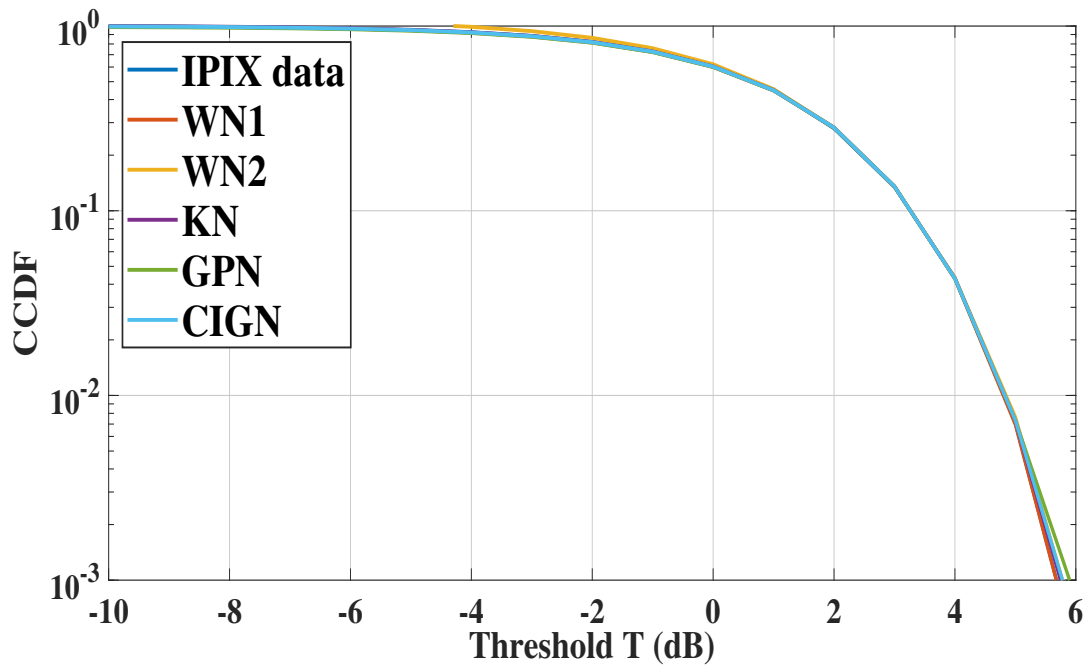


Figure 3.10 – CCDF curves, 30m, HH polarization, 20th range cell, Azimuth resolution = 16.1499°.

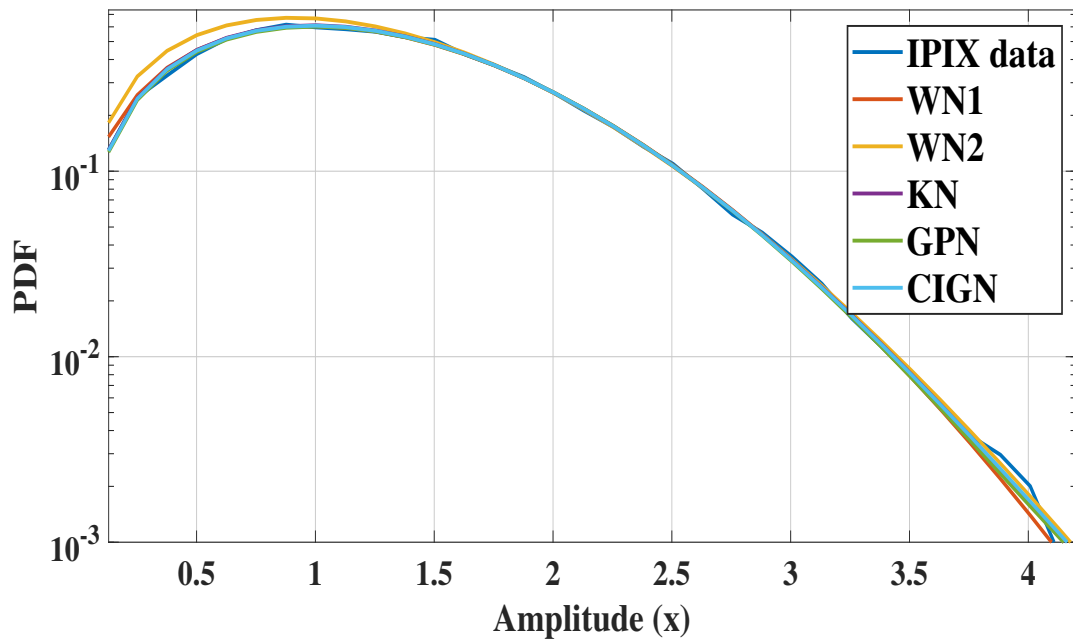


Figure 3.11 – PDF curves, 30m, HH polarization, 20th range cell, Azimuth resolution = 16.1499°.

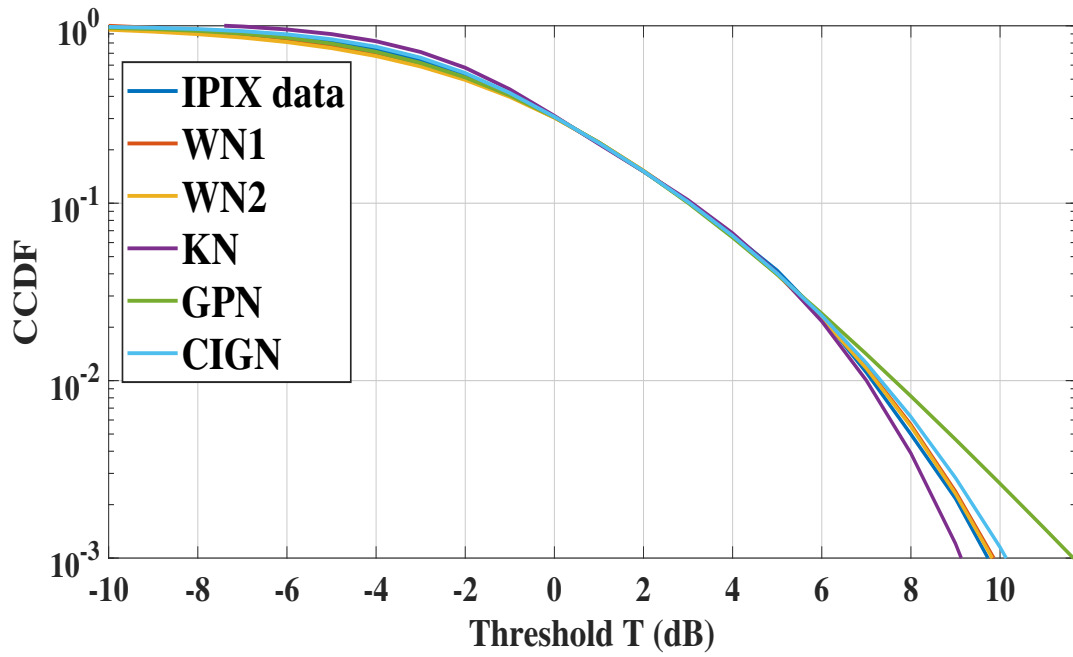


Figure 3.12 – CCDF curves, 30m, VV polarization, 6th range cell, Azimuth resolution = 16.1499° .

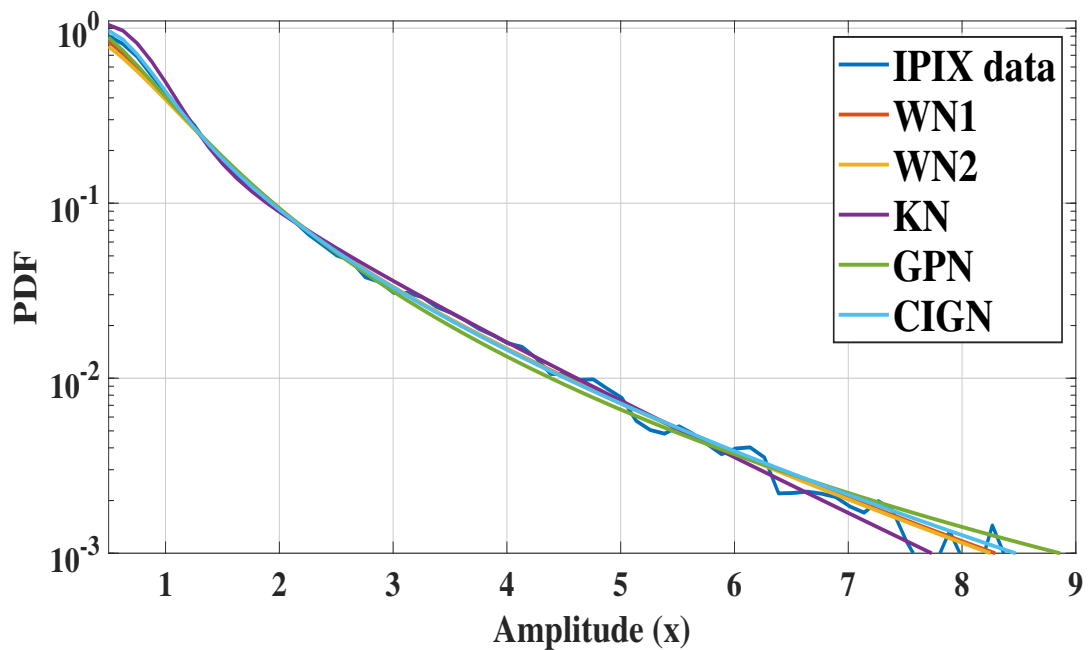


Figure 3.13 – PDF curves, 30m, VV polarization, 6th range cell, Azimuth resolution = 16.1499° .

Models	Parameters and Metrics	60m HH 4 th	60m VV 4 th	30m HH 20 th	30m VV 6 th
WN1	\hat{c}	0.9779	1.9896	1.9778	0.6568
	$\hat{\beta}$	0.2587	1.3984	1.4061	0.5053
	$\hat{\sigma}$	1.1505	0.0427	$2.6157e^{-04}$	0.2767
	Log(MSE)	-5.8092	-5.5088	-6.2696	-6.1233
	Log(CS)	-3.5350	-4.1158	-4.2617	-4.2608
WN2	\hat{c}	0.9687	0.9642	0.9506	0.6576
	$\hat{\beta}$	0.2500	0.2408	0.2354	0.5026
	$\hat{\sigma}$	0.9303	0.9316	0.9281	0.3823
	Log(MSE)	-5.8110	-5.7189	-6.7320	-6.0238
	Log(CS)	-3.5195	-3.9442	-4.1175	-4.1556
KN	\hat{v}	1.3220	38.1319	0.8461	0.1728
	\hat{b}	0.3190	9.6991	2.1853	0.3787
	$\hat{\sigma}$	0.9893	0.8558	0.9390	0.4384
	Log(MSE)	-5.5857	-5.5092	-6.4879	-5.0042
	Log(CS)	-3.6136	-4.1155	-4.2283	-3.5782
GPN	$\hat{\alpha}$	1.4773	84.6081	2.0707	2.7044
	\hat{b}	0.2603	77.8829	0.1045	1.6812
	$\hat{\sigma}$	0.9355	0.6614	0.9918	$1.8155e^{-09}$
	Log(MSE)	-5.5880	-5.3439	-6.3646	-4.0127
	Log(CS)	-3.6124	-3.9343	-4.2425	-4.1363
CIGN	$\hat{\lambda}$	1.0011	4.1937	0.5579	0.7567
	$\hat{\mu}$	0.3955	0.3007	0.2745	0.8421
	$\hat{\sigma}$	0.9364	0.9636	0.9619	0.3267
	Log(MSE)	-5.6047	-5.5052	-6.4566	-5.9862
	Log(CS)	-3.6130	-4.1181	-4.2309	-4.2072

Table 3.4 – The estimated parameters for each model for range resolutions 60 and 30m, using PCFE method.

For range resolution of 15m where the echoes are a bit spiky, the first performance was conducted for the 18th range cells of (19980204_221700_ANTSTEP) file, azimuth resolution is 0.2966° and HH polarization mode. The WN1 and WN2 CCDFs consistently give a good fit in the body and in the tail region of IPIX data. On the contrary, the CIGN and GPN models show a deviation in the tail region, as shown in Figure 3.14, and offer the worst MSE metrics, (Table 3.5). For PDF curves, CG models show the worst fit (Figure 3.15). The second test was performed for the 2nd range cells, and VV data. Excellent performance is produced by all the models, according to the MES metrics, the proposed CCDFs show the best approximation to the IPIX data, (Figure 3.16). In this case, the CIGN PDF produces the worst performance in the tail region, (Figure 3.17).

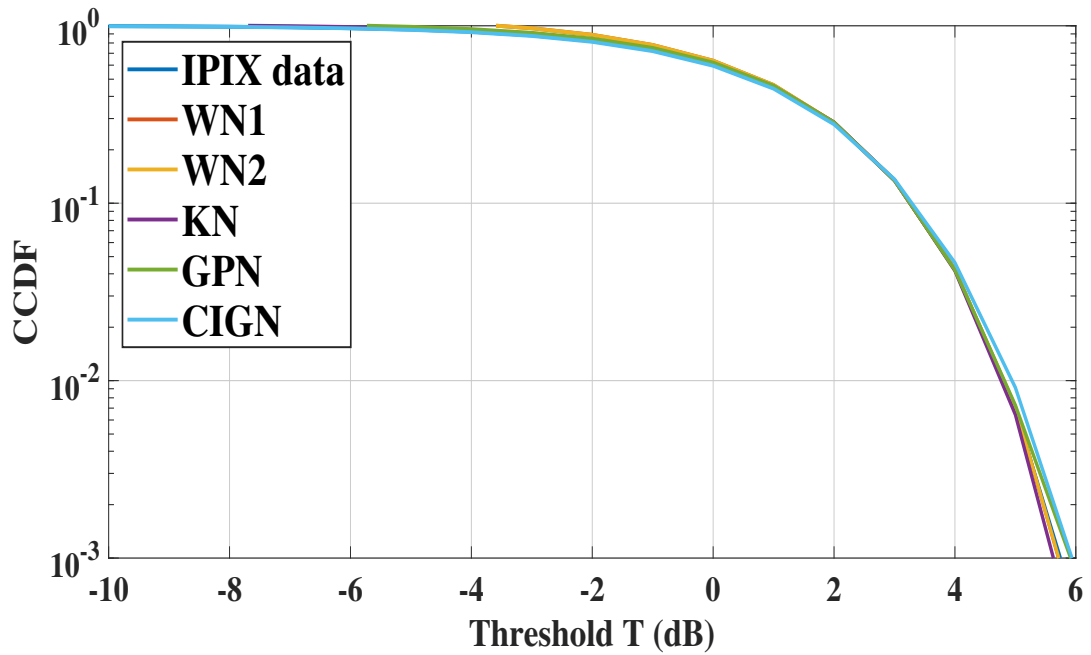


Figure 3.14 – CCDF curves, 15m, HH polarization, 18th range cell, Azimuth resolution = 0.2966° .

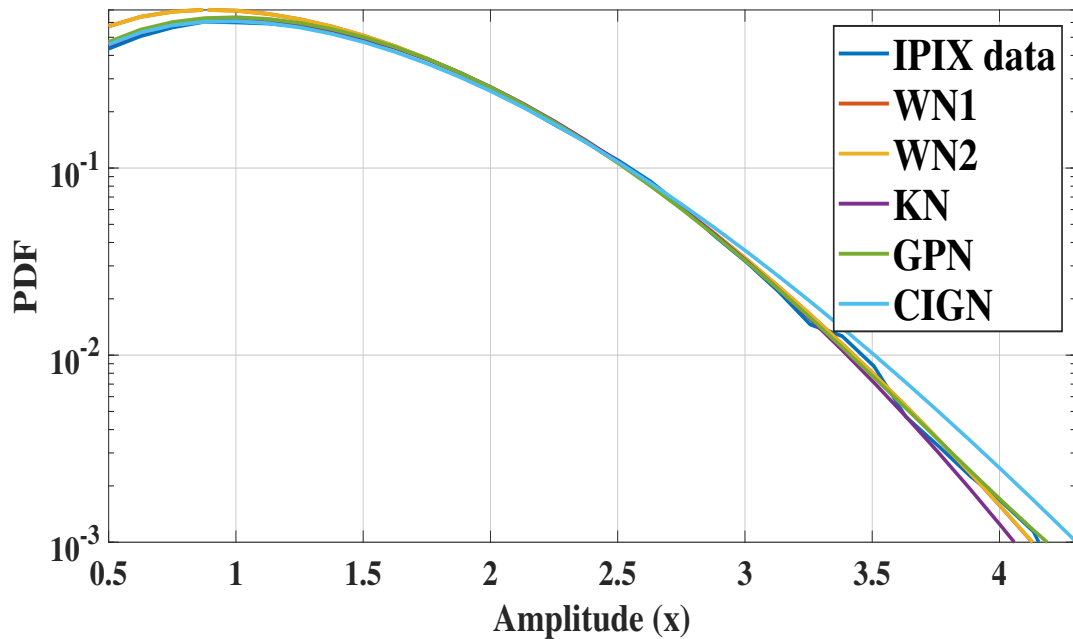


Figure 3.15 – PDF curves, 15m, HH polarization, 18th range cell, Azimuth resolution = 0.2966° .

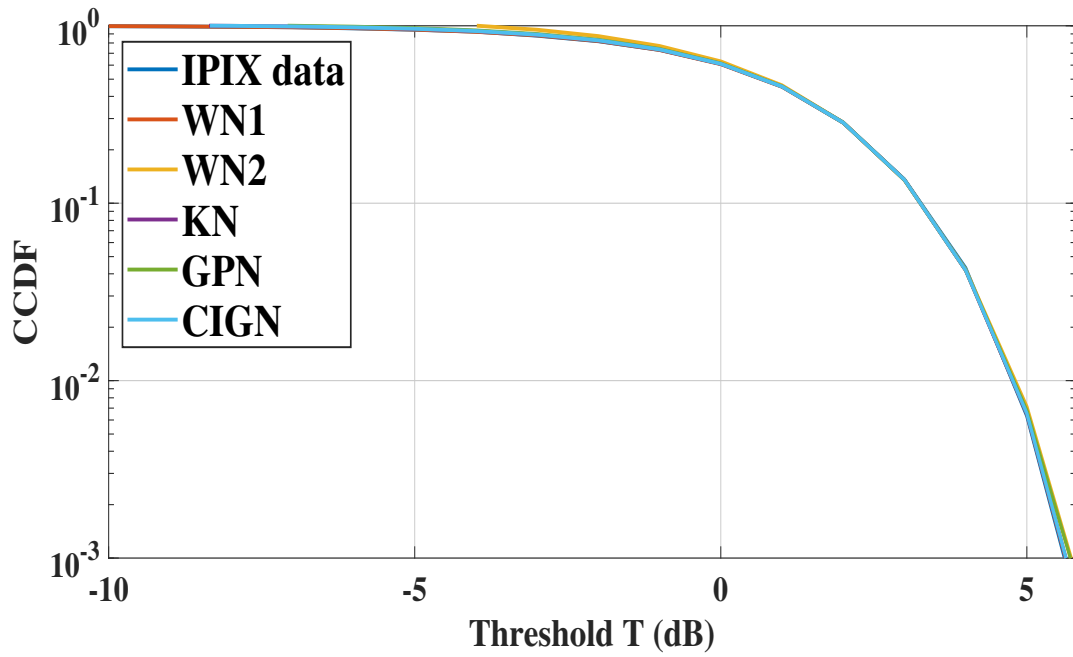


Figure 3.16 – CCDF curves, 15m, VV polarization, 2nd range cell, Azimuth resolution = 0.2966° .

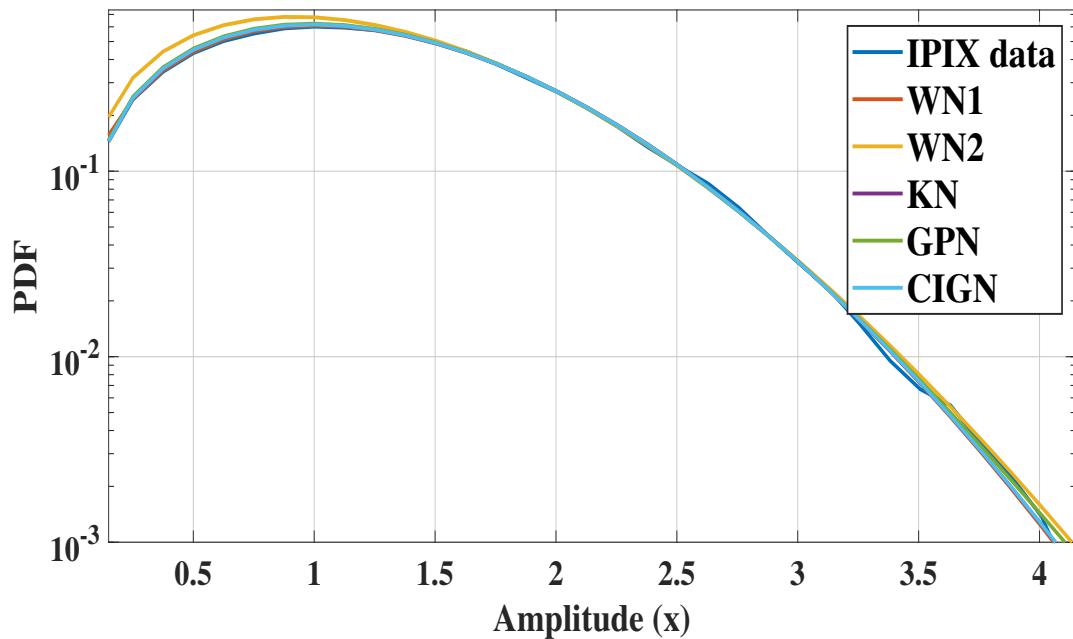


Figure 3.17 – PDF curves, 15m, VV polarization, 2nd range cell, Azimuth resolution = 0.2966° .

Models	Parameters and Metrics	15m HH 18 th	15m VV 2 nd	15m VH 3 rd
WN1	\hat{c}	0.9439	2.0098	0.7087
	$\hat{\beta}$	0.1483	1.4141	0.6015
	$\hat{\sigma}$	0.8942	$2.3231e^{-05}$	0.2025
	Log(MSE)	-7.0123	-6.1913	-6.8314
	Log(CS)	-3.9738	-4.1830	-4.3272
WN2	\hat{c}	0.9446	0.9598	0.7040
	$\hat{\beta}$	0.1603	0.2183	0.5935
	$\hat{\sigma}$	0.9324	0.9343	0.3267
	Log(MSE)	-7.0139	-6.0196	-6.9113
	Log(CS)	-3.9697	-4.0016	-4.3470
KN	\hat{v}	3.55790	19.2946	0.1973
	\hat{b}	10.2566	9.9768	0.3941
	$\hat{\sigma}$	0.97390	0.9315	0.3865
	Log(MSE)	-6.1494	-6.1569	-5.5771
	Log(CS)	-4.2924	-4.1586	-3.9966
GPN	$\hat{\alpha}$	2.3983	5.1031	2.4939
	\hat{b}	0.5785	1.0417	1.4959
	$\hat{\sigma}$	0.9590	0.9661	$5.9237e^{-07}$
	Log(MSE)	-6.5598	-6.1325	-4.9644
	Log(CS)	-3.8982	-4.0829	-3.6083
CIGN	$\hat{\lambda}$	0.9768	4.4852	0.9654
	$\hat{\mu}$	1.2454	0.2881	0.9068
	$\hat{\sigma}$	$2.3924e^{-07}$	0.9666	0.1727
	Log(MSE)	-5.1047	-6.1619	-6.6351
	Log(CS)	-3.8611	-4.1583	-4.5874

Table 3.5 – The estimated parameters for each model for range resolution 15m, using PCFE method.

The last test was carried out for the 3rd range cells with cross-polarized VH data. We observe in Figure 3.18 that the CG CCDFs exhibit a large deviation in the tail region, where the GPN and KN models produce the worst results. In general, the proposed WN1 and WN2 models show an excellent fit to the tail region of IPIX data with the smallest MSE values. Also, in this case, all PDF models show a less precise fit than CCDF models, (Figure 3.19). Based on the obtained results from the three resolutions, the PDF models show long tails and fail to provide a precise fit, where the proposed CCDFs WN1 and WN2 provide the best fit compared to the KN, GPN and CIGN models, especially in the tail region.

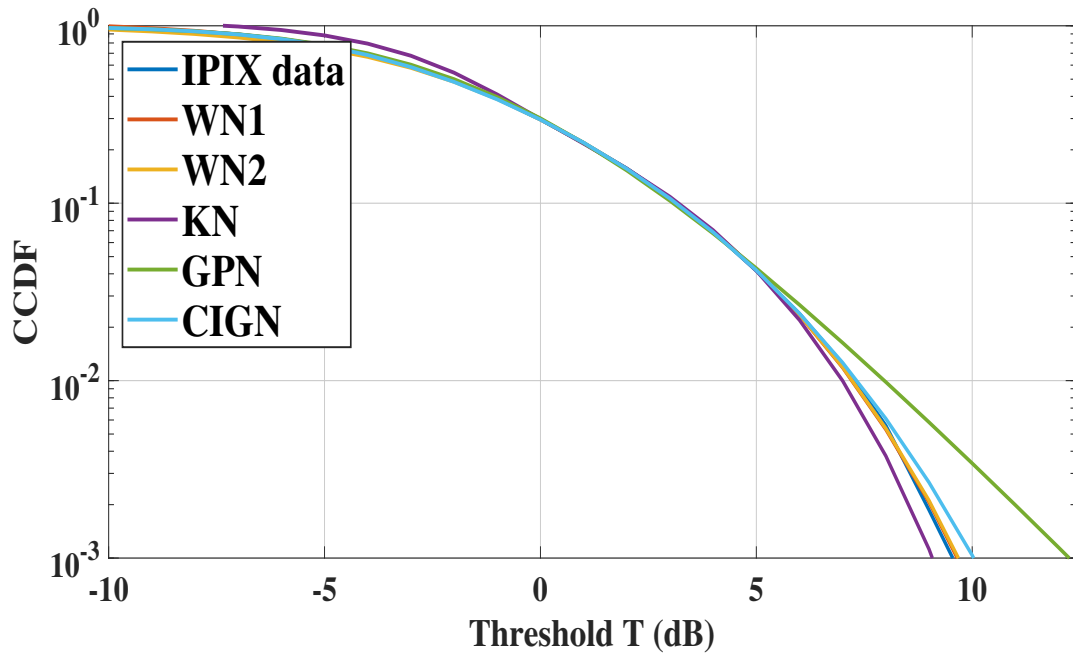


Figure 3.18 – CCDF curves, 15m, VH polarization, 3rd range cell, Azimuth resolution = 0.2966° .

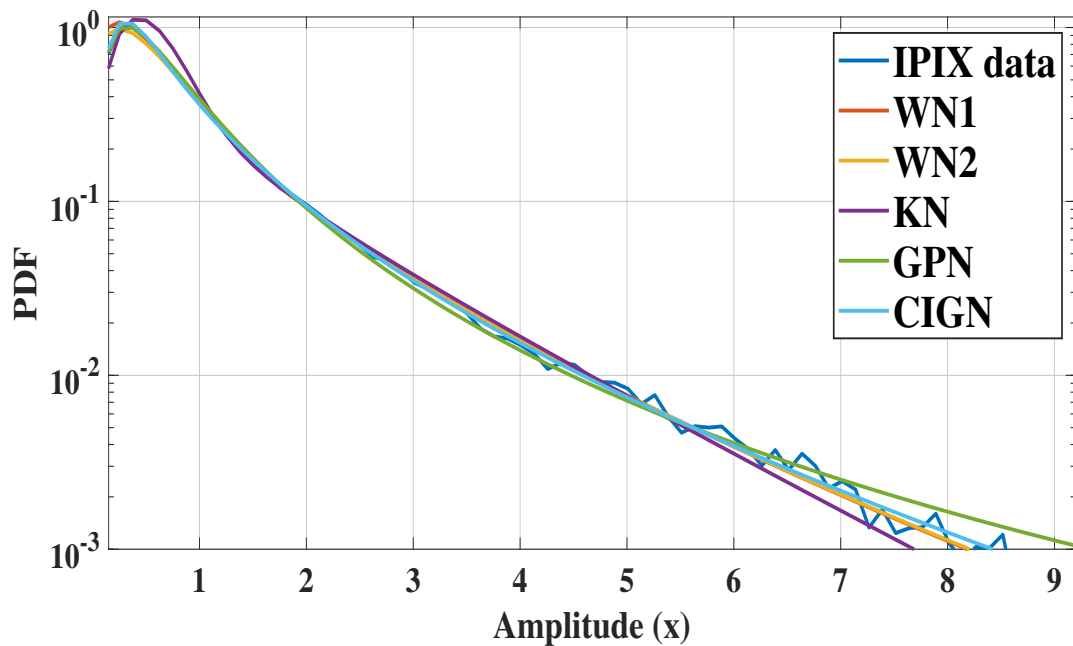


Figure 3.19 – PDF curves, 15m, VH polarization, 3rd range cell, Azimuth resolution = 0.2966° .

3.6.3.2 Range Resolutions 9 and 3m

We examine the fitting performance of the proposed models when the radar operates at a high-resolution of 9 and 3m, where the sea clutter becomes spikier and intensive. When examining the 9m resolution (19980204_221908_ANTSTEP) file, we found that many cells of like and cross-polarization data show accurate CCDF tails. One of these cells is 24th with HH data, and azimuth resolution equal to 0.3241° , the CIGN model shows the longer tail and the worst fitting performance. In this case, the best results are obtained by the proposed models WN1 and WN2, as shown in Figure 3.20. For the same range cells and VV data, we observe in Figure 3.22 that all models yield a good-fit to the IPIX data. According to MSE metrics, WN1 model shows the best fit performance, followed by WN2 and CIGN models, (Table 3.6). In addition, at this resolution with the HV and VH cross-polarization data, the proposed CCDFs provide precise tail regions, as shown in in Figures 3.24 and 3.26, only, CIGN CCDF presents a deviation from the HV data. Depending on the MSE metrics, (Table 3.6), WN1 and WN2 models provide a better approximation of IPIX data.

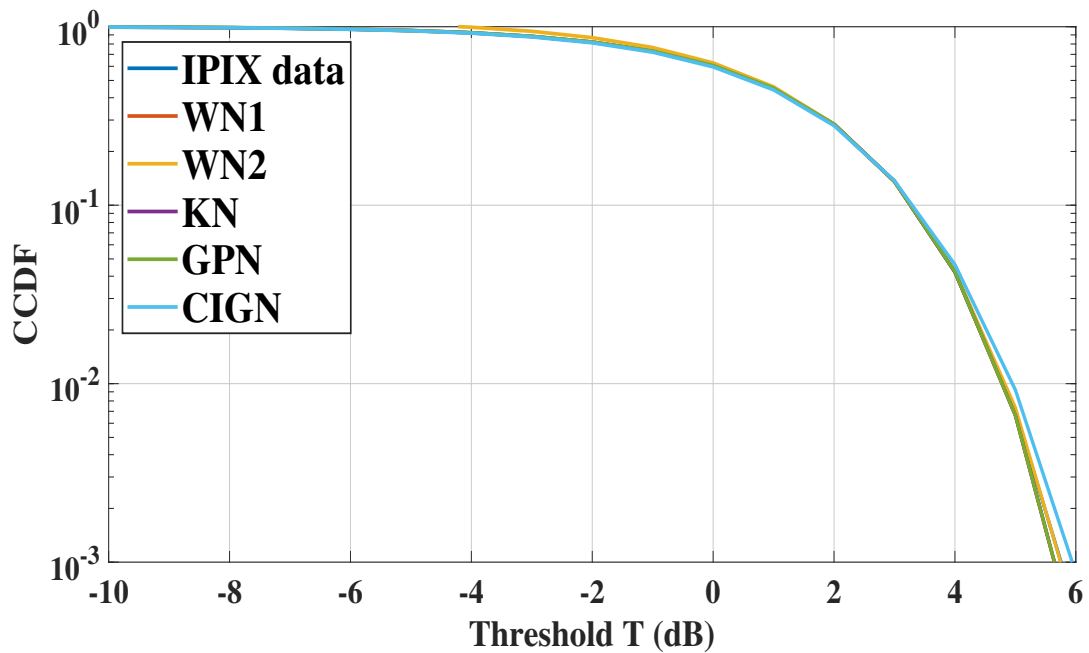


Figure 3.20 – CCDF curves, 9m, HH polarization, 24th range cell, Azimuth resolution = 0.3241° .

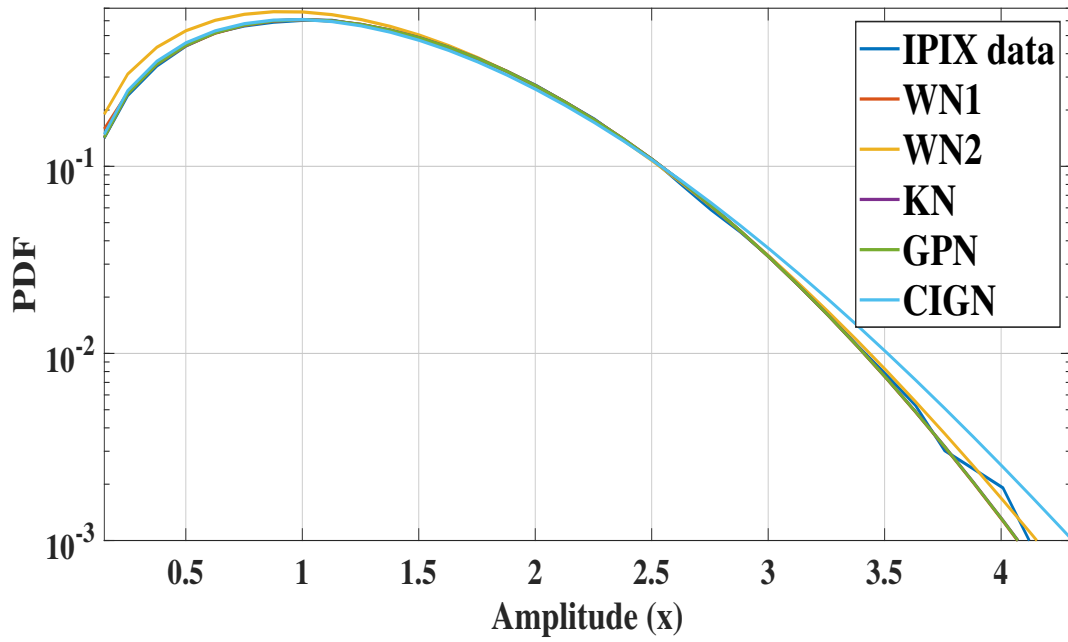


Figure 3.21 – PDF curves, 9m, HH polarization, 24th range cell, Azimuth resolution = 0.3241° .

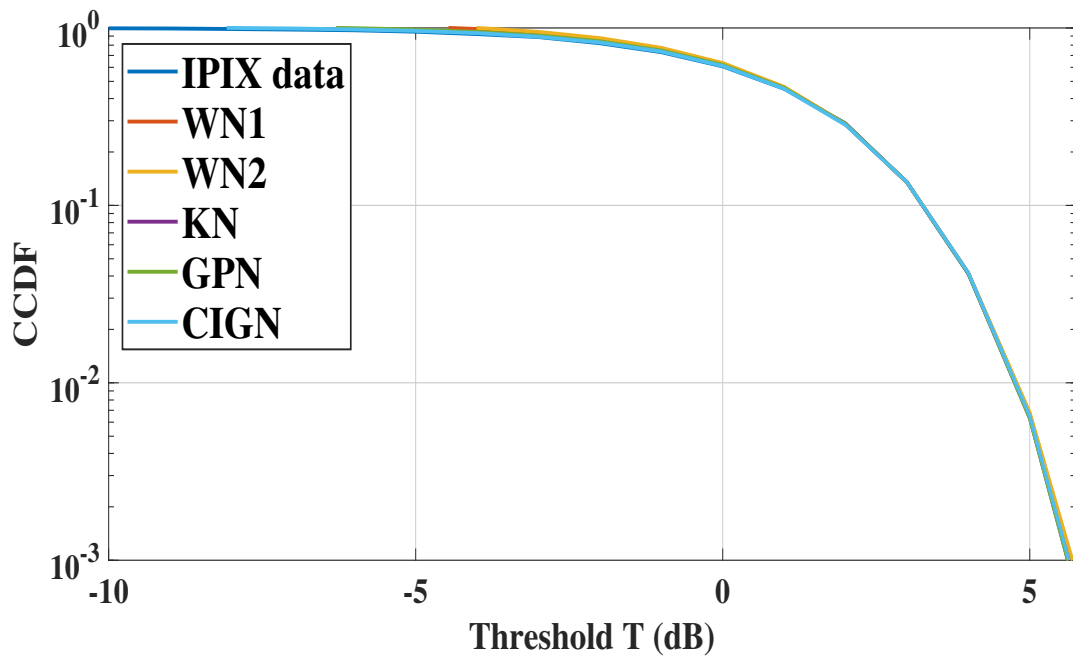


Figure 3.22 – CCDF curves, 9m, VV polarization, 24th range cell, Azimuth resolution = 0.3241° .

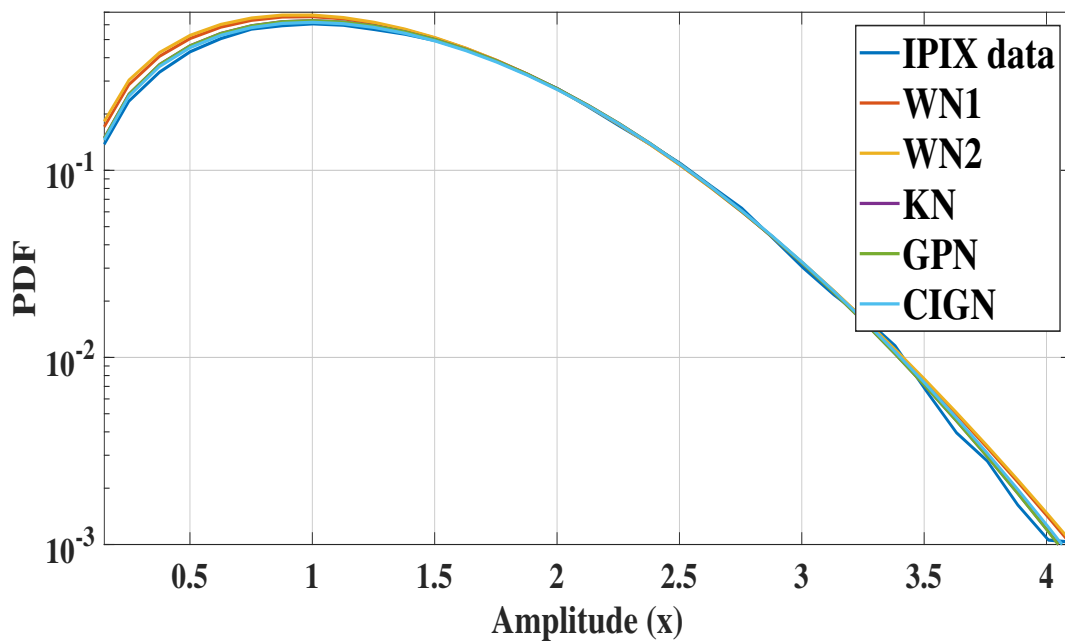


Figure 3.23 – PDF curves, 9m, VV polarization, 24th range cell, Azimuth resolution = 0.3241° .

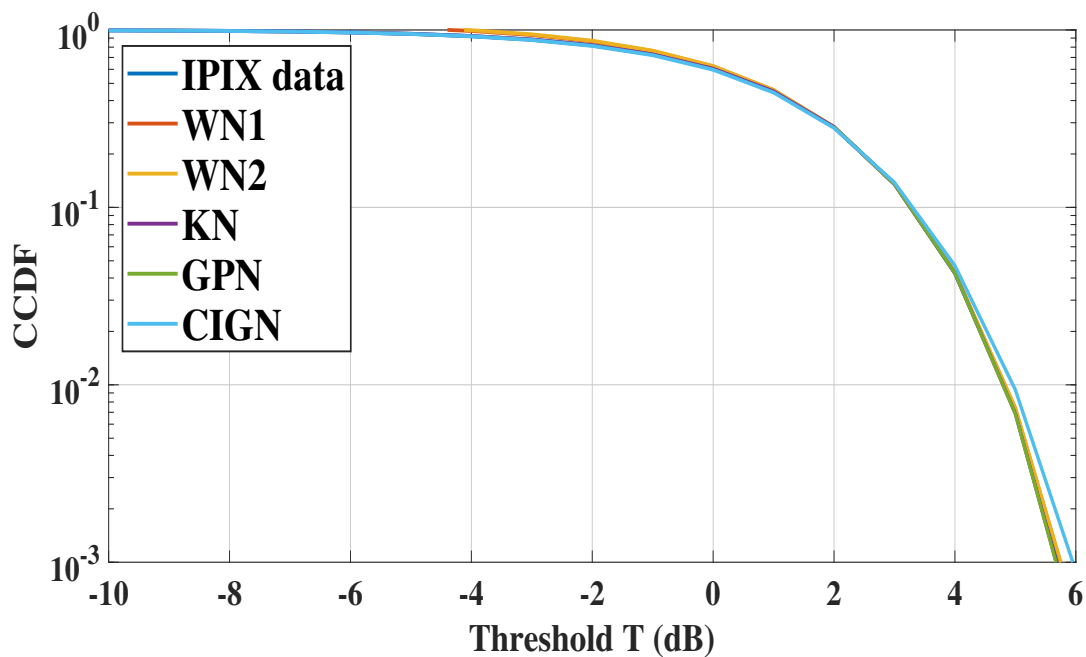


Figure 3.24 – CCDF curves, 9m, HV polarization, 2nd range cell, Azimuth resolution = 0.3241° .

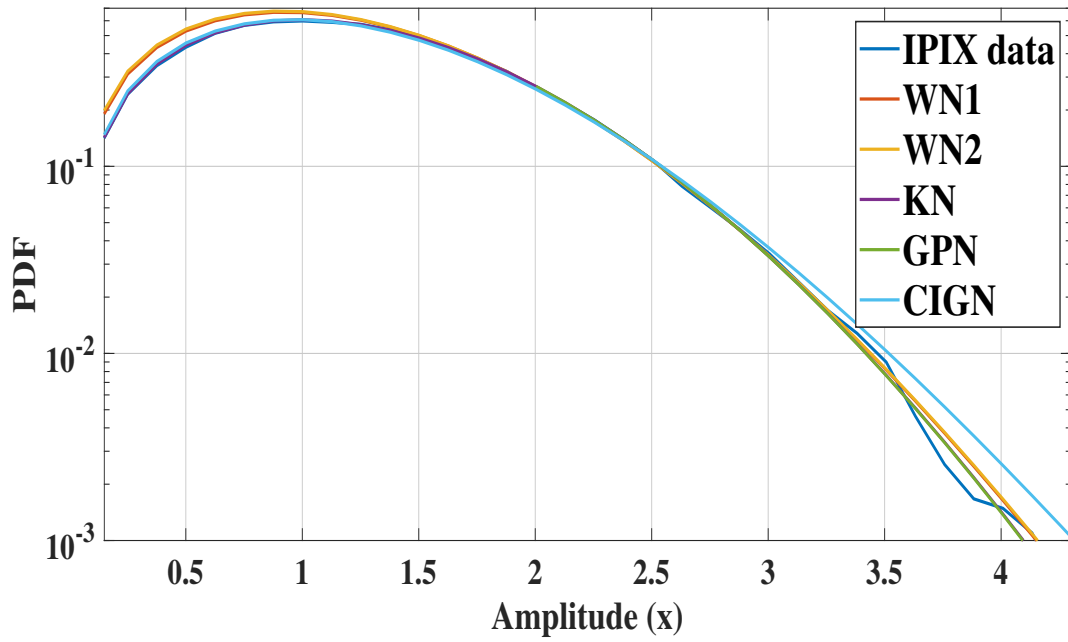


Figure 3.25 – PDF curves, 9m, HV polarization, 2nd range cell, Azimuth resolution = 0.3241° .

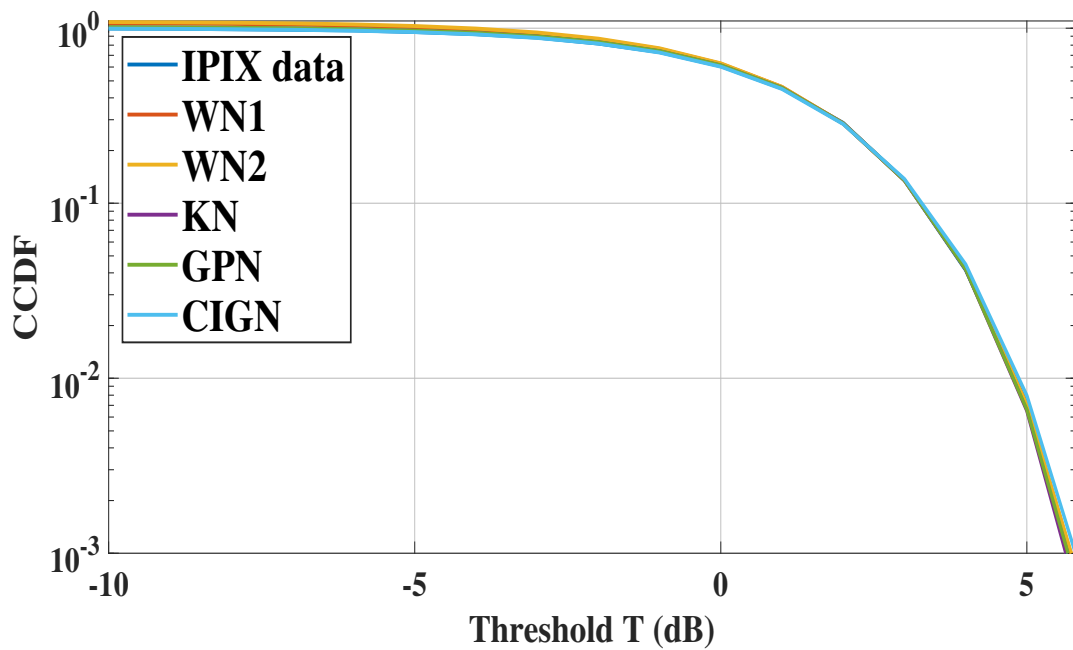


Figure 3.26 – CCDF curves, 9m, VH polarization, 28th range cell, Azimuth resolution = 0.3241° .

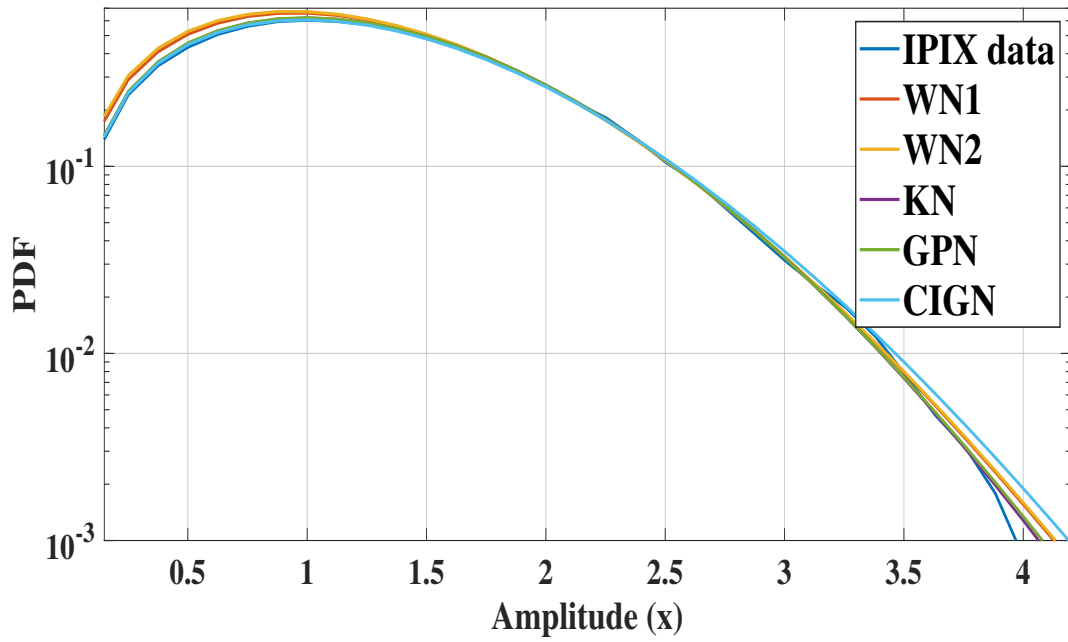


Figure 3.27 – PDF curves, 9m, VH polarization, 28th range cell, Azimuth resolution = 0.3241° .

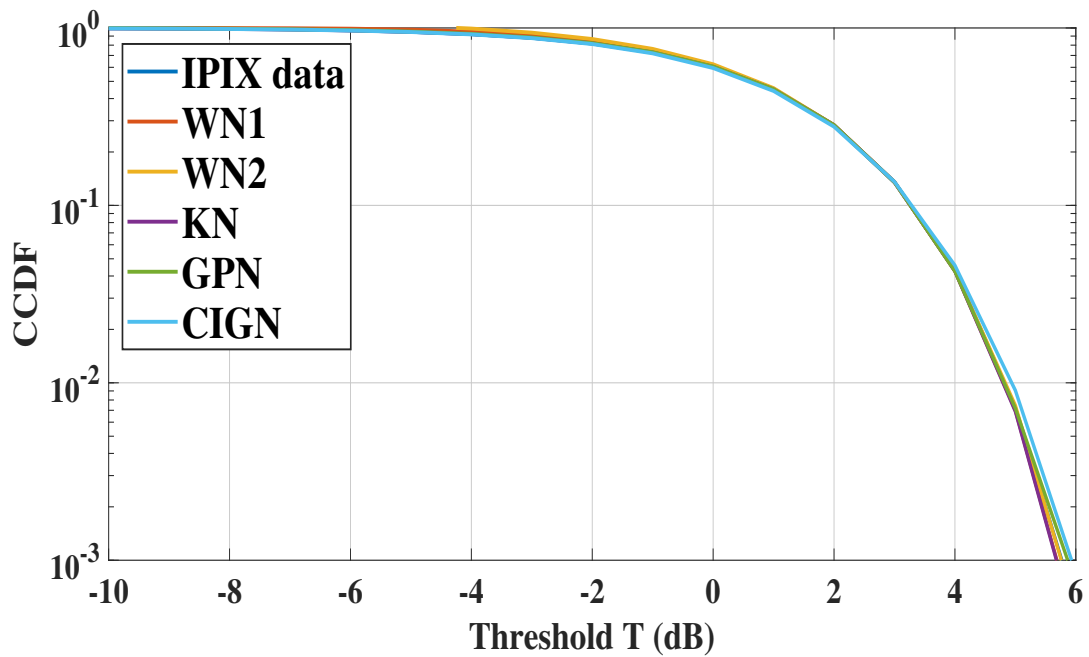


Figure 3.28 – CCDF curves, 3m, HH polarization, 3rd range cell, Azimuth resolution = 44.8956° .

Models	Parameters and Metrics	9m HH 24 th	9m VV 24 th	9m HV 2 nd	9m VH 28 th
WN1	\hat{c}	2.0027	0.6059	0.9604	0.9791
	$\hat{\beta}$	1.4135	0.3820	0.2289	0.2561
	$\hat{\sigma}$	$6.5939e^{-09}$	$2.8574e^{-04}$	0.9524	0.8969
	Log(MSE)	-6.9721	-6.7910	-6.8650	-6.6436
	Log(CS)	-6.8801	-6.5715	-6.5588	-6.4128
WN2	\hat{c}	0.9636	0.9746	0.9543	0.9697
	$\hat{\beta}$	0.2457	0.2397	0.2239	0.2473
	$\hat{\sigma}$	0.9325	0.9368	0.9319	0.9342
	Log(MSE)	-6.9134	-6.7149	-6.7972	-6.6001
	Log(CS)	-6.8801	-6.5715	-6.5588	-6.4128
KN	\hat{v}	1.2047	0.1292	2.1030	1.6363
	\hat{b}	14.1249	1.8163	3.6864	0.4521
	$\hat{\sigma}$	0.91180	0.9903	0.9480	0.8977
	Log(MSE)	-6.8928	-6.5780	-6.5300	-6.3445
	Log(CS)	-6.8801	-6.5715	-6.5588	-6.4128
GPN	$\hat{\alpha}$	1.0091	1.6695	3.3425	4.2457
	\hat{b}	11.9145	7.4684	0.4830	0.5580
	$\hat{\sigma}$	0.9832	0.8458	0.9737	0.9800
	Log(MSE)	-6.8801	-6.5715	-6.5588	-6.4128
	Log(CS)	-6.8801	-6.5715	-6.5588	-6.4128
CIGN	$\hat{\lambda}$	0.9776	1.0717	1.0344	1.6179
	$\hat{\mu}$	1.2468	0.6178	1.0179	1.0574
	$\hat{\sigma}$	$2.7948e^{-06}$	0.8614	$2.2214e^{-04}$	0.5333
	Log(MSE)	-5.0659	-6.6257	-4.9413	-5.2086
	Log(CS)	-6.8801	-6.5715	-6.5588	-6.4128

Table 3.6 – The estimated parameters for each model for range resolution 9m, using PCFE method.

Finally, to verify if the proposed CCDFs are suitable for high-resolution 3m sea clutter data, we applied eight tests on three files (19980205_185111_ANTSTEP), (19980223_190901_ANTSTEP) and (19980204_222110_ANTSTEP), where the azimuth resolution is 44.8956° , 329.87° and 0.3131° , respectively. The estimated parameters for each test are illustrated in Tables 3.7 and 3.8. For the first file, the analysis was carried out on the 3rd range cells and HH data. The proposed CCDFs show the best fitting results, whereas the WN2 model provides the accurate tail followed by WN1. In contrast, the CG CCDFs are slightly spaced and the CIGN model exhibits the worst performance, (Figure 3.28). Also, for the VV data and the 17th range cells, the proposed models provide the best fit against the CG models, (Figure 3.29).

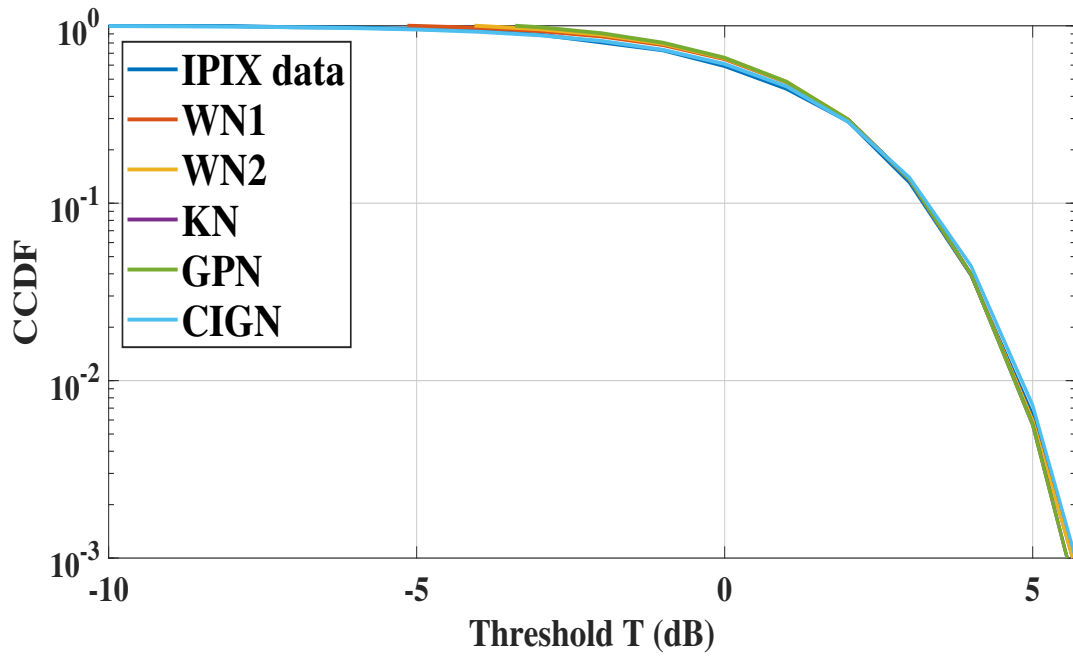


Figure 3.29 – CCDF curves, 3m, VV polarization, 17th range cell, Azimuth resolution = 44.8956° .

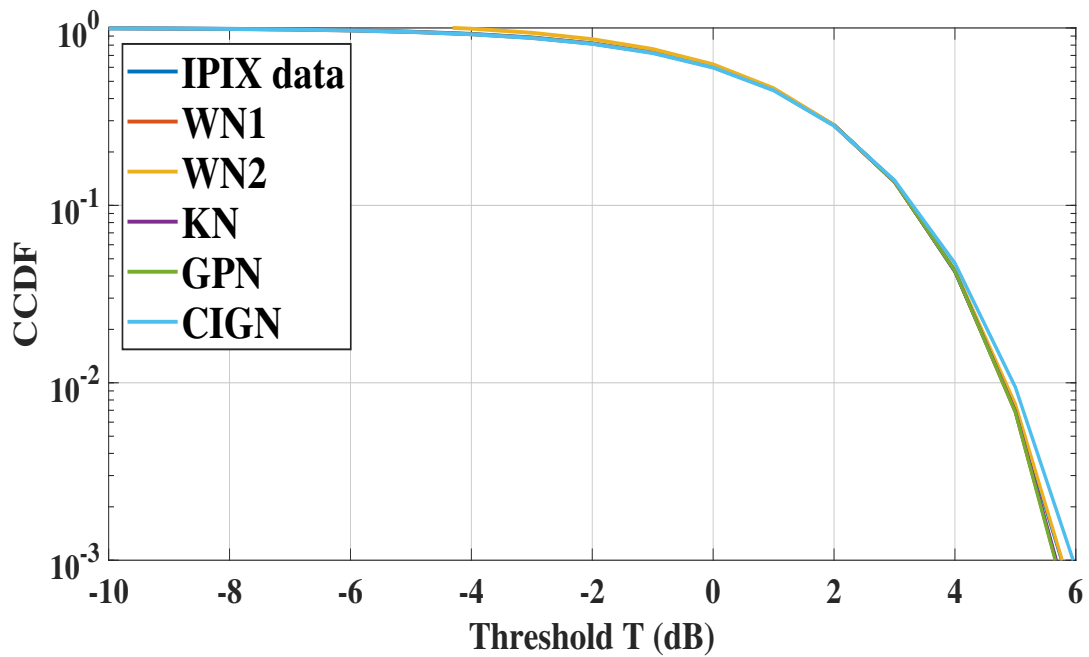


Figure 3.30 – CCDF curves, 3m, HV polarization, 12th range cell, Azimuth resolution = 44.8956° .

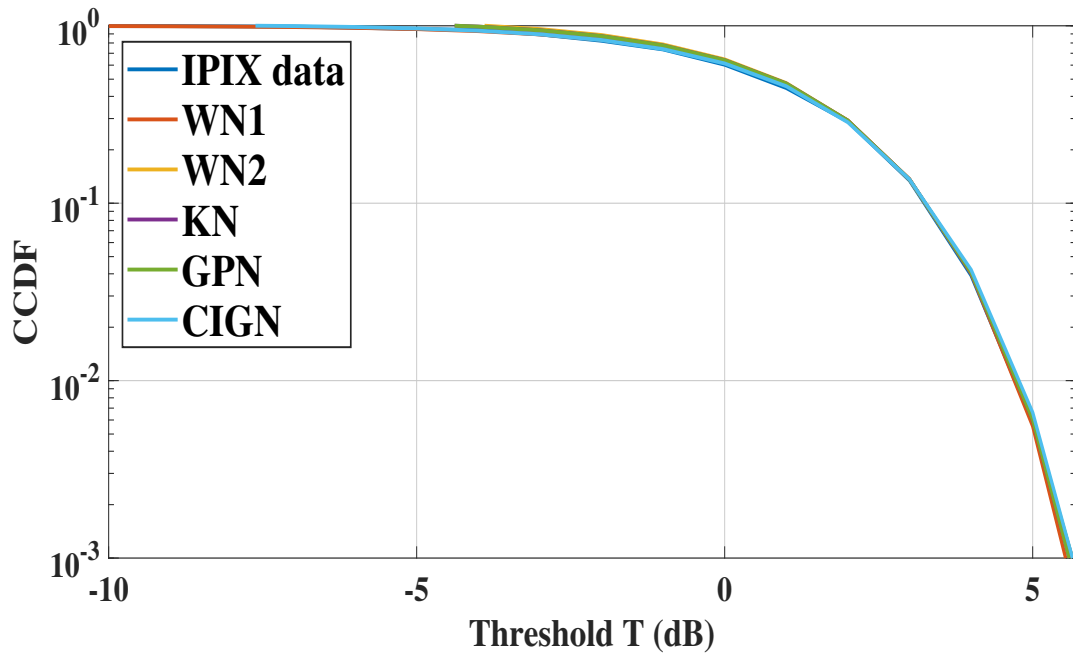


Figure 3.31 – CCDF curves, 3m, VH polarization, 23rd range cell, Azimuth resolution = 44.8956° .

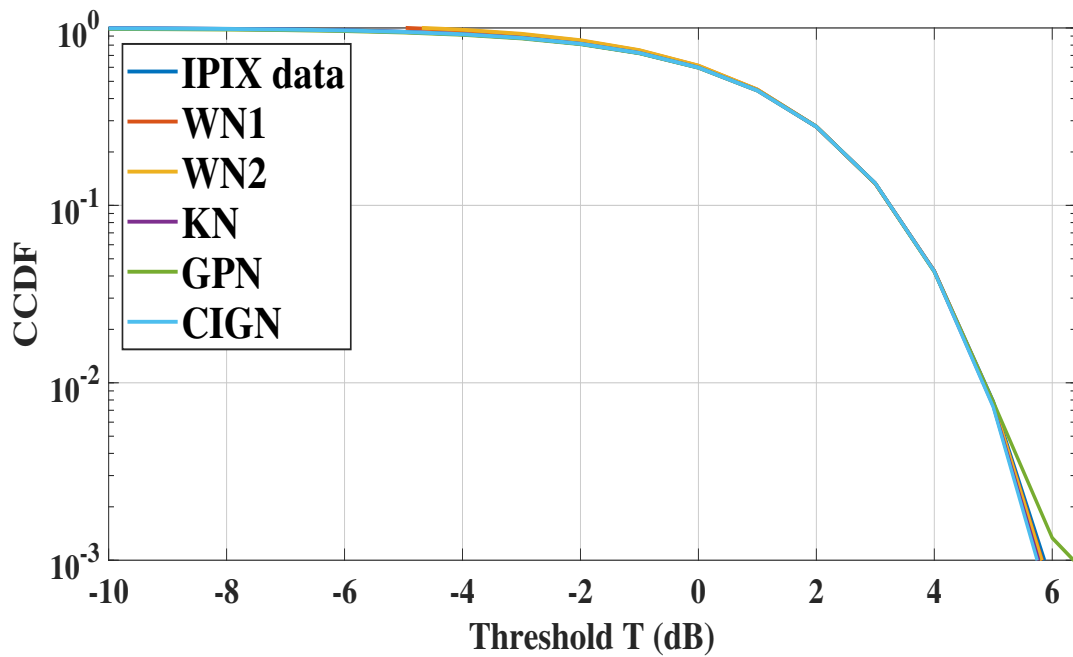


Figure 3.32 – CCDF curves, 3m, HH polarization, 2nd range cell, Azimuth resolution = 329.87° .

Models	Parameters and Metrics	3m HH 3 rd	3m VV 17 th	3m HV 12 th	3m VH 23 rd
WN1	\hat{c}	1.9380	1.0689	1.9879	2.0839
	$\hat{\beta}$	1.3674	0.3785	1.4099	1.4341
	$\hat{\sigma}$	0.1351	0.8894	$1.6106e^{-07}$	$7.3102e^{-04}$
	Log(MSE)	-6.4910	-5.0335	-6.5843	-5.6797
WN2	\hat{c}	0.9385	1.0452	0.9576	1.0015
	$\hat{\beta}$	$1.0609e^{-06}$	0.3466	0.2468	0.2609
	$\hat{\sigma}$	0.9275	0.9432	0.9299	0.9455
	Log(MSE)	-7.1075	-5.0475	-6.9164	-5.7643
KN	\hat{v}	2.0646	1.1002	3.0856	1.4039
	\hat{b}	3.5411	0.4253	8.3125	0.4049
	$\hat{\sigma}$	0.9443	0.8800	0.7138	0.9819
	Log(MSE)	-6.2868	-5.0099	-6.4392	-5.6767
GPN	$\hat{\alpha}$	3.4124	1.4113	5.9924	1.1130
	\hat{b}	0.4800	2.6806	0.4366	0.3418
	$\hat{\sigma}$	0.9763	0.9673	0.9697	0.9819
	Log(MSE)	-6.4235	-5.0090	-6.5594	-5.6765
CIGN	$\hat{\lambda}$	1.0007	1.2596	3.1503	9.6392
	$\hat{\mu}$	0.3191	0.7418	1.2502	0.1405
	$\hat{\sigma}$	0.9521	0.8102	$3.8958e^{-04}$	0.9774
	Log(MSE)	-5.3598	-4.4974	-4.9707	-5.6764

Table 3.7 – The estimated parameters for each model for range resolution 3m, using PCFE method.

Similar results are obtained for the cross-polarization HV data on the 12th range cells. The WN2 model shows the best performance, where the CIGN CCDF exhibits the worst tail. As for the VH data and 23rd range cells, all the CCDFs show a good fit and the WN2 is the closest to the IPIX data, (Figure 3.30 and 3.31). For the second file, 2nd range cells and HH data, the proposed models show precise tails, where the GPN model shows a deviation in the tail region, (Figure 3.32). The last results do not show any significant differences, the WN1 and WN2 CCDFs exhibit accurate tails and provide the best fit performance over CG models, (Figures 3.32, 3.34 and 3.35). Based on the results obtained from the three azimuth resolutions, we can conclude that the proposed WN1 and WN2 models are suitable for high-resolution IPIX data.

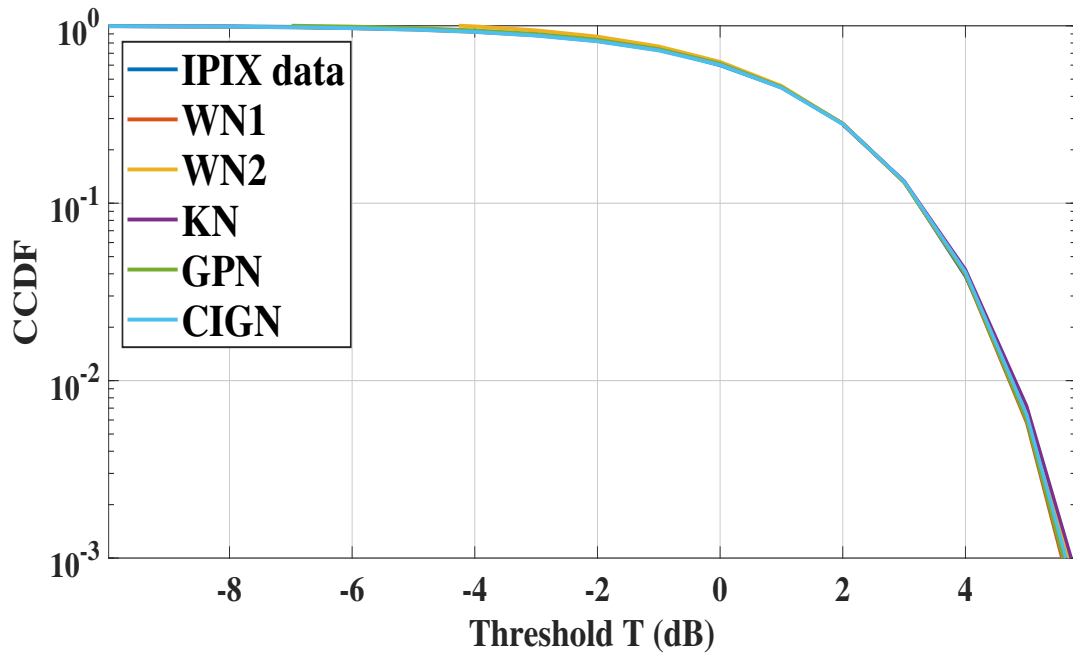


Figure 3.33 – CCDF curves, 3m, VV polarization, 2nd range cell, Azimuth resolution = 329.87° .

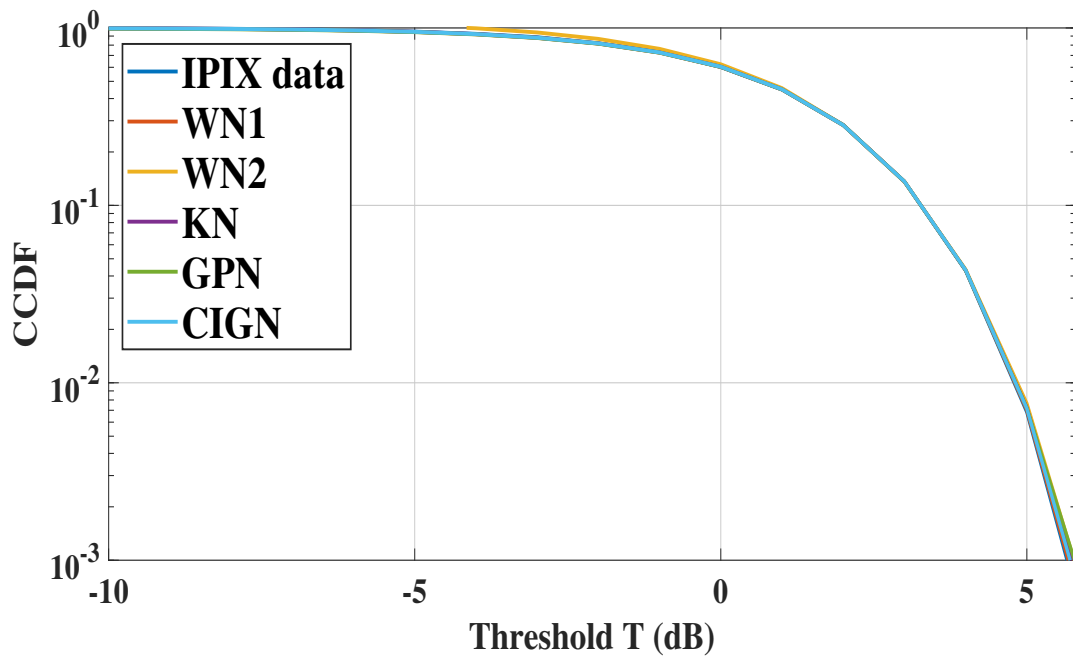


Figure 3.34 – CCDF curves, 3m, HV polarization, 26th range cell, Azimuth resolution = 0.3131° .

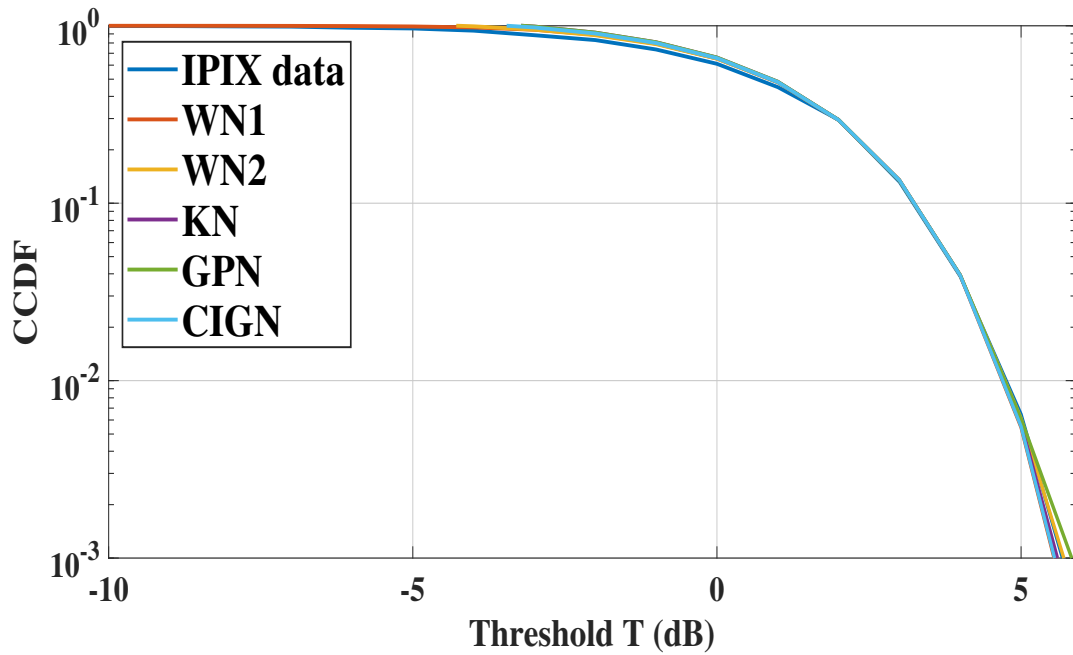


Figure 3.35 – CCDF curves, 3m, VH polarization, 26th range cell, Azimuth resolution = 0.3131°.

Models	Parameters and Metrics	3m HH 2 nd	3m VV 2 nd	3m HV 26 th	3m VH 26 th
WN1	\hat{c}	0.9668	0.9265	1.9846	1.1855
	$\hat{\beta}$	0.3050	1.4080	1.4037	0.3377
	$\hat{\sigma}$	0.9828	$3.8270e^{-05}$	$6.5766e^{-09}$	0.9003
	Log(MSE)	-7.4254	-6.2362	-5.4133	-6.5135
WN2	\hat{c}	0.9585	0.9776	0.9520	1.0596
	$\hat{\beta}$	0.2886	0.2630	0.2346	0.3943
	$\hat{\sigma}$	0.9161	0.9270	0.9260	0.9318
	Log(MSE)	-7.4049	-6.9731	-5.4128	-6.6882
KN	\hat{v}	1.5365	0.7924	0.972	0.3855
	\hat{b}	2.3122	1.9992	0.2293	2.1345
	$\hat{\sigma}$	0.8971	$6.0428e^{-08}$	0.8522	0.9418
	Log(MSE)	-6.9523	-5.3474	-5.4066	-5.6053
GPN	$\hat{\alpha}$	1.8310	0.8107	11.5337	6.7741
	\hat{b}	0.0980	0.7166	0.3563	0.9750
	$\hat{\sigma}$	0.9826	0.9812	1.0002	0.9594
	Log(MSE)	-4.9651	-6.1981	-5.3200	-4.5534
CIGN	$\hat{\lambda}$	0.1246	9.0120	0.9292	1.2897
	$\hat{\mu}$	0.1932	0.7383	0.1959	0.1558
	$\hat{\sigma}$	0.9646	0.7971	0.9851	0.9618
	Log(MSE)	-6.8053	-5.7352	-5.3200	-5.5378

Table 3.8 – The estimated parameters for each model for range resolution 3m, using PCFE method.

3.7 Conclusions

This chapter highlights high-resolution sea clutter modeling. Two approximate expressions for the Weibull plus thermal noise distributions have been proposed as models to fit real sea clutter data. First, the fitting using synthetic data have been used to validate these two models by means of the PCFE method and the method of moments matching. The experimental results at low and medium resolution of 60, 30 and 15m resolution reveal that the proposed models WN1 and WN2 provide a good fit to the sea data even if the presence of longer tailed cells. Moreover, at high-resolution 9 and 3m the proposed models consistently yields a good fit in most cells for like and cross-polarization data and outperform three widely used CG plus thermal noise distributions in all the cases studied. The two proposed models should be good candidates for modeling high-resolution sea clutter data.

Chapter 4

Sea Clutter Modeling Using Mixtures of Two Approximate Weibull Distributions plus Thermal Noise

Contents

4.1	Introduction	68
4.2	Mixture Models	68
4.3	Simulation Results and Discussions	71
4.4	Conclusions	84

Abstract

Robust marine surveillance using high-resolution radar requires an accurate description of the back-scatter from the sea and its environments. This chapter is considered as a continuation of the previous chapter and consists of studying the robustness of the mixture of the proposed Weibull approximations to model the sea clutter using the IPIX database.

4.1 Introduction

From the previous chapter, it was discussed that when the sea is observed at low grazing angle with high-resolution radar, the statistics of the clutter are mostly non-Gaussian, and tend to fit better to the proposed Weibull approximations against the CG models especially in the tail region. Another way to ensure the best fit for sea data is to use a mixture method of two distributions. In this context, Dong suggested a mixture of two K and two Weibull distributions to fit the sea clutter. It was found in this work that the KK distribution provides overall the best fit [36]. Rosenberg proposed the KK distribution to analyze the real sea data collected at medium to high grazing angles by the defense science technology organization (DSTO) Ingara fully polarimetric X-band radar. This model provides a good fit to real sea clutter data, as well as in the case of the presence of thermal noise. Also, the threshold required to achieve the CFAR characteristic is studied and compared to the K distribution [41]. Abraham *et al* suggested a mixture of Rayleigh and K models to represent active sonar data, the K Rayleigh mixture model provides a good fit to clutter sonar data [42]. Zhou *et al* proposed a statistical model consisting of a mixture of K and LN distributions for modeling the SAR data. This mixture is able to model and fit the clutter data, the target data, or a mixture of clutter and target data [42]. Also, Gouri *et al* used the sum and the mixture of the CIG, K and GP plus thermal noise distributions to model high-resolution IPIX sea data. All the results confirmed that the proposed method offers a good fit to sea clutter in most cases, especially in the tail region [18]. In this context, this chapter analyzes the sum and the mixture of the proposed Weibull models WN1 and WN2 to fit real sea data using the IPIX database and compares it with the mixture of CG models studied by Gouri *et al* in [18].

4.2 Mixture Models

In this section, we propose a mixture model describing the statistical properties of sea clutter data, the sum of two weighted PDFs is given by:

$$f(x) = kf_1(x|\theta_1) + (1 - k)f_2(x|\theta_2) \quad (4.1)$$

where $\theta = [k, \theta_1, \theta_2]$ is a vector of unknown parameters to be estimated at each estimation task, the weighting parameter $k \in [0, 1]$. The first model $f_1(x)$ or the second model $f_2(x)$ may follow one of the two proposed Weibull models, WN1 and WN2, described in chapter 3.

4.2.1 Mixture of WN1 and WN2 Model for Single Pulse

If the WN1 (3.60) and the WN2 (3.67) PDFs are described by $f_1(x)$ and $f_2(x)$ respectively, the mixture PDF of single pulse model is given by:

$$f(x) = k \frac{b^2 x^{b-1}}{\sqrt{\pi} a} \int_0^\infty \left(\frac{s}{a}\right)^{\frac{b}{2}-1} \frac{1}{\sqrt{s^2 + 2\sigma^2}^b} \exp \left[-\left(\frac{x}{\sqrt{s^2 + 2\sigma^2}}\right)^b - \left(\frac{s}{a}\right)^b \right] ds \\ + \frac{(1-k)2b}{x\sqrt{\pi}} \varepsilon \alpha \int_0^\infty \frac{1}{(w^{\frac{4}{b}} + 1)^{\frac{b}{2}}} \exp \left[-\frac{\varepsilon}{(w^{\frac{4}{b}} + 1)^{\frac{b}{2}}} - (\alpha^2 w^2) \right] dw \quad (4.2)$$

In this case, the CCDF obtained from a mixture of the WN1 (3.61) and WN2 (3.68) models is:

$$CCDF(x) = Prob(x > T) = \frac{kb}{a^{\frac{b}{2}} \sqrt{\pi}} \int_0^\infty s^{\frac{b}{2}-1} \left[1 - \gamma \left(1, \left(\frac{T}{\sqrt{s^2 + 2\sigma^2}}\right)^b \right) \right] \exp \left[-\left(\frac{s}{a}\right)^b \right] ds \\ + \frac{(1-k)2\alpha}{\sqrt{\pi}} \int_0^\infty \exp \left[-\frac{T^b}{(2\sigma^2)^{\frac{b}{2}} (w^{\frac{4}{b}} + 1)^{\frac{b}{2}}} - (\alpha^2 w^2) \right] dw \quad (4.3)$$

where $\varepsilon = (x^2/2\sigma^2)^{\frac{b}{2}}$, $\alpha = (2\sigma^2/a^2)^{\frac{b}{4}}$, and T is the threshold detection as mentioned in chapter 3. The shape and scale parameters are given respectively by: $c = 0.5b$, and $\beta = a2^{-2/b}$.

4.2.2 Mixture of WN1 and WN2 Model for Multiple Pulse

Based on the approximation (3.63), the mixture PDF of multiple pulse for WN1 (3.65) and WN2 (3.71) models is given by:

$$Nf(x) = \frac{kRb^2(Rx)^{Nb-1}}{\Gamma(N)a\sqrt{\pi}} \int_0^\infty \left(\frac{s}{a}\right)^{\frac{b}{2}-1} \frac{1}{\sqrt{s^2 + 2\sigma^2}^{Nb}} \exp \left[-\left(\frac{Rx}{\sqrt{s^2 + 2\sigma^2}}\right)^b - \left(\frac{s}{a}\right)^b \right] ds \\ + \frac{(1-k)2b\alpha}{\Gamma(N)x\sqrt{\pi}} \left(\frac{R^2x^2}{2\sigma^2}\right)^{\frac{Nb}{2}} \int_0^\infty \frac{1}{(w^{\frac{4}{b}} + 1)^{\frac{Nb}{2}}} \exp \left[-\frac{\left(\frac{R^2x^2}{2\sigma^2}\right)^{\frac{b}{2}}}{(w^{\frac{4}{b}} + 1)^{\frac{b}{2}}} - (\alpha^2 w^2) \right] dw \quad (4.4)$$

The mixture CCDF of multiple pulse for WN1 (3.66) and WN2 (3.72) models is given by:

$$NCCDF(x) = Prob(x > T) = \frac{kb}{a^{\frac{b}{2}} \sqrt{\pi}} \int_0^\infty s^{\frac{b}{2}-1} \left[1 - \frac{\gamma \left(N, \left(\frac{RT}{\sqrt{s^2 + 2\sigma^2}}\right)^b \right)}{\Gamma(N)} \right] \exp \left[-\left(\frac{s}{a}\right)^b \right] ds \\ + \frac{(1-k)2R^{Nb}\alpha(2\sigma^2)^{\frac{b}{2}}}{\Gamma(N)\sqrt{\pi}(2\sigma^2)^{\frac{Nb}{2}}} \int_0^\infty \frac{(w^{\frac{4}{b}} + 1)^{\frac{b}{2}}}{(w^{\frac{4}{b}} + 1)^{\frac{Nb}{2}}} \exp \left[-\frac{R^b T^b}{(2\sigma^2)^{\frac{b}{2}} (w^{\frac{4}{b}} + 1)^{\frac{b}{2}}} - (\alpha^2 w^2) \right] dw \quad (4.5)$$

4.2.3 Mixture of The Compound Gaussian plus Noise Models

To assess the performance of the proposed mixture Weibull models to fit high-resolution sea clutter data, the mixture of CG are recalled here and used for comparison purposes. The fitting performance of these models has been studied and discussed by Gourri *et al* in [18]. Several combinations between KN, GPN and CIGN models can be obtained in (4.1). When the KN and the CIGN models are described by $f_1(x)$ and $f_2(x)$ respectively, the PDF and CCDF are given by:

$$f(x) = \int_0^\infty \frac{kx}{\sigma^2 + 2y^2/\pi} \exp\left[-\frac{x^2}{2\sigma^2 + 4y^2/\pi}\right] \frac{2b^{2\nu}y^{2\nu-1}}{\Gamma(\nu)} \exp(-b^2y^2) dy \\ + (1-k) \int_0^\infty \frac{x}{\sigma^2 + 2y^2/\pi} \exp\left[-\frac{x^2}{2\sigma^2 + 4y^2/\pi}\right] \frac{\lambda^{\frac{3}{2}}}{\sqrt{2\pi}y^{\frac{3}{2}}} \exp\left[-\lambda \frac{(y-\mu)^2}{2\mu^2y}\right] dy \quad (4.6)$$

$$CCDF(x) = Prob(x > T) = \int_0^\infty k \exp\left[-\frac{T^2}{2\sigma^2 + 4y^2/\pi}\right] \frac{2b^{2\nu}y^{2\nu-1}}{\Gamma(\nu)} \exp(-b^2y^2) dy \\ + (1-k) \int_0^\infty \exp\left[-\frac{T^2}{2\sigma^2 + 4y^2/\pi}\right] \frac{\lambda^{\frac{3}{2}}}{\sqrt{2\pi}y^{\frac{3}{2}}} \exp\left[-\lambda \frac{(y-\mu)^2}{2\mu^2y}\right] dy \quad (4.7)$$

When the CIGN and the GPN models are described by $f_1(x)$ and $f_2(x)$ respectively, the PDF and CCDF are given by:

$$f(x) = \int_0^\infty \frac{kx}{\sigma^2 + 2y^2/\pi} \exp\left[-\frac{x^2}{2\sigma^2 + 4y^2/\pi}\right] \frac{\lambda^{\frac{3}{2}}}{\sqrt{2\pi}y^{\frac{3}{2}}} \exp\left[-\lambda \frac{(y-\mu)^2}{2\mu^2y}\right] dy \\ + (1-k) \int_0^\infty \frac{x}{\sigma^2 + 2y^2/\pi} \exp\left[-\frac{x^2}{2\sigma^2 + 4y^2/\pi}\right] \frac{b^\alpha y^{-\alpha-1}}{\Gamma(\alpha)} \exp\left[-\frac{b}{y}\right] dy \quad (4.8)$$

$$CCDF(x) = Prob(x > T) = \int_0^\infty k \exp\left[-\frac{T^2}{2\sigma^2 + 4y^2/\pi}\right] \frac{\lambda^{\frac{3}{2}}}{\sqrt{2\pi}y^{\frac{3}{2}}} \exp\left[-\lambda \frac{(y-\mu)^2}{2\mu^2y}\right] dy \\ + (1-k) \int_0^\infty \exp\left[-\frac{T^2}{2\sigma^2 + 4y^2/\pi}\right] \frac{b^\alpha y^{-\alpha-1}}{\Gamma(\alpha)} \exp\left[-\frac{b}{y}\right] dy \quad (4.9)$$

When the GPN and the KN models are described by $f_1(x)$ and $f_2(x)$ respectively, the PDF and CCDF are given by:

$$\begin{aligned}
f(x) &= \int_0^\infty \frac{kx}{\sigma^2 + 2y^2/\pi} \exp\left[-\frac{x^2}{2\sigma^2 + 4y^2/\pi}\right] \frac{b^\alpha y^{-\alpha-1}}{\Gamma(\alpha)} \exp\left[-\frac{b}{y}\right] dy \\
&+ \int_0^\infty \frac{(1-k)x}{\sigma^2 + 2y^2/\pi} \exp\left[-\frac{x^2}{2\sigma^2 + 4y^2/\pi}\right] \frac{2b^{2\nu} y^{2\nu-1}}{\Gamma(\nu)} \exp(-b^2 y^2) dy
\end{aligned} \tag{4.10}$$

$$\begin{aligned}
CCDF(x) = Prob(x > T) &= \int_0^\infty k \exp\left[-\frac{T^2}{2\sigma^2 + 4y^2/\pi}\right] \frac{b^\alpha y^{-\alpha-1}}{\Gamma(\alpha)} \exp\left[-\frac{b}{y}\right] dy \\
&+ (1-k) \int_0^\infty \exp\left[-\frac{T^2}{2\sigma^2 + 4y^2/\pi}\right] \frac{2b^{2\nu} y^{2\nu-1}}{\Gamma(\nu)} \exp(-b^2 y^2) dy
\end{aligned} \tag{4.11}$$

4.3 Simulation Results and Discussions

In this section, we assess the fitting performance of the proposed mixture model for real sea IPIX data, by comparing the real CCDFs and PDFs with the estimated CCDFs and PDFs using the PCFE method. Also, we compare our results with the results obtained by the mixture of CG models studied by Gouri *et al* in [18]. The MSE values are calculated from the fitted and empirical CCDFs curves. The CS values are calculated from the fitted and empirical PDFs curves. In the following, several experimental studies are conducted to examine the modeling assessments of the mixture models with different IPIX radar resolutions. All the technical characteristics of each IPIX file used in this section are available in Table 3.2 and 3.3.

4.3.1 Range Resolutions 60, 30 and 15m

First, we perform the fitting performance when the radar operates at a low resolution of 60m, using (19980204_221307_ANTSTEP) file, in which the azimuth resolution is set 0.3571° . For HH polarization mode, and 17th range cells. It can be seen in Figure 4.1 that the CCDF of the GPN+KN model produces the worst performance fit to the IPIX data. According to the MSE criterion, the WN1+WN2 model is the closest to the real sea data, (Table 4.1). We note the same performance for the PDF curves, Figure 4.2. For the same range cells, and cross VH polarization mode. A very good fit was achieved by all CCDF mixture models to the actual IPIX data, especially in the tail region, as shown in Figure 4.3. The mixture CCDF of the proposed WN1 and WN2 models provides the best tail approximation with the smallest MSE values, (Table 4.1). On the other hand, the PDF curves show less accurate performance than the CCDFs curves, (Figure 4.4).

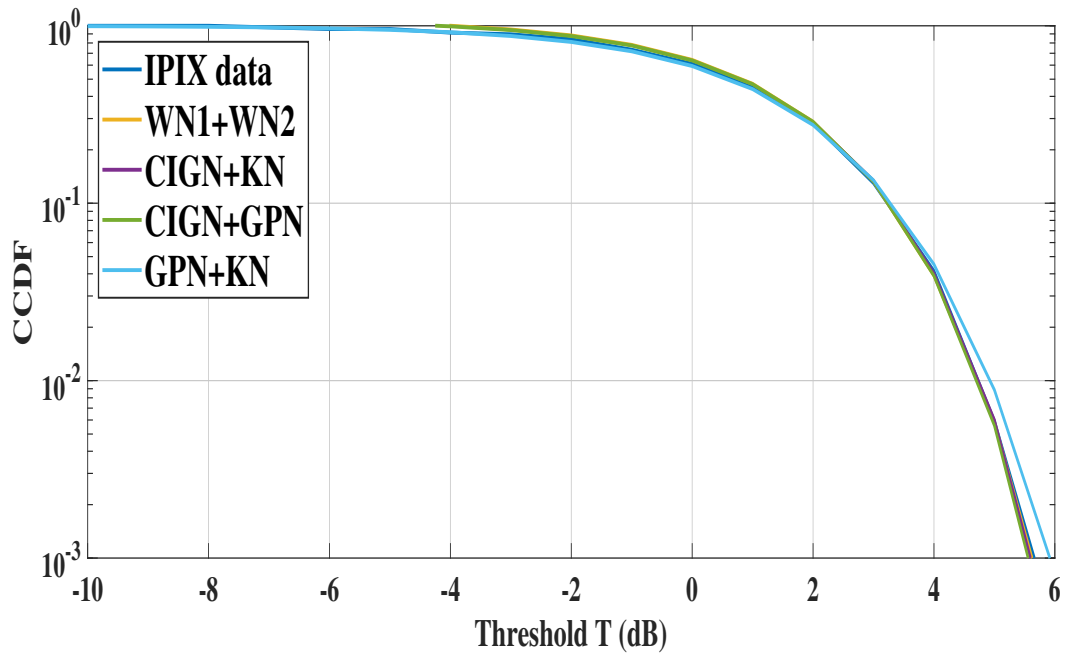


Figure 4.1 – CCDF curves, 60m, HH polarization, 17th range cell, Azimuth resolution = 0.3571° .

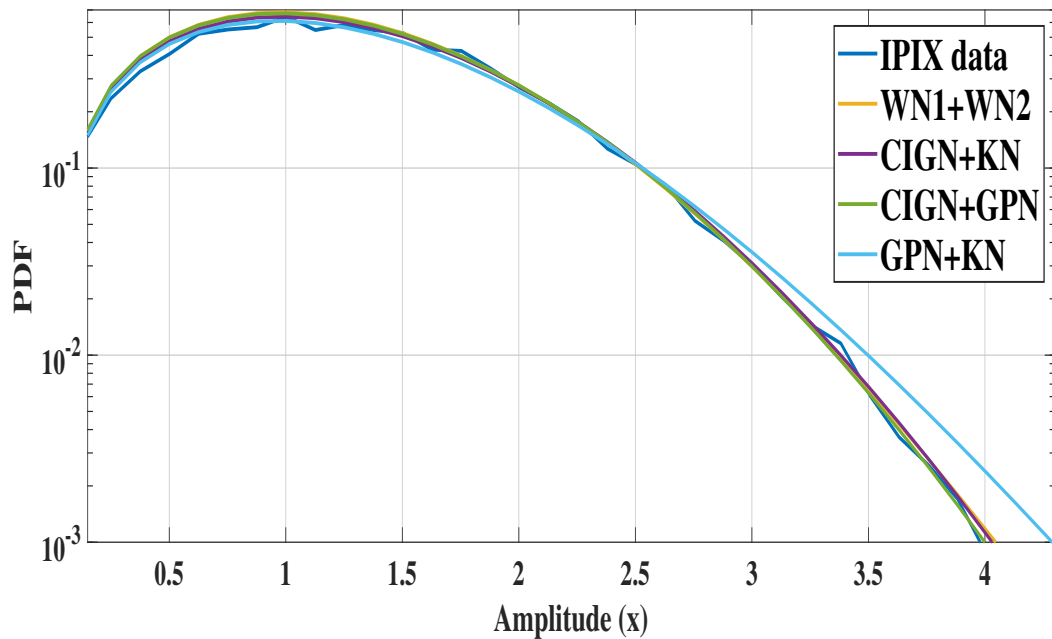


Figure 4.2 – PDF curves, 60m, HH polarization, 17th range cell, Azimuth resolution = 0.3571° .

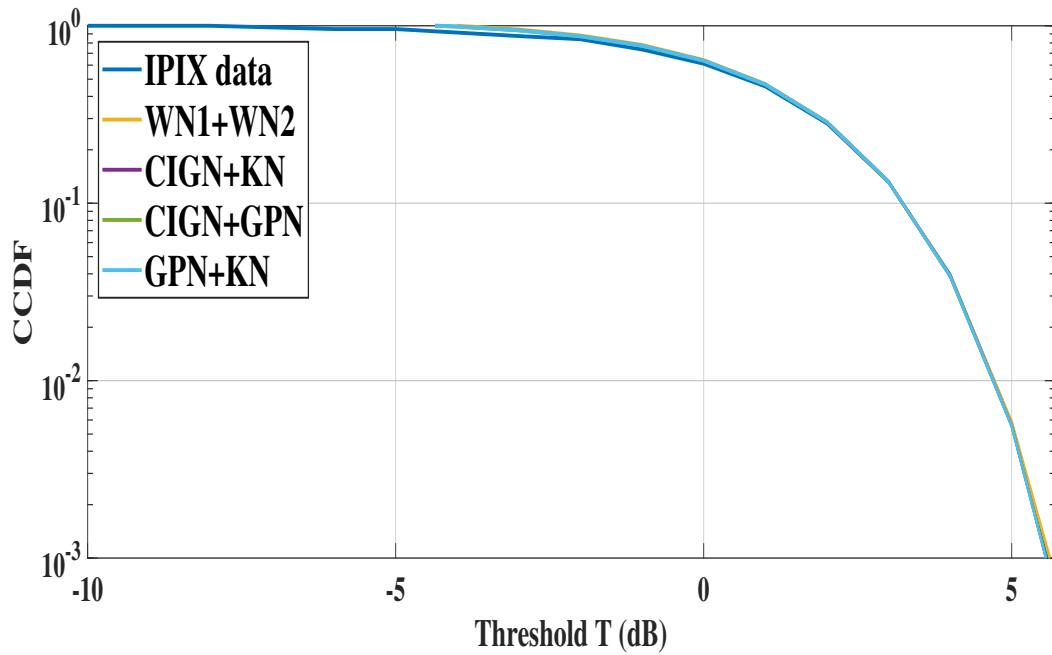


Figure 4.3 – CCDF curves, 60m, VH polarization, 17th range cell, Azimuth resolution = 0.3571° .

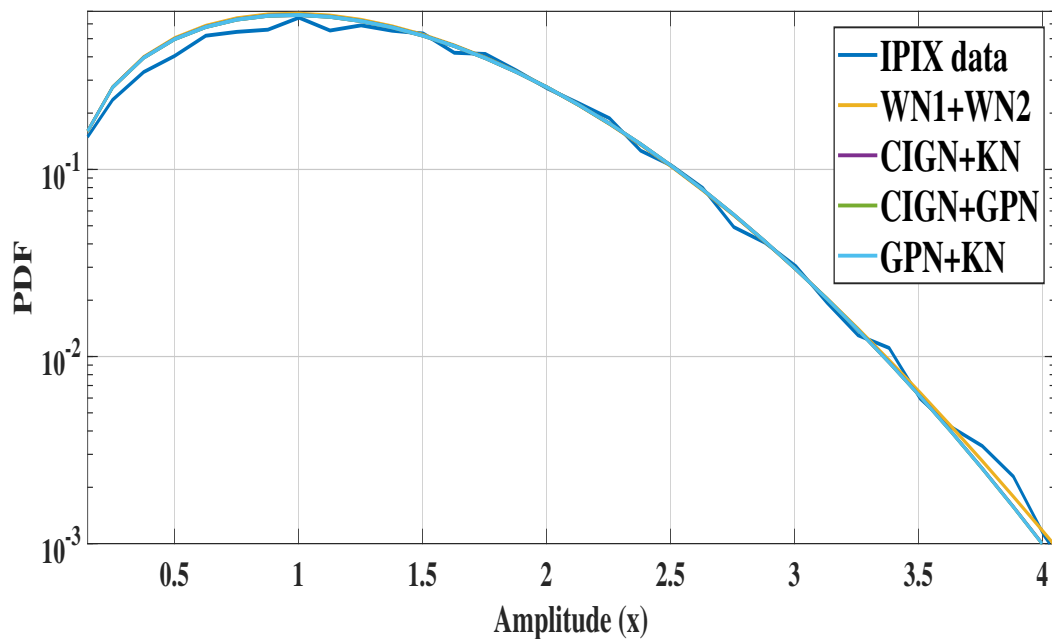


Figure 4.4 – PDF curves, 60m, VH polarization, 17th range cell, Azimuth resolution = 0.3571° .

We repeat the fitting performance of the proposed models by increasing the radar resolution to 30m. For the (19980204_194537_ANTSTEP) file, 20th range cells, VV polarization mode, and azimuth resolution equal to 16.1499° . We observe in Figure 4.5, all CG mixture models show long tails, where the mixture CIGN+KN model provides the poorest fitting performance. The WN1+WN2 model produces the best results with the smallest MSE values, (Table 4.1). The same pattern observed for the PDFs curves, (Figure 4.6).

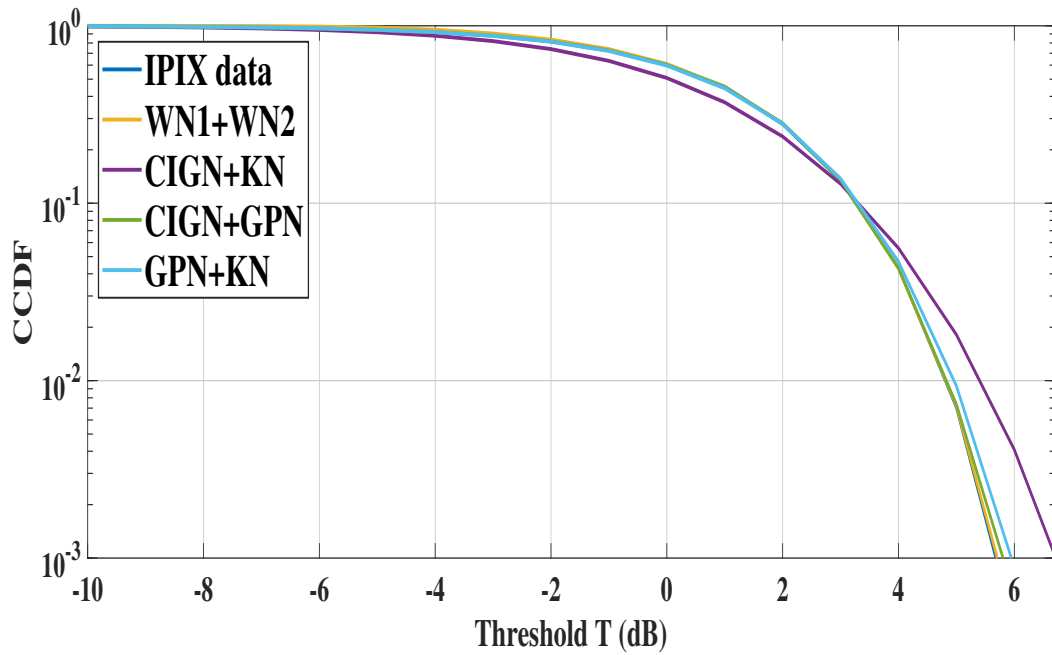


Figure 4.5 – CCDF curves, 30m, VV polarization, 20th range cell, Azimuth resolution = 16.1499°.

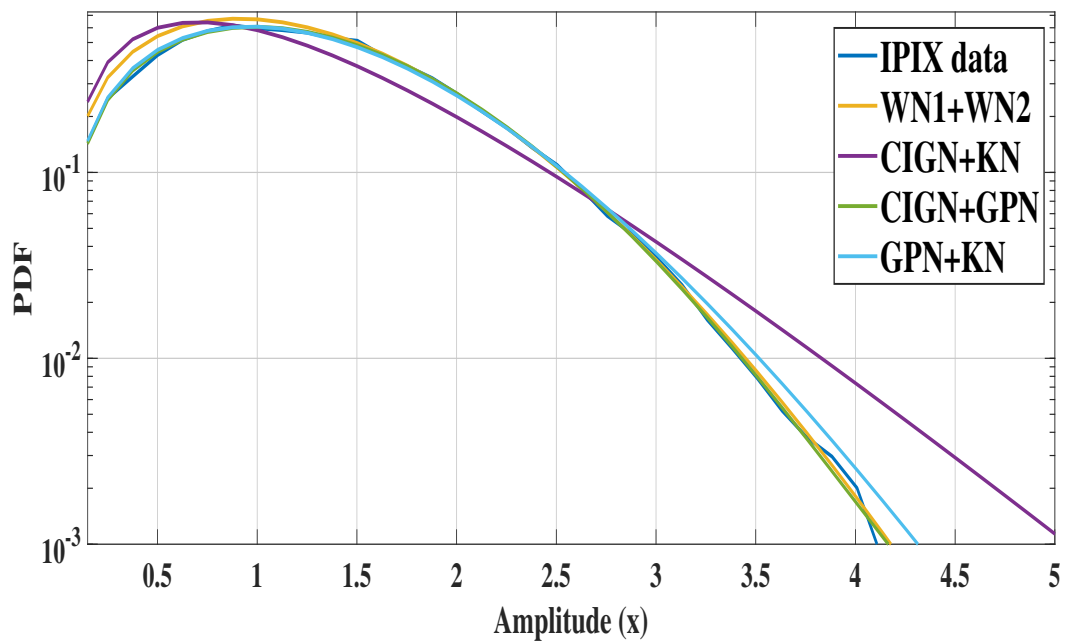


Figure 4.6 – PDF curves, 30m, VV polarization, 20th range cell, Azimuth resolution = 16.1499°.

For the same range resolution, HV mode, and 17th range cells, Figure 4.7 and 4.8 show that all the mixture CCDFs and PDFs curves exhibit a good fit to real sea IPIX data. The best performance was achieved using the WN1+WN2 mixture model with the smallest MSE and CS metrics, (Table 4.1).

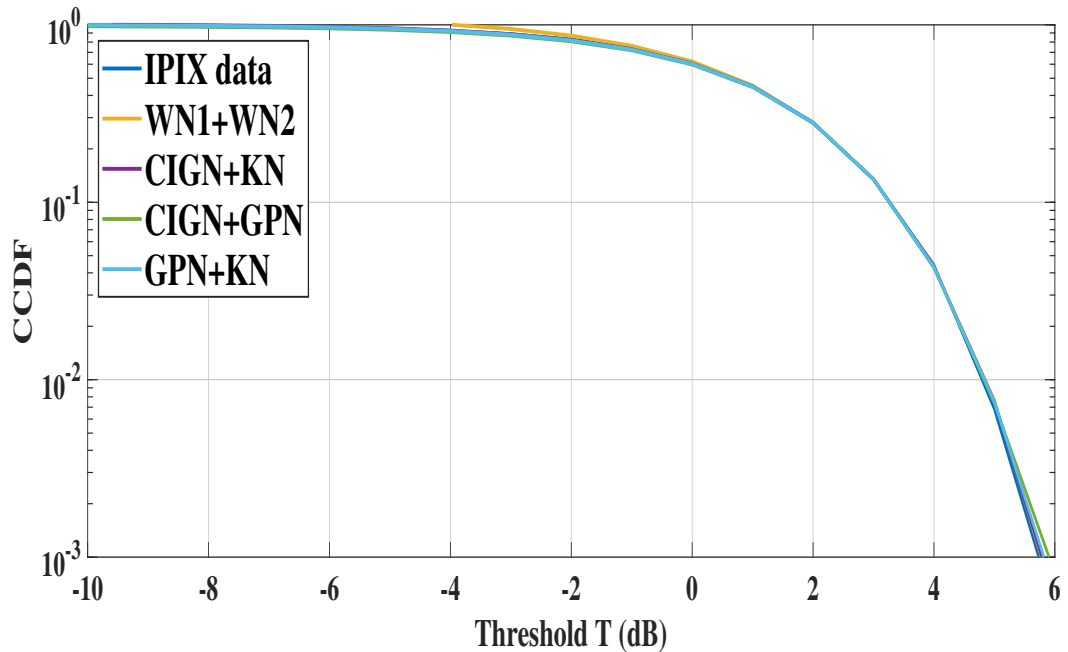


Figure 4.7 – CCDF curves, 30m, HV polarization, 17th range cell, Azimuth resolution = 16.1499°.

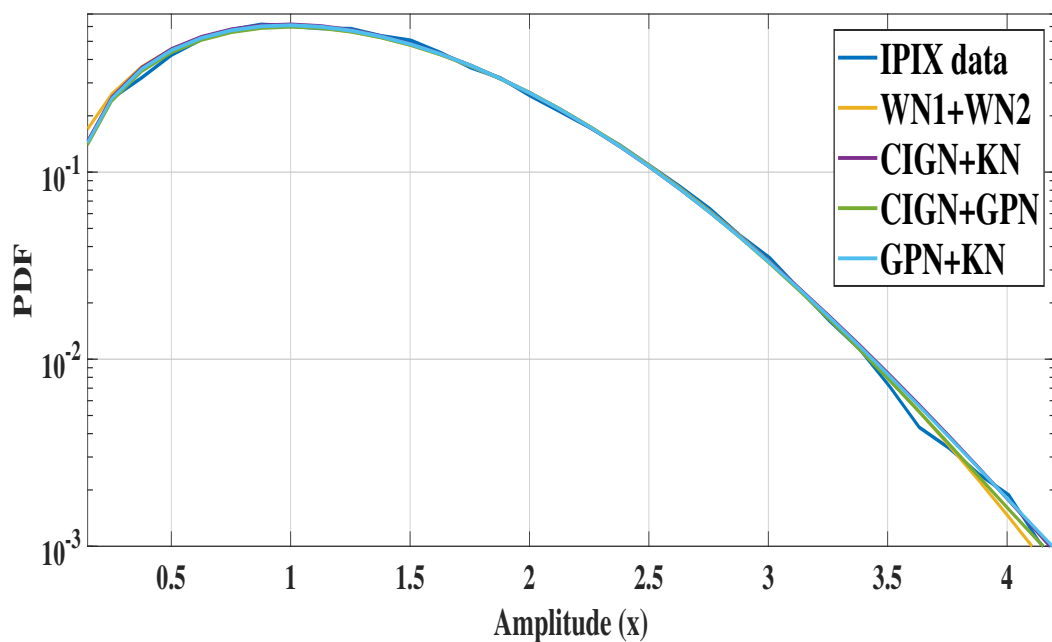


Figure 4.8 – PDF curves, 30m, HV polarization, 17th range cell, Azimuth resolution = 16.1499°.

Models	Parameters and Metrics	60m HH 17 th	60m VH 17 th	30m VV 20 th	30m HV 17 th
WN1+WN2	\hat{c}	0.9921	0.8695	1.1186	0.9523
	$\hat{\beta}$	0.3680	1.1258	0.6055	1.2053
	$\hat{\sigma}$	1.0012	0.1204	0.8170	$6.2863e^{-07}$
	\hat{k}	0.8963	0.4589	0.5720	0.5869
	Log(MSE)	-6.8010	-5.9958	-7.3633	-6.3198
	Log(CS)	-3.3650	-4.6963	-4.0167	-4.3670
CIGN+KN	\hat{c}	0.9836	0.8001	0.2822	1.0036
	$\hat{\beta}$	0.3452	1.2200	0.3302	1.1959
	$\hat{\sigma}$	0.9963	0.0998	$3.5075e^{-11}$	$5.9003e^{-06}$
	\hat{k}	0.9201	0.5089	0.9675	0.6111
	Log(MSE)	-6.2117	-5.5583	-2.0028	-6.0015
	Log(CS)	-3.2014	-4.1709	-1.0251	-4.40175
CIGN+GPN	\hat{v}	1.0121	0.7586	0.3029	1.2098
	\hat{b}	0.3388	0.2985	0.6970	1.5950
	$\hat{\sigma}$	0.9769	1.1232	0.7909	0.0120
	\hat{k}	0.7201	0.6627	0.5720	0.3639
	Log(MSE)	-6.0007	-5.4211	-6.5801	-5.7157
	Log(CS)	-3.0130	-4.4580	-3.6300	-4.2010
GPN+KN	$\hat{\alpha}$	1.5774	0.9922	0.4162	1.1591
	\hat{b}	0.1251	0.2237	0.5970	1.0655
	$\hat{\sigma}$	0.3359	1.3278	0.8309	$6.5128e^{-08}$
	\hat{k}	0.4583	0.8900	0.5133	0.5006
	Log(MSE)	-5.0253	-5.5539	-5.5848	-6.2101
	Log(CS)	-2.6258	-4.5348	-3.9474	-4.3669

Table 4.1 – The estimated parameters for each model for range resolutions 60 and 30m, using PCFE method, and the metric tests.

At 15m radar resolution where the clutter is a bit spiky, the first performance was conducted for the 11th range cells of (19980204_221700_ANTSTEP) file, azimuth resolution is 0.2966° and HH polarization mode. The WN1+WN2 CCDF model consistently gives a good fit in the body and in the tail region of the IPIX data. On the contrary, CG models provide the worst fit performance, where the CIGN+GPN CCDF shows the largest deviation in the tail region as shown in Figure 4.9, with the worst MSE metrics, (Table 4.2). The same results are obtained for the PDFs of mixtures, (Figure 4.10).

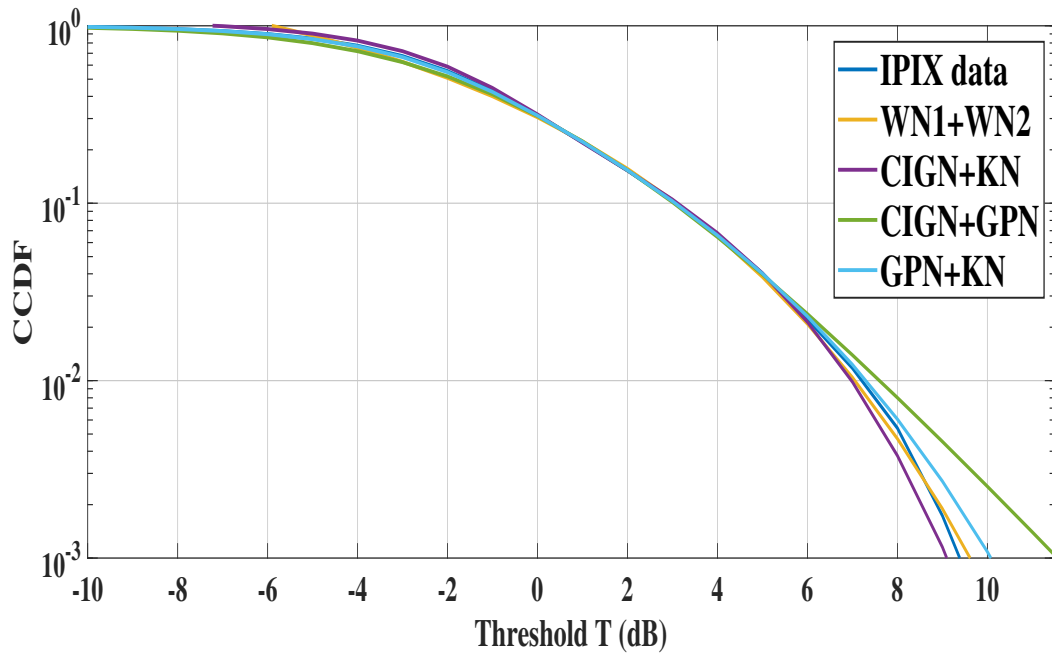


Figure 4.9 – CCDF curves, 15m, HH polarization, 11th range cell, Azimuth resolution = 0.2966° .

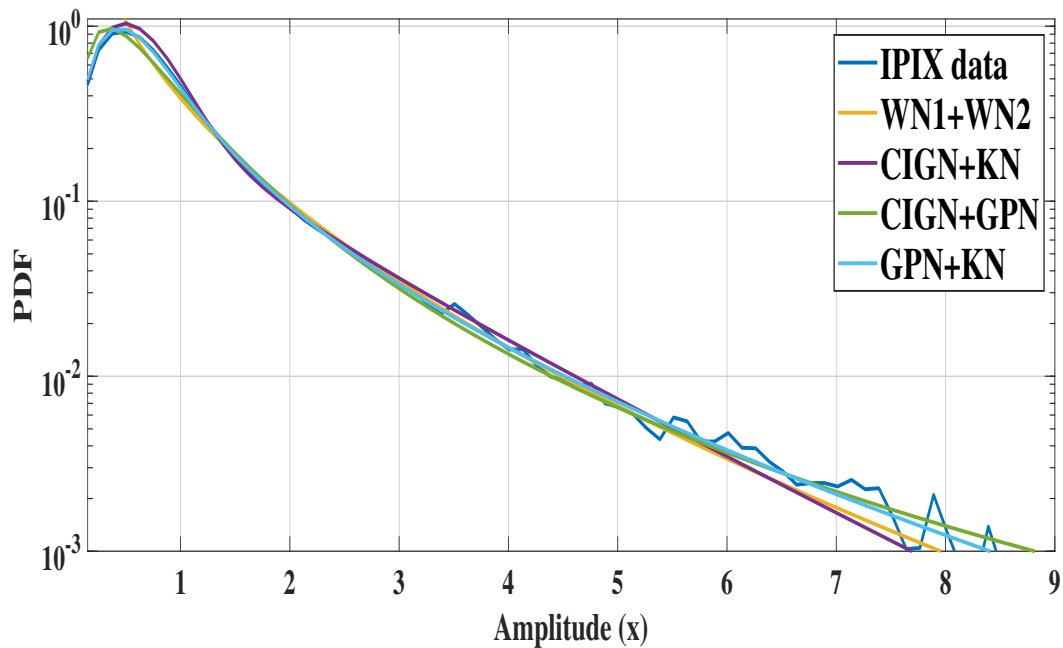


Figure 4.10 – PDF curves, 15m, HH polarization, 11th range cell, Azimuth resolution = 0.2966° .

Finally, for the same range resolution, VV mode, and 22nd. We observe in Figure 4.11 and 4.12 respectively an excellent fitting performance for all the mixture models. The proposed model WN1+WN2 provides the best MSE and CS results, (Table 4.2).

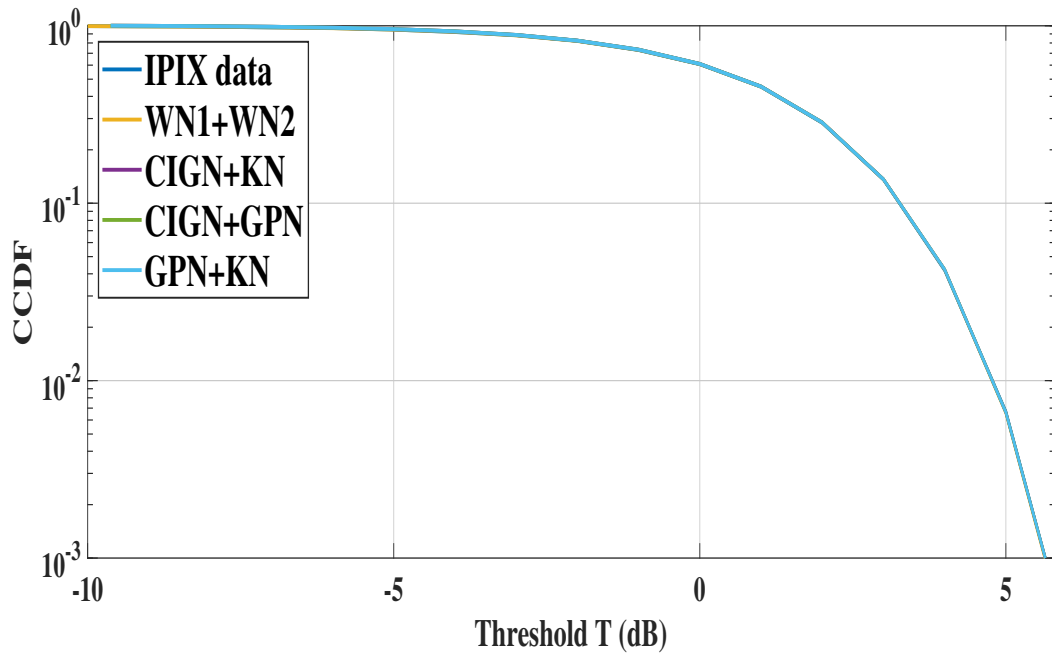


Figure 4.11 – CCDF curves, 15m, VV polarization, 22nd range cell, Azimuth resolution = 0.2966°.

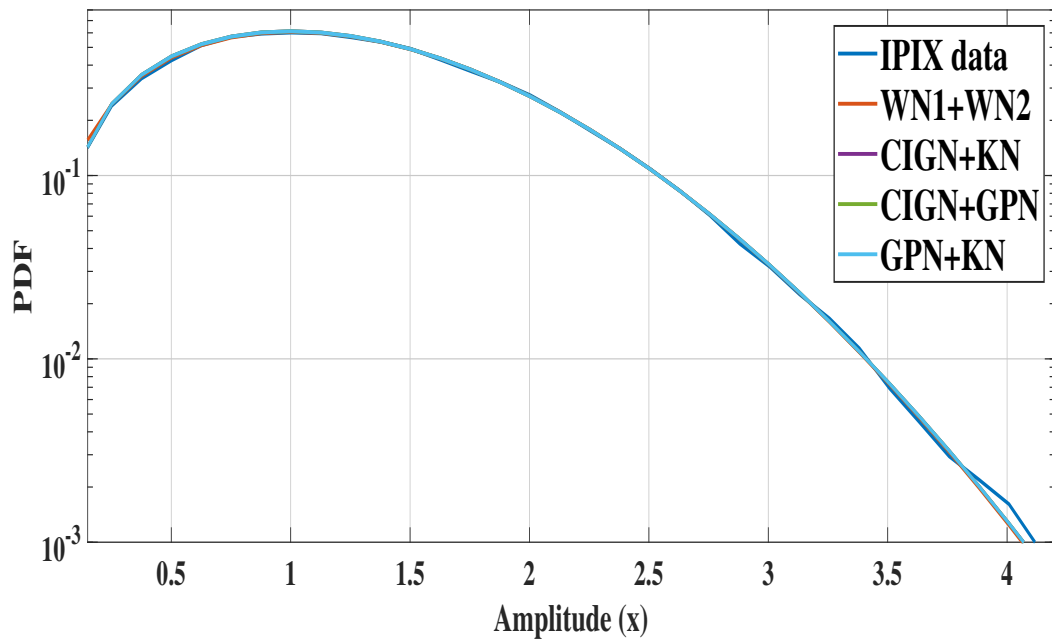


Figure 4.12 – PDF curves, 15m, VV polarization, 22nd range cell, Azimuth resolution = 0.2966°.

4.3.2 Range Resolutions 9, and 3m

In this subsection, we examine the fitting performance when the radar operates at a high-resolution of 9 and 3m, where the sea clutter becomes spikier and intensive. We start with the 9m (19980204_221908_ANTSTEP) file, VV polarization mode, and 15th range cells.

In Figure 4.13 it is clear that all the mixture CCDFs show accurate fit, especially in the tail region. According to MSE measurement, the best approximation of the tail is achieved by the WN1+WN2 CCDF, (Table 4.2). In addition, mixture PDFs show a good fit but with less tail approximation than the CCDFs models, (Figure 4.14).

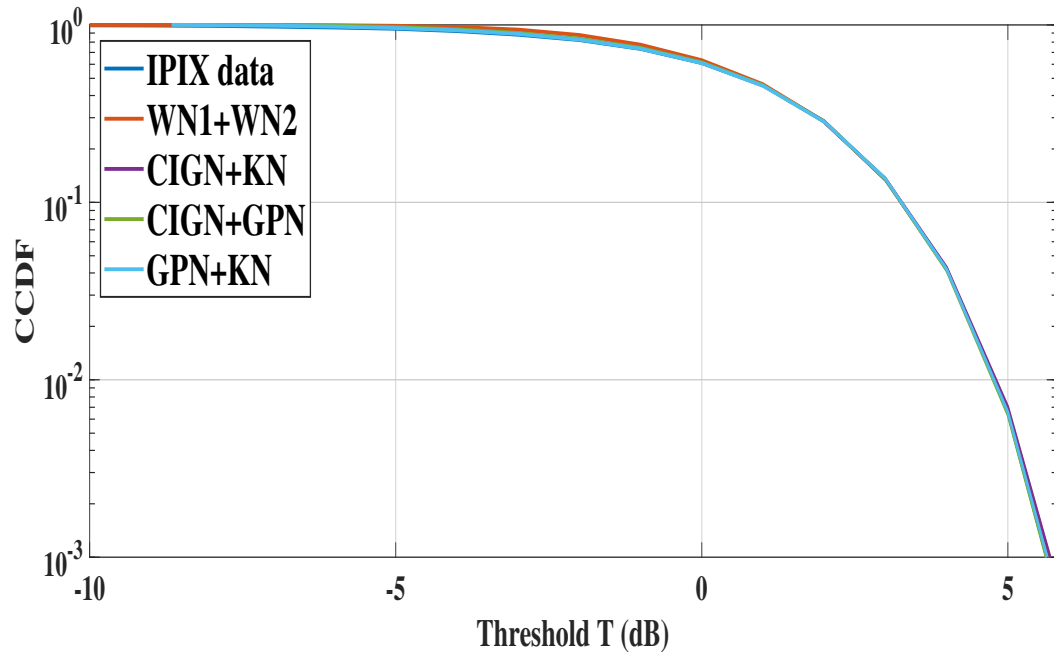


Figure 4.13 – CCDF curves, 9m, VV polarization, 15th range cell, Azimuth resolution = 0.3241°.

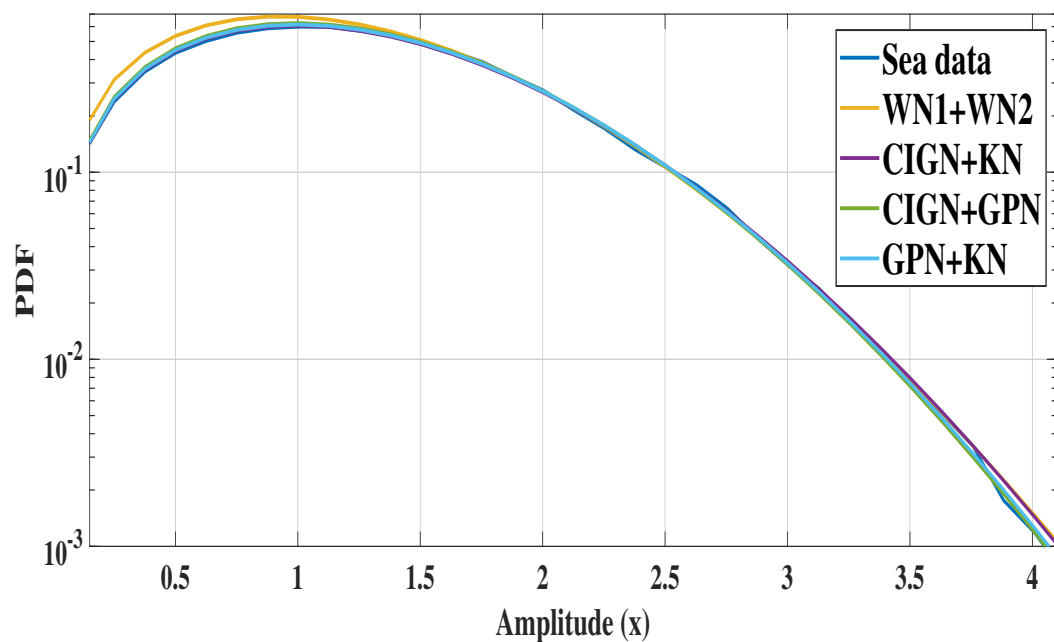


Figure 4.14 – PDF curves, 9m, VV polarization, 15th range cell, Azimuth resolution = 0.3241°.

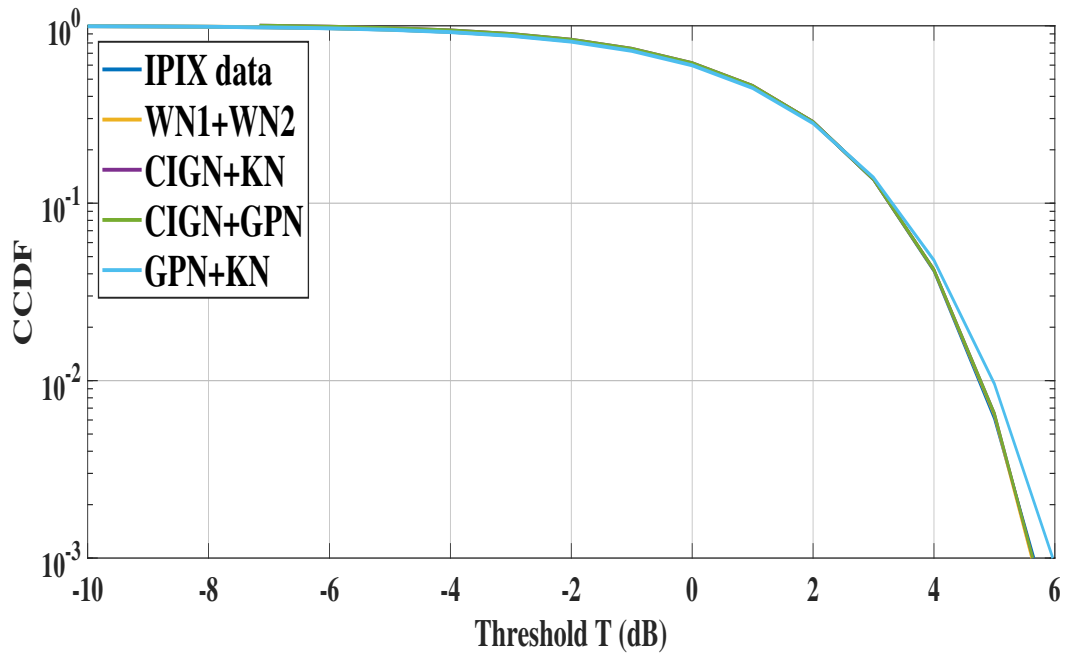


Figure 4.15 – CCDF curves, 9m, HV polarization, 3rd range cell, Azimuth resolution = 0.3241°.

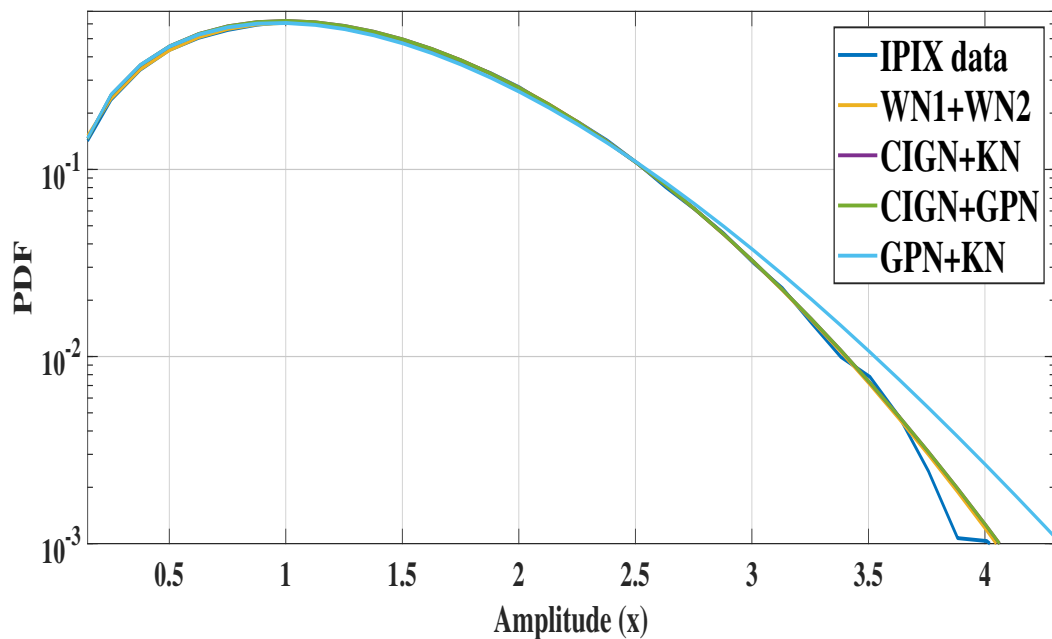


Figure 4.16 – PDF curves, 9m, HV polarization, 3rd range cell, Azimuth resolution = 0.3241°.

We repeat the same test for the same range resolution, HV polarization mode, and 3rd range cells. In this case the GPN+KN CCDF produces the worst tail approximation, as shown in Figure 4.15. According to the MSE metric, the best performance is achieved by the WN1+WN2 model followed by the CIGN+GPN model, (Table 4.3). For the mixture PDFs, All the models show a poor tail approximation, (Figure 4.16).

Models	Parameters and Metrics	15m HH 11 th	15m VV 22 nd	9m VV 15 th	9m HV 3 rd
WN1+WN2	\hat{c}	0.9330	1.4381	0.5702	0.1286
	$\hat{\beta}$	0.2106	1.1901	0.3390	0.3610
	$\hat{\sigma}$	1.3805	$3.6879e^{-05}$	0.2369	$4.4808e^{-08}$
	\hat{k}	0.1548	0.9802	0.6696	0.4851
	Log(MSE)	-5.9657	-6.3966	-6.6369	-6.6790
	Log(CS)	-3.5751	-3.9650	-4.1680	-3.9601
CIGN+KN	\hat{c}	1.2125	1.3666	0.5859	0.1952
	$\hat{\beta}$	0.3657	0.9196	0.2898	0.4088
	$\hat{\sigma}$	1.0304	$5.1861e^{-07}$	0.3691	0.0175
	\hat{k}	0.4048	0.7028	0.5698	0.4118
	Log(MSE)	-4.3319	-6.5025	-6.5129	-6.6001
	Log(CS)	-3.0025	-3.9622	-4.0169	-3.8580
CIGN+GPN	\hat{v}	1.9256	1.1285	0.7003	0.1696
	\hat{b}	0.7926	1.3002	0.1927	0.4182
	$\hat{\sigma}$	1.5902	$6.3701e^{-04}$	0.2322	$5.6729e^{-11}$
	\hat{k}	0.8259	0.8075	0.7115	0.5009
	Log(MSE)	-2.6235	-6.5607	-6.4874	-6.1922
	Log(CS)	-2.9199	-3.3185	-3.8968	-3.3705
GPN+KN	$\hat{\alpha}$	1.0696	0.9825	0.6981	1.3108
	\hat{b}	0.3199	0.9758	0.2020	1.285
	$\hat{\sigma}$	1.1302	0.0058	0.3900	1.0285
	\hat{k}	0.3002	0.9336	0.7225	0.1852
	Log(MSE)	-4.5281	-6.3705	-6.3699	-5.0014
	Log(CS)	-3.1120	-3.7308	-4.3258	-2.1963

Table 4.2 – The estimated parameters for each model for range resolutions 15 and 9m, using PCFE method.

Finally, to verify whether the proposed CCDF mixture is suitable for high-resolution 3m sea data, we applied the test on (19980205_185111_ANTSTEP) file, HH polarization data, and 6th range cell. All results obtained with this resolution do not show any statistically significant differences compared to the results obtained for the resolution of 9m. The mixture WN1+WN2 model shows the best fit to real IPIX data and provides the best tails approximation, as shown in Figure 4.17, and Figure 4.18, with the smallest metrics tests, (Table 4.3). Also, The same results obtained from the 17th range cell and VV polarization mode, the WN1+WN2 model shows the best fit and provides the accurate tail region to ral IPIX data, (Figures 4.19 and Figure 4.20).

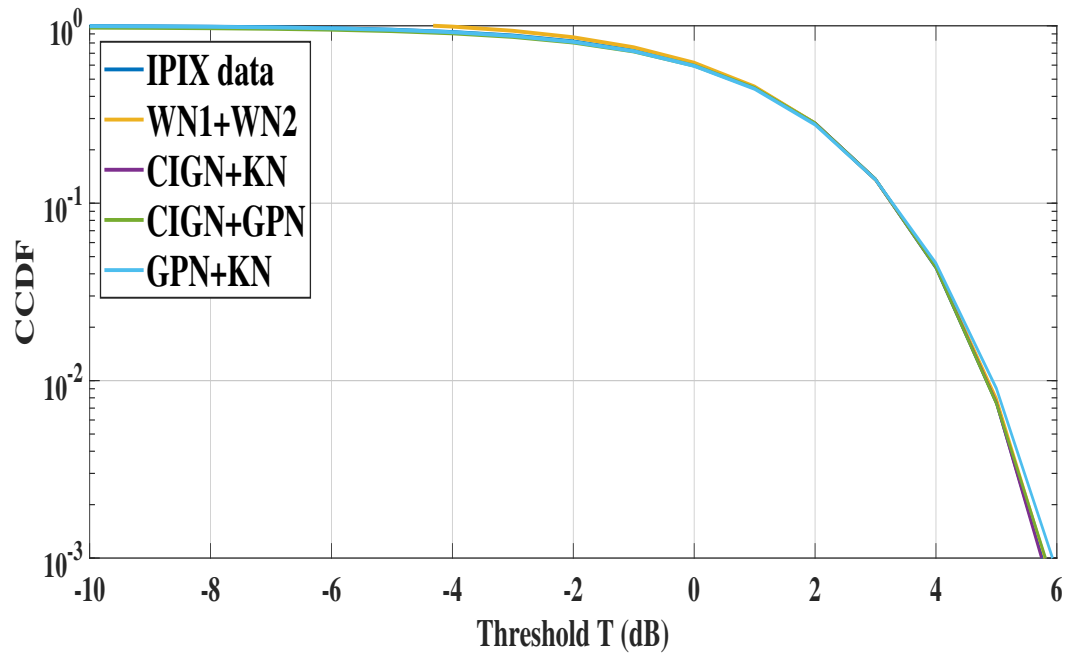


Figure 4.17 – CCDF curves, 3m, HH polarization, 6th range cell, Azimuth resolution = 44.8956° .

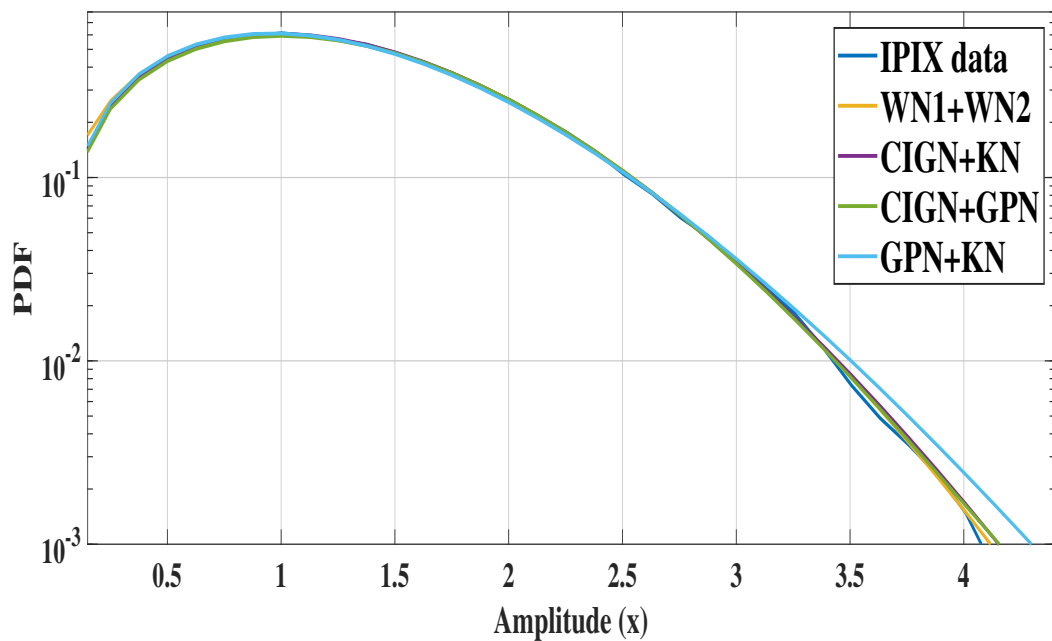


Figure 4.18 – PDF curves, 3m, HH polarization, 6th range cell, Azimuth resolution = 44.8956° .

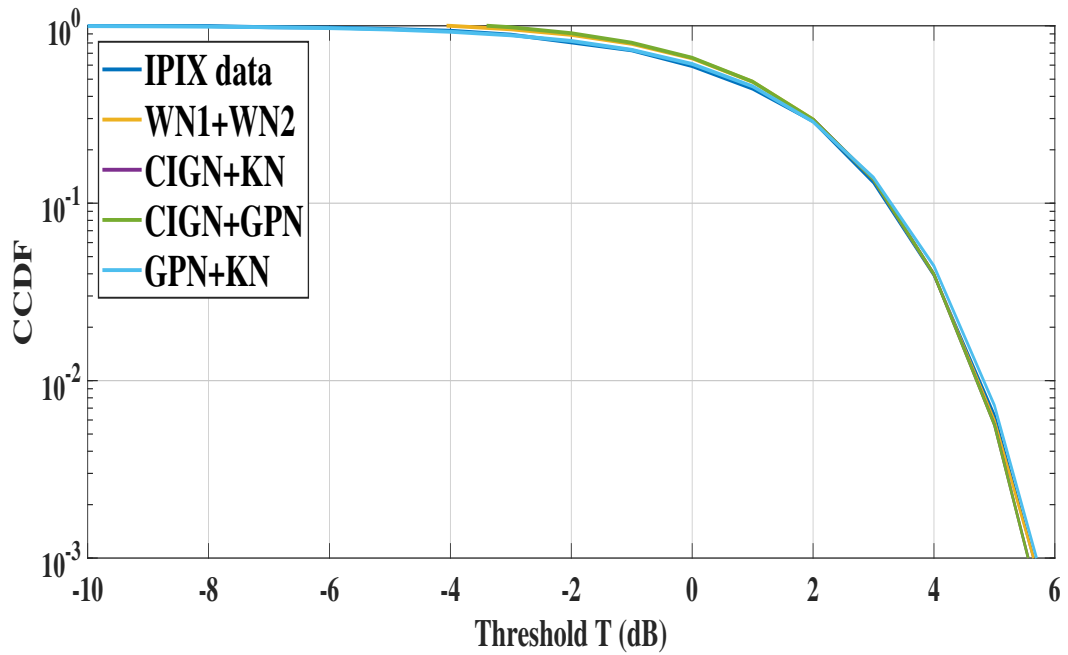


Figure 4.19 – CCDF curves, 3m, VV polarization, 17th range cell, Azimuth resolution = 44.8956° .

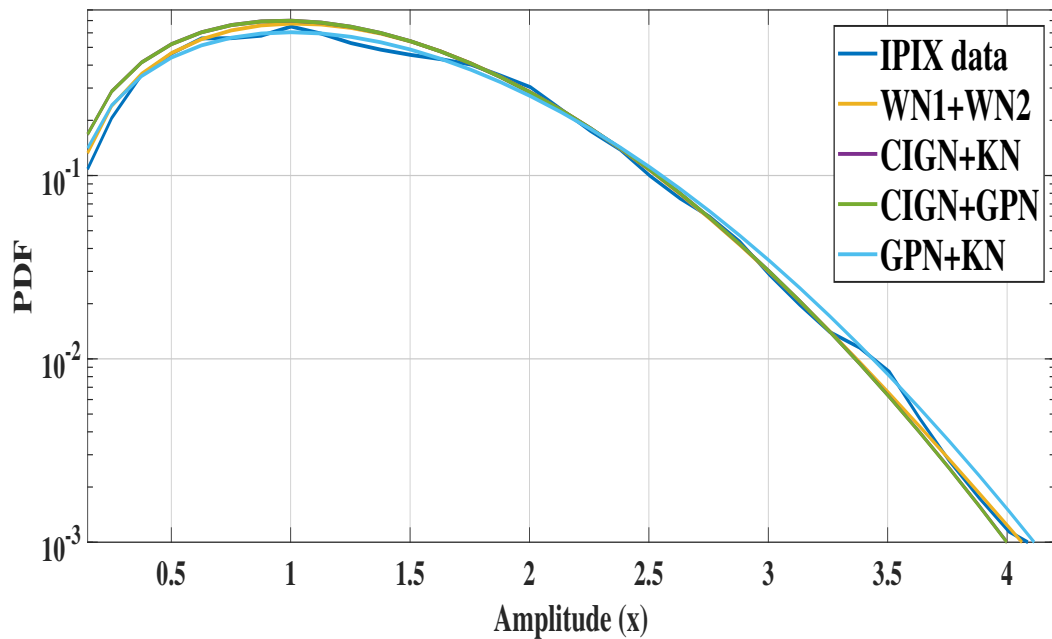


Figure 4.20 – PDF curves, 3m, VV polarization, 17th range cell, Azimuth resolution = 44.8956° .

Models	Parameters and Metrics	3m HH 6 th	3m VV 17 th
WN1+WN2	\hat{c}	0.5368	1.1125
	$\hat{\beta}$	0.3006	0.0981
	$\hat{\sigma}$	0.9820	$5.8005e^{-07}$
	\hat{k}	0.8379	0.9217
	Log(MSE)	-6.9625	-6.5081
	Log(CS)	-4.2514	-4.4175
CIGN+KN	\hat{c}	0.5772	1.0796
	$\hat{\beta}$	0.3127	0.1101
	$\hat{\sigma}$	0.8231	$5.9045e^{-09}$
	\hat{k}	0.8002	0.8901
	Log(MSE)	-6.5046	-6.3615
	Log(CS)	-4.1307	-3.9302
CIGN+GPN	\hat{v}	0.6018	1.1896
	\hat{b}	0.2968	0.2498
	$\hat{\sigma}$	0.9110	$6.8645e^{-11}$
	\hat{k}	0.6963	0.9926
	Log(MSE)	-5.6613	-5.6916
	Log(CS)	-3.9920	-4.2793
GPN+KN	$\hat{\alpha}$	0.9018	1.0065
	\hat{b}	2.1045	0.4817
	$\hat{\sigma}$	1.785	0.0125
	\hat{k}	0.1336	0.8967
	Log(MSE)	-5.0117	-6.3011
	Log(CS)	-3.1258	-3.5528

Table 4.3 – The estimated parameters for each mixture model for range resolutions 3m, using PCFE method.

4.4 Conclusions

Modeling sea clutter using real IPIX data is discussed in this section. All experimental results confirmed that the statistical mixture model generated by the two approximations WN1 and WN2 provides the best fit for the real data outperforming the CG models in most cases.

Chapter 5

Two Novel Radar Detectors for Spiky Sea Clutter With the Presence of Thermal Noise and Interfering Targets

Contents

5.1	Introduction	86
5.2	Radar Hypothesis Test and CFAR Detectors	86
5.3	Proposed Detectors: The Var-Max-Min Detector and The Max-Min Detector	89
5.4	Simulation Results and Discussions	90
5.5	Conclusions	105

Abstract

In this chapter, new CFAR decision rules "detectors" are proposed for the Weibull, K, and CIG clutter models. These models provide accurate modeling of sea clutter, especially in the tail regions, as shown in chapters 3 and 4. The proposed decision rules are modified to deal with the presence of interfering targets. The proposed detectors are investigated on the basis of synthetic data as well as real IPIX data.

5.1 Introduction

Detection decisions are based on measurements of reflected signals received at the radar and thermal noise already present in the receiver. Samples or measurements may be collected in one or more dimensions, including range, cross-range, angle, and Doppler. Typically, the received signals are sampled at an interval spacing equal to the resolution of the radar system in the dimension in which they are collected. The process of detecting a target begins with comparing a radar measurements with a threshold, measurements exceeding the threshold are associated with returns from a target, and measurements below the threshold are associated with thermal noise or other interference sources including intentional interference (jamming), unintentional interference (electromagnetic interference), clutter, and other sources. The detector threshold is selected to achieve the highest possible P_D for a given SNR and P_{FA} . A false alarm occurs when, in the absence of a target, a source of interference produces a measured value that exceeds the detection threshold. A radar system is designed to achieve and maintain a specified P_{FA} . False alarms deplete radar resources by appearing as valid targets requiring subsequent radar actions and thus degrade system performance. If the interference statistics are known in advance, a threshold can be chosen to achieve a specific P_{FA} . CFAR detectors are designed to track changes in the interference and to adjust the detection threshold to maintain a constant P_{FA} .

5.2 Radar Hypothesis Test and CFAR Detectors

A single echo sample of radar data is composed of either interference alone or interference plus target echoes. For any radar measurement that must be tested for the presence of a target, one of two hypotheses can be assumed true:

1. The measurement is the result of interference only.
2. The measurement is the combined result of interference and echoes from a target.

The first hypothesis is denoted as the null hypothesis, H_0 , and the second as H_1 . For a single echo sample denoted Y . The two PDFs are:

1. $p_{Y|H_0}(y|H_0)$: PDF of Y given that a target is not present.
2. $p_{Y|H_1}(y|H_1)$: PDF of Y given that a target is present.

The design of the detection algorithm and analysis of the resulting radar performance is dependent on developing models for these PDFs for the proposed system and scenario. Moreover, most of the design problems of the radar system are to manipulate these two PDFs to achieve the most favorable detection performance. The detection logic should examine each radar measurement to be tested and choose one of the hypotheses as to the best calculation for that measurement. If H_0 best accounts for the data, then the system declares that a target

is not present at the range, angle, or Doppler coordinates of that measurement. If H_1 best accounts for the data, then the system declares that a target is present. The best procedure to use depends on the definition of “optimal” and the details of the random process models that describe the data. Radar detection algorithms are usually designed according to the NP criterion, a particular optimization strategy. This rule fixes the P_{FA} , that will be allowed by the detection processor and then maximizes the P_D , for a given SNR. Applying the NP criterion to realistic radar detection problems leads to threshold detection using various detection statistics determined by the particular statistics of the data [44]. Figure 5.1 illustrates the threshold detection procedure. Whatever the source of the radar data, a threshold value T is computed, and each data sample is compared with that threshold. If the sample is below the threshold, it is assumed to represent interference only. If it is above the threshold, it is similarly assumed to be too strong to represent interference only, in this case, it must correspond to an interference plus a target of interest, so detection is declared at the range, velocity, or image location represented by that sample.

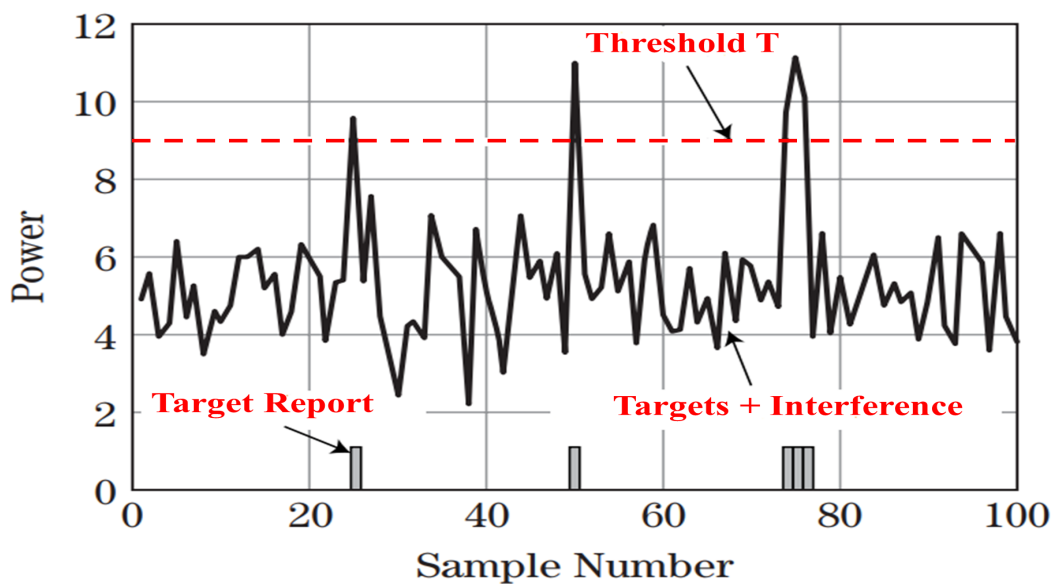


Figure 5.1 – The concept of threshold detection.

It is important to realize that these decisions can be wrong. A strong interference peak can cross the threshold, which leads to a false alarm. Given a good model of the interference, the threshold can be selected to control the P_{FA} . A weak target echo may not add enough power to the interference to cause it to cross the threshold so that the target is not detected, this is called a "miss", and its probability is $1 - P_D$. The P_D and P_{FA} combinations are affected by the quality of the radar system and the design of the signal processor.

The designer of the radar system will generally decide what rate of false alarms can be tolerated based on the implications of acting on a false alarm, this can include overloading an operator monitoring a radar detector screen, using radar resources to start a trace on a non-existent target, or in extreme cases even firing a weapon. Since radar can take tens or even hundreds of detection decisions per second, values of P_{FA} must be quite low to maintain a tolerable false alarm rate. Values in the range of 10^{-4} to 10^{-8} are common, and yet may still lead to false alarms every few seconds or minutes. A desirable property of a detector is an ability to maintain a given P_{FA} in the presence of heterogeneous or changing interference. A detector with this property is called a CFAR detector. All the CFAR detectors proposed in the literature each deal with a problem inherent in the particular conditions of use of the radar, some of them are mentioned below. The first model of the CFAR class is the CA-CFAR detector "Cell Averaging" proposed by Finn and Johnson [45]. This detector evaluates the level of the clutter from the arithmetical mean of the reference cells. In other words, in order to maintain a desired P_{FA} , the estimation of the adaptive threshold is the result of multiplying a constant by the average clutter level. The CA-CFAR exhibits optimum performance in a homogeneous interference environment. However, in reality, due to the presence of a clutter edge and/or interfering targets in the reference window, the clutter is often heterogeneous. As a result, the performance and false alarm rate regulation capabilities of the CA-CFAR detector are significantly affected. If a clutter edge is present, the Cell Under Test (CUT) may be found submerged in an area where the clutter power is higher than where some reference cells are located. In this case, in order to minimize the capture effect while maintaining an almost P_{FA} . Hansen and Sawyers proposed the GO-CFAR "Greatest-Of" detector [46]. In this type, the estimate of the level of clutter is given by the maximum of the arithmetic means obtained from the cells belonging to the two reference half-windows, located on either side of the CUT. Weiss, showed that the GO-CFAR detector is very vulnerable to the presence of one or more interfering targets in the reference window [47]. In the presence of interfering targets, cases of targets that are closely distant from each other may be encountered in target-dense environments. In such situations, automatic detectors declare the presence of a single target. To improve the resolution of close targets and therefore improve detection performance, Trunk proposed the SO-CFAR "Smallest-Of" detector [48], the clutter level is estimated as in the GO-CFAR but with the minimum averages of adjacent cells. Its detection performance is significantly degraded if the interfering targets are located in the two half-windows references. In addition, in the presence of a clutter edge, the SO-CFAR detector has difficulty in maintaining a CFAR. Some of the more common CFARs detectors include Trimmed Mean (TM) [49] or Censored (CS) CFAR [50], Order Statistics (OS) CFAR [51] and more, each dealing with a problem inherent to the specific conditions of use of the radar.

5.3 Proposed Detectors: The Var-Max-Min Detector and The Max-Min Detector

The two proposed detectors shown in Figure 5.2 are designed to be CFAR and able to provide a high P_D in the case of the presence of thermal noise and interfering targets. The content of each cell is obtained by sampling the signal received at the output of the square law envelope detector. The obtained samples are stored in a shift register and the detection test in each cell uses a reference window of N cells adjacent to the CUT which provide a local estimate of the clutter level. The sliding of this window along the register of cells makes it possible to cover the entire radar range. Since it is mathematically difficult to prove the CFARness of the proposed thresholds, the latter were found using the trial and error method, and the choice of the number of reference cells for both detectors were found after intensive testing for several values from 2 to 32 cells. The best performances in terms of false alarm regulation of the suggested detectors are obtained for a number equal to 2, which is useful regarding the calculation time and the stationarity of clutter.

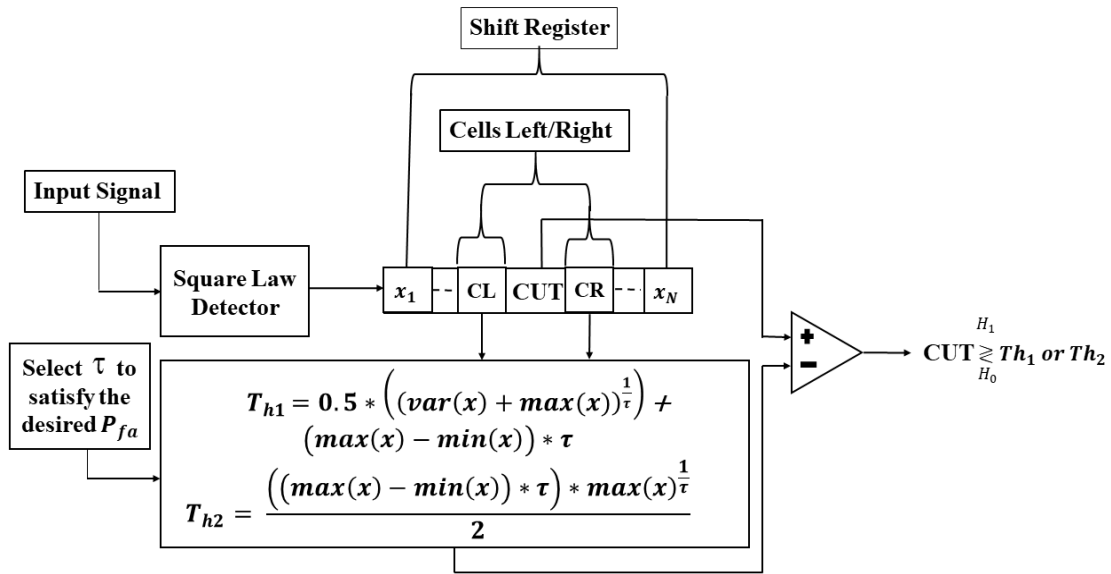


Figure 5.2 – Block diagram of the two proposed detectors.

The principle of our detectors is based on binary decision-making to choose between the presence or the absence of the target of interest, as explained above. Monte Carlo simulations are performed to investigate the suggested decision rules for the Weibull, K, and CIG sea clutter models with the consideration of the presence of thermal noise. The decision rules corresponding to the Var-Max-Min detector and the Max-Min detector are based on miscellaneous statistics, the variance, the maximum and the minimum value of the reference cells.

The threshold of the Var-Max-Min detector is given by:

$$T_{h1} = 0.5 * \left((\text{var}(x) + \max(x))^{\frac{1}{\tau}} \right) + (\max(x) - \min(x)) * \tau. \quad (5.1)$$

The threshold of the Max-Min detector is given by:

$$T_{h2} = \frac{((\max(x) - \min(x)) * \tau) * \max(x)^{\frac{1}{\tau}}}{2}. \quad (5.2)$$

5.4 Simulation Results and Discussions

First, we analyze the P_{FA} performance of the two decision rules using synthetic data plus thermal noise. Then, we study the robustness of P_{FA} regulation in the case of the presence of thermal noise and two interfering targets "Swirling I" in the reference cells. Next, we show the P_D for each clutter model. Finally, we investigate the performance of the proposed detectors using a real IPIX sea data.

5.4.1 False Alarm Regulation

In this subsection, we show the variations of P_{FA} versus the threshold factor τ for each model. To undertake these simulations, we use the MATLAB tool and the following assumptions: Non-coherent detector, the variations of P_{FA} from 0 to 10^{-4} with representation in logarithmic base 10, different values of shape and scale parameters, the number of independent Monte Carlo runs is set to 10^7 and the thermal noise power $p_n = 2\sigma^2$ is set to 2 dB. For the Max-Min detector, Figure 5.3 shows the variation of P_{FA} from values close to 0 to -4 versus the threshold factor τ for the Weibull distribution clutter with different values of shape and scale parameters. We observe that all curves overlap with each other without any deviations even when the clutter becomes spiky $c \geq 0.5$. The same pattern is observed in Figure 5.4 for K with $v \geq 0.01$ and CIG distribution with $\lambda \geq 0.1$ in Figure 5.5. The three tests prove that the Max-Min detector attain the CFAR property independently of the shape and scale parameters. We also note from the three experiments that the presence of thermal noise does not affect the robustness of the proposed first detector.

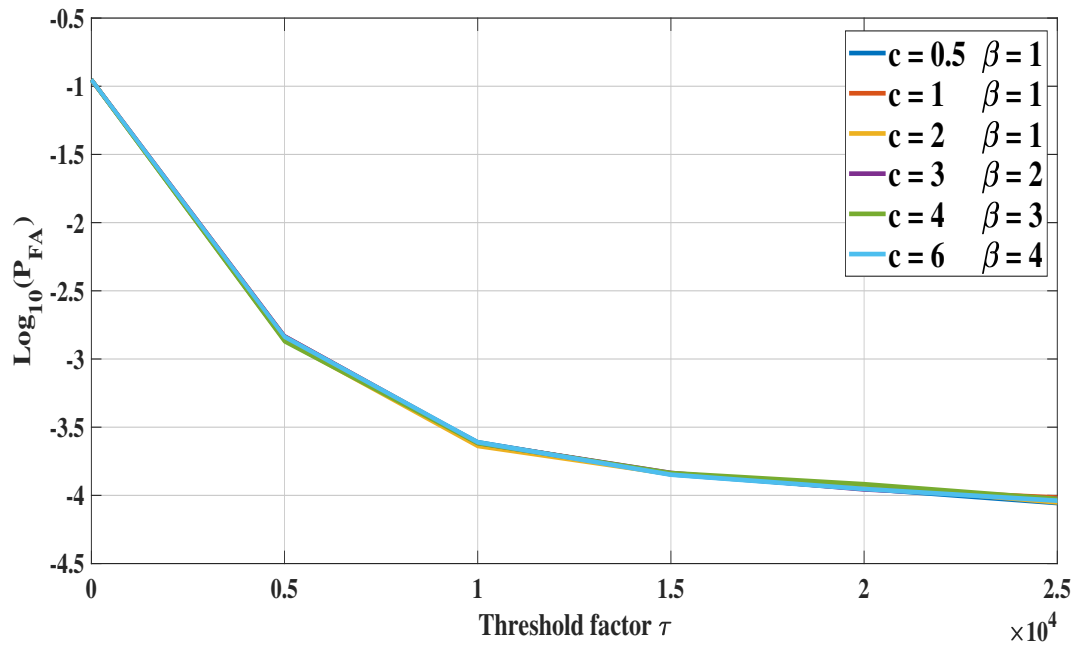


Figure 5.3 – Variation of P_{FA} of the Max-Min detector versus the threshold factor τ using the Weibull distribution.

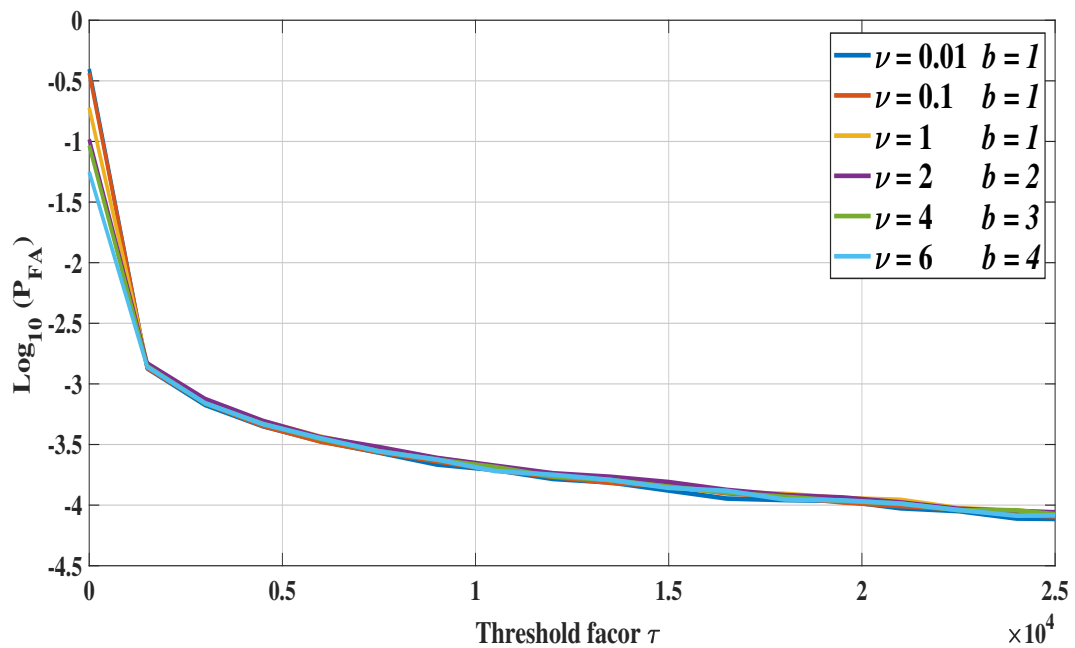


Figure 5.4 – Variation of P_{FA} of the Max-Min detector versus the threshold factor τ using the K distribution.

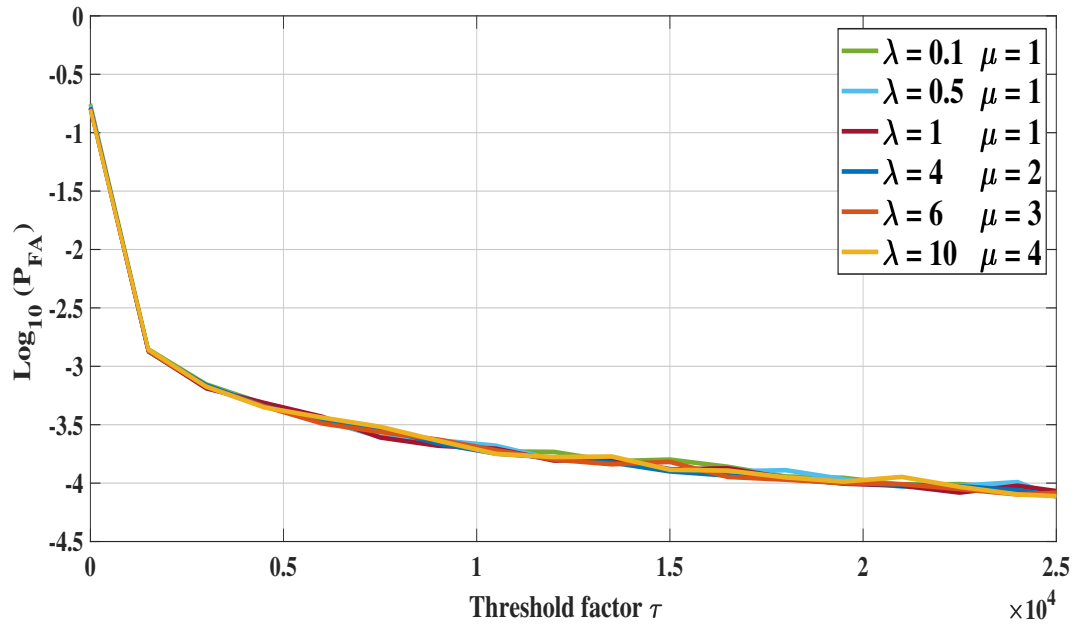


Figure 5.5 – Variation of P_{FA} of the Max-Min detector versus the threshold factor τ using the CIG distribution.

On the other hand, we repeated the same tests with the same parameters for the Var-Max-Min detector. We show the variations of P_{FA} against the threshold factor τ for the three clutter models in Figures 5.6, 5.7, and 5.8. It is clear from the three experiments that all the curves almost coincide with each other. This means that the Var-Max-Min detector keeps the CFAR property for the three models with $c \geq 0.5$, $\nu \geq 1$ and $\lambda \geq 0.1$. Also, the thermal noise does not affect the false alarm regulation.

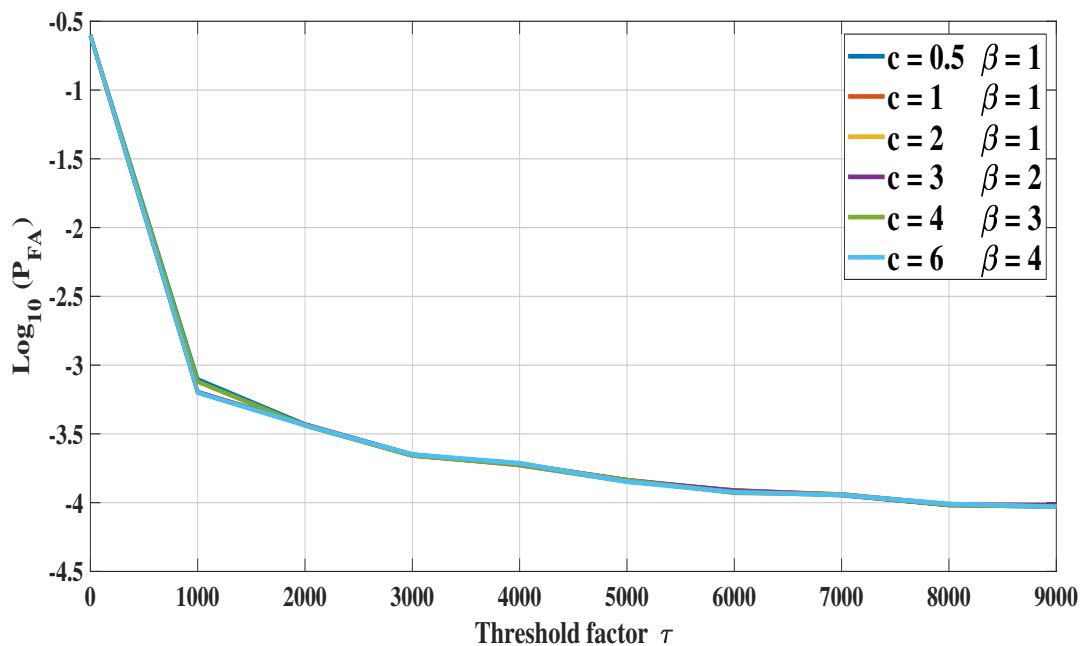


Figure 5.6 – Variation of P_{FA} of the Var-Max-Min detector versus the threshold factor τ using the Weibull distribution.

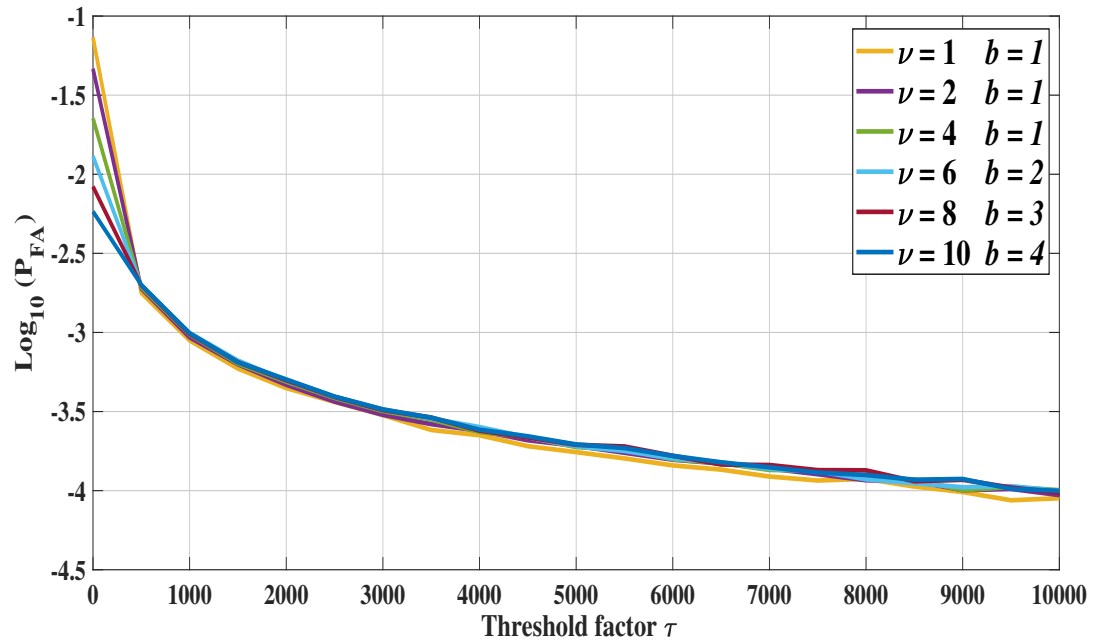


Figure 5.7 – Variation of P_{FA} of the Var-Max-Min detector versus the threshold factor τ using the K distribution.

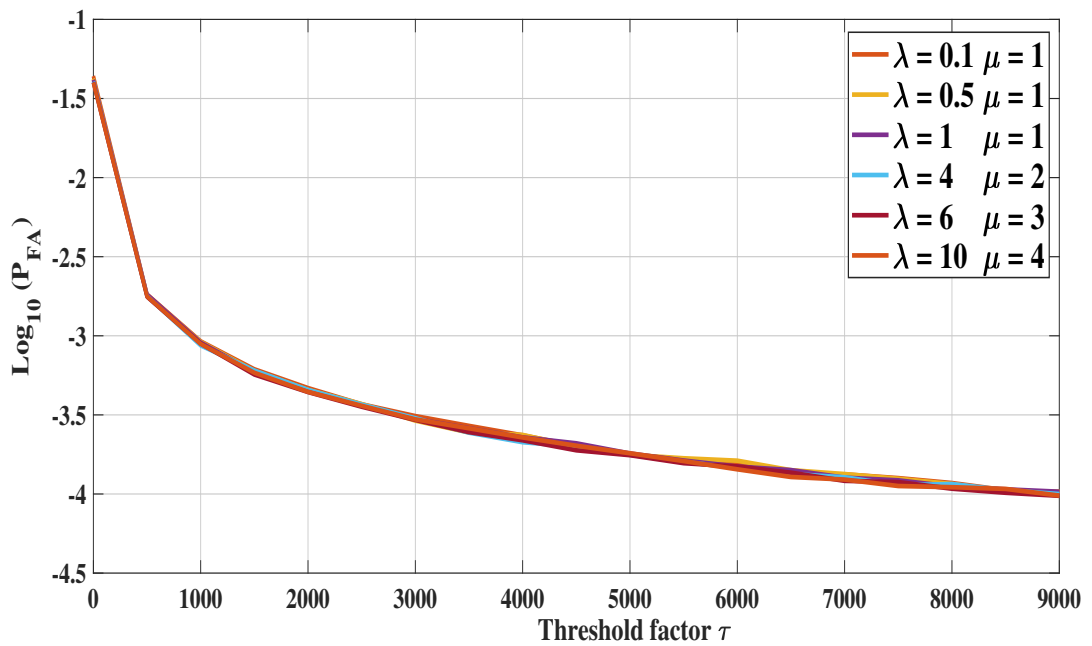


Figure 5.8 – Variation of P_{FA} of the Var-Max-Min detector versus the threshold factor τ using the CIG distribution.

5.4.2 False Alarm Regulation in the Presence of Two Interfering Targets

In this subsection, we study the effect of the presence of two interfering targets in the reference window on the proposed detectors performance. To test the robustness of the proposed detectors in the case of the presence of one or more interfering targets in the reference window, we modified the first version of the suggested detectors to deal with the presence of interfering targets. Each detector uses four reference cells instead of two, then these cells are arranged in an ascending order to acquire $X_{(1):(4)}$, then the two largest samples are censored, which means that these detectors can handle up to two interfering targets. Each threshold is calculated using the other two samples in the same manner as in (5.1) and (5.2). To perform this work, we use the same assumptions mentioned above, considering that the interfering targets are supposed to fluctuate according to the Swerling I model and the Interference-to-Clutter Ratio (ICR) is assumed to be equal to 20 dB. For the Weibull distribution Figure 5.9 shows the changes of P_{FA} against the threshold factor τ , it is clear that almost all curves overlap, which means that the CFAR property is preserved. For K and CIG distributions, the detector also keeps the CFAR characteristic as shown Figures 5.10 and 5.11 respectively.

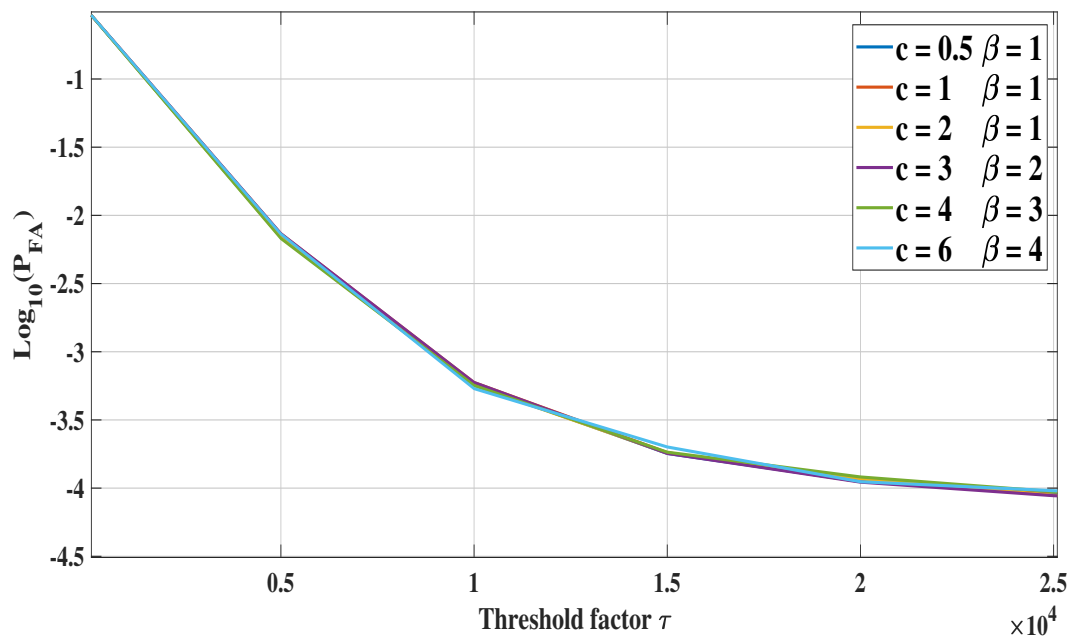


Figure 5.9 – Variation of P_{FA} of the Max-Min detector versus the threshold factor τ using the Weibull distribution plus two interfering targets.

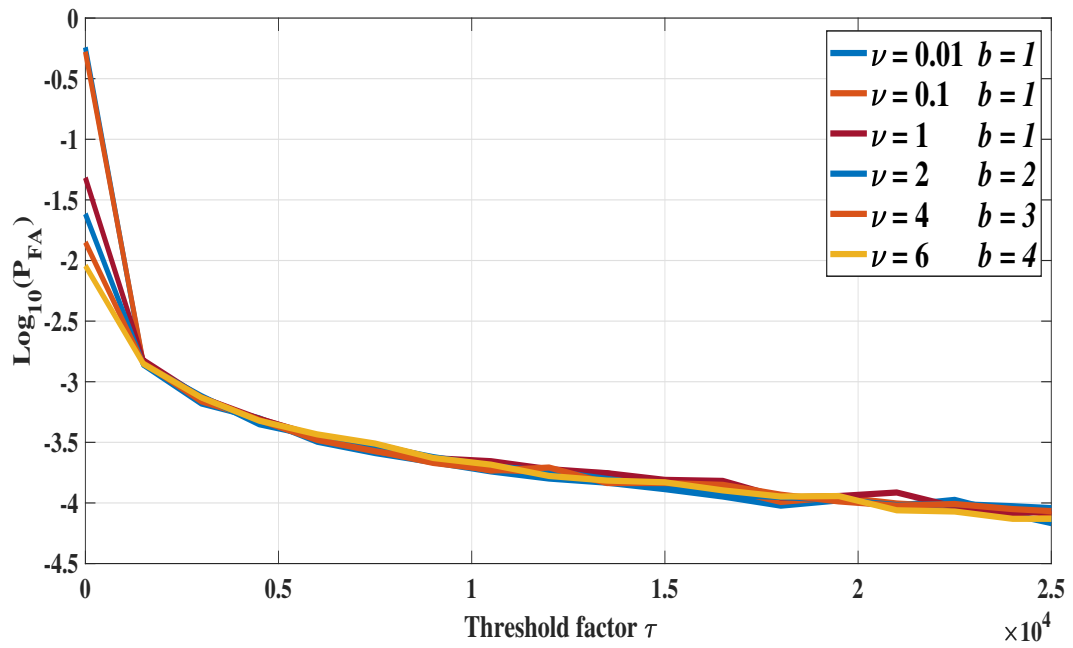


Figure 5.10 – Variation of P_{FA} of the Max-Min detector versus the threshold factor τ using the K distribution plus two interfering targets.

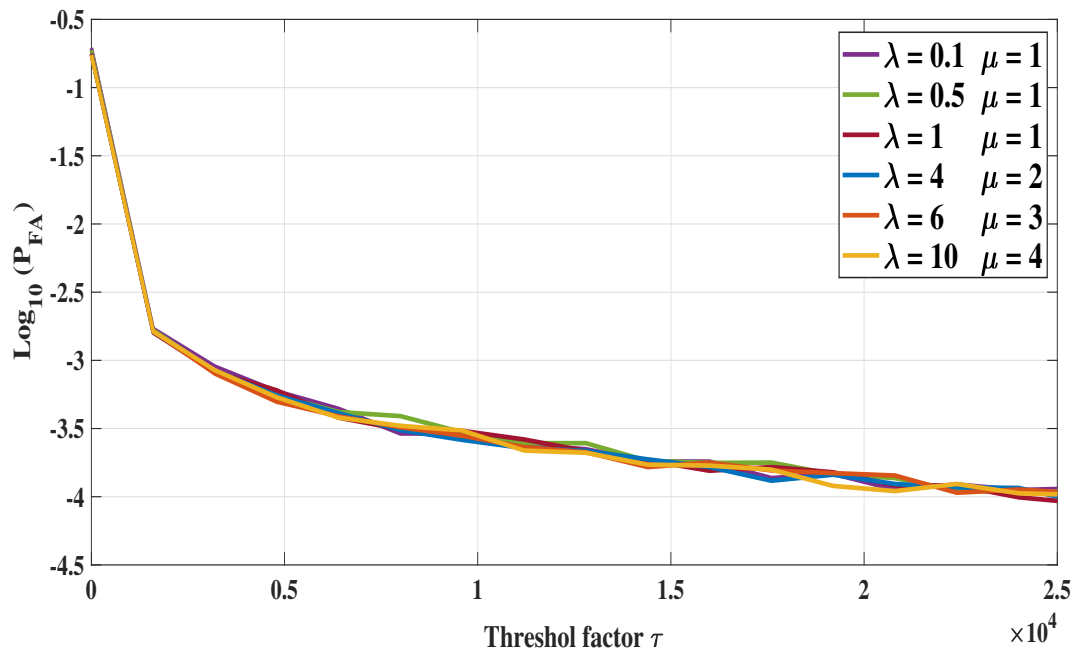


Figure 5.11 – Variation of P_{FA} of the Max-Min detector versus the threshold factor τ using the CIG distribution plus two interfering targets.

We repeat the same simulations with the same parameters for the Var-Max-Min detector. The same patterns are observed for the three distributions where all the curves almost match each other. From the obtained results, the proposed detectors regulate the P_{FA} in an acceptable manner which means that the presence of interference targets in the reference window does not affect the robustness of the proposed detectors.

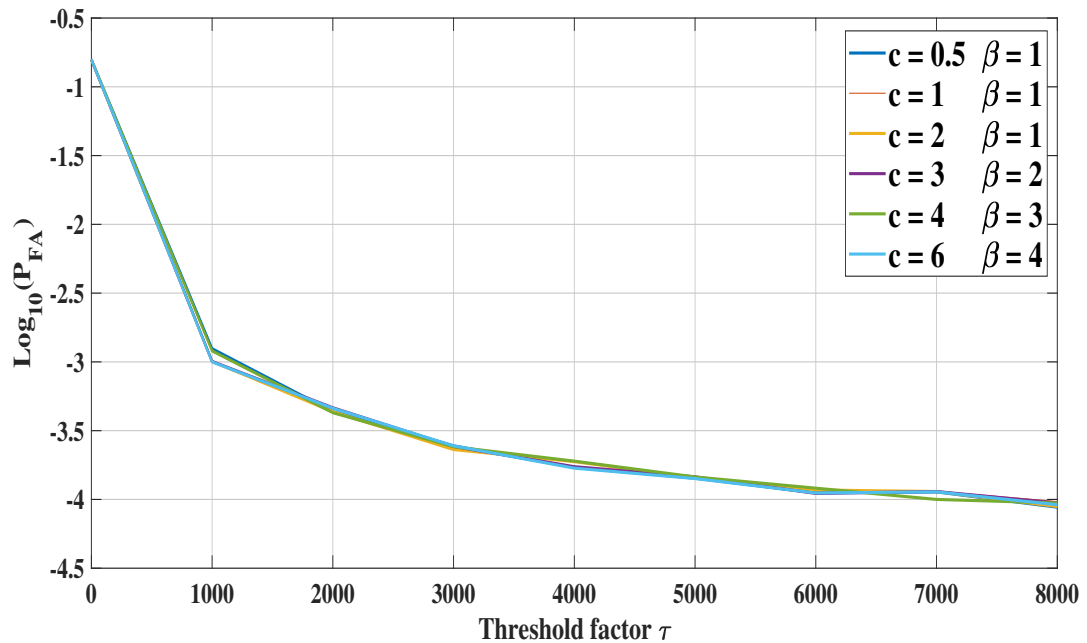


Figure 5.12 – Variation of P_{FA} of the Var-Max-Min detector versus the threshold factor τ using the Weibull distribution plus two interfering targets.

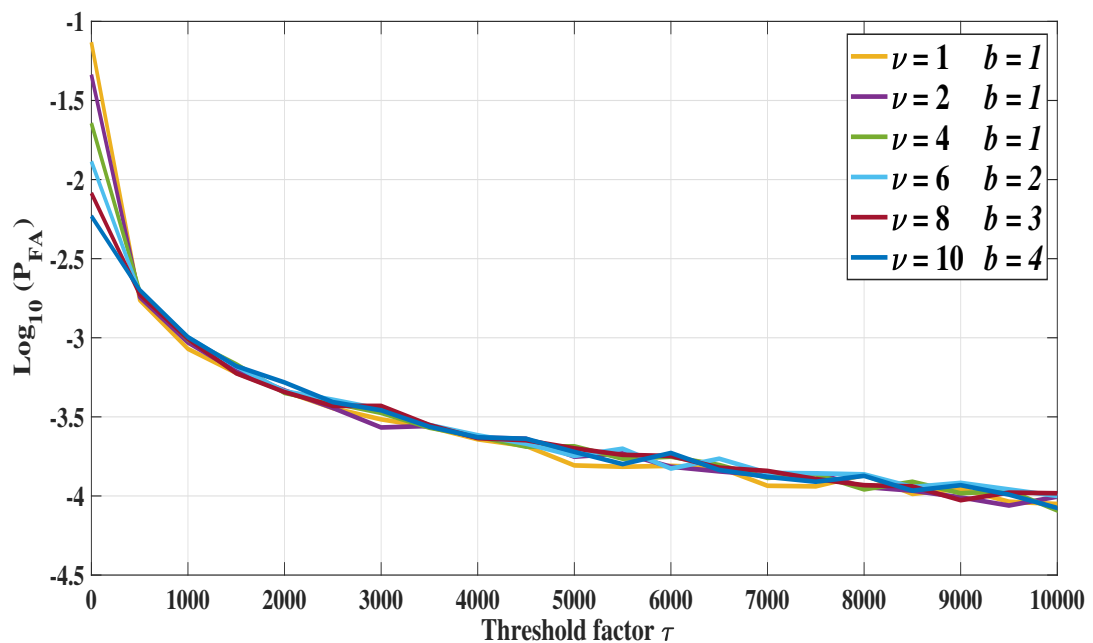


Figure 5.13 – Variation of P_{FA} of the the Var-Max-Min detector versus the threshold factor τ using the K distribution plus two interfering targets.

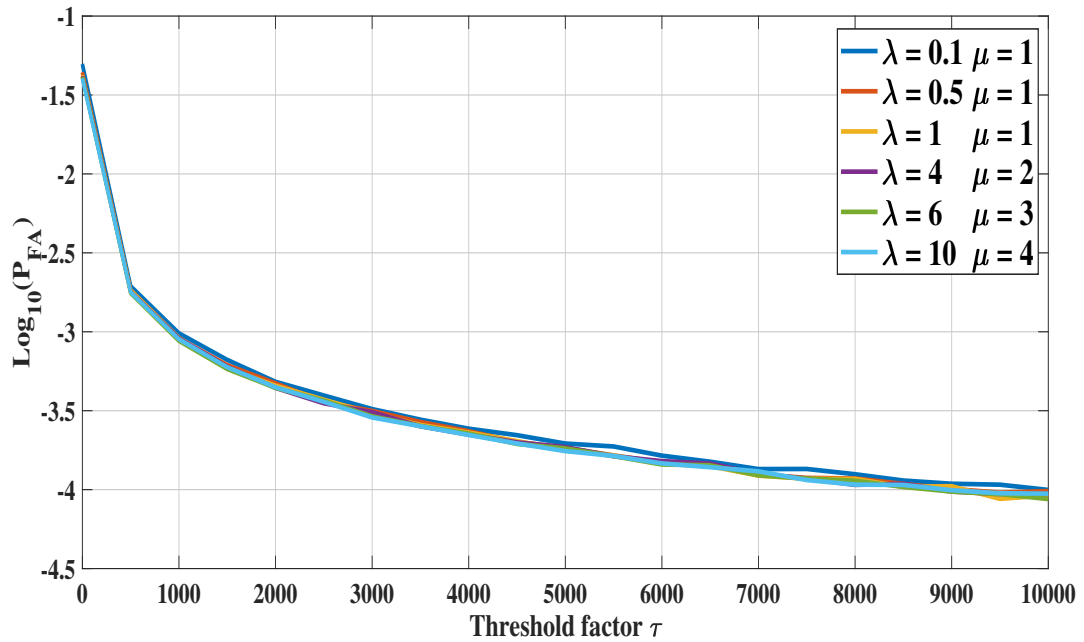


Figure 5.14 – Variation of P_{FA} of the Var-Max-Min detector versus the threshold factor τ using the CIG distribution plus two interfering.

5.4.3 Probability of Detection

In this subsection, we illustrate the probability of detection of the proposed detectors for the three clutter models mentioned above. Figure 5.15 shows P_D versus the SCR for the Weibull clutter model, which starts from small values of the shape parameter, $c \geq 0.5$. We observe that the detection curves are superimposed and indicate that increasing the shape parameter leads to an increase in detection. According to the design of the proposed detector, which is based only on two reference cells when estimating the level of clutter, the Max-Min detector provides a high detection performance. In Figures 5.16 and 5.17, we repeat the same simulations for the K and CIG clutter models, the same performance of detection is observed even for the case of spiky clutter.

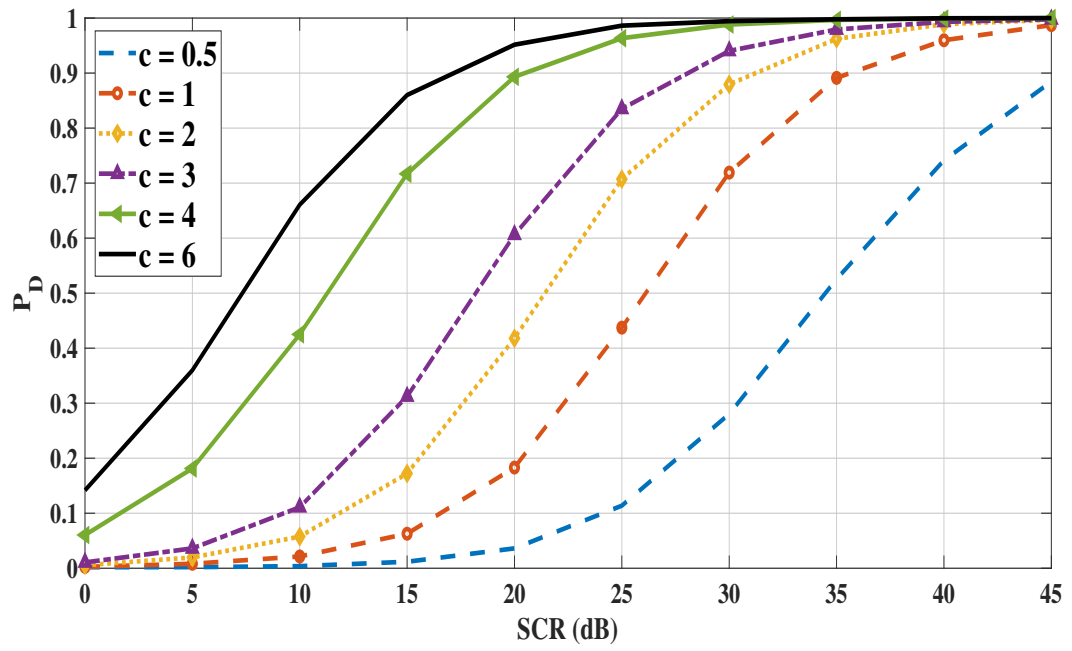


Figure 5.15 – P_D of the Max-Min detector versus the SCR using the Weibull distribution.

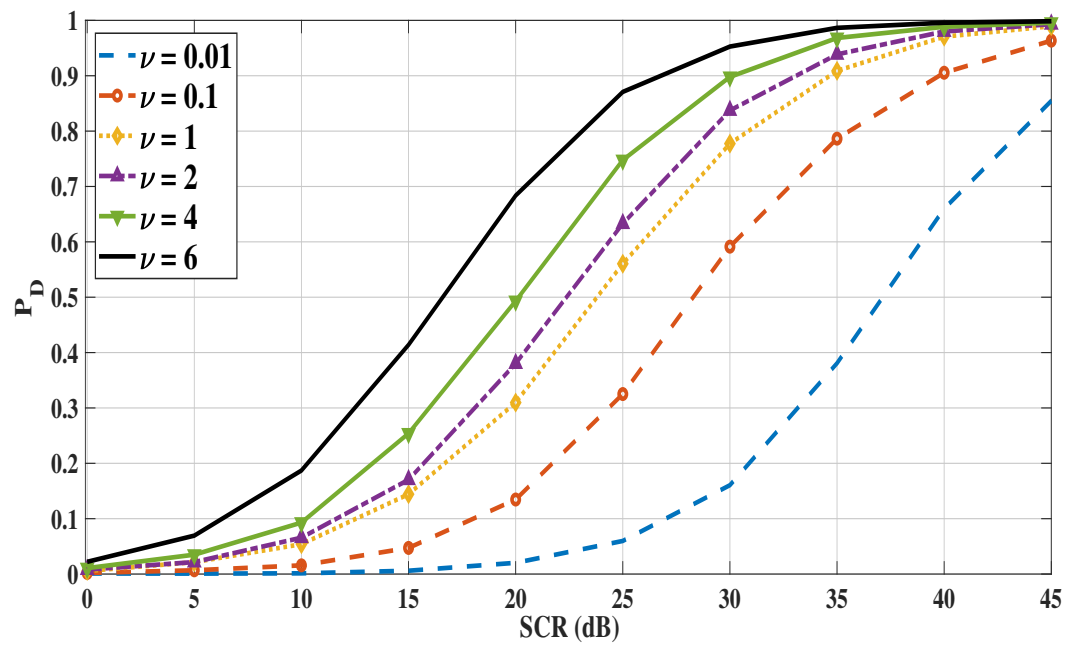


Figure 5.16 – P_D of the Max-Min detector versus the SCR using the K distribution.

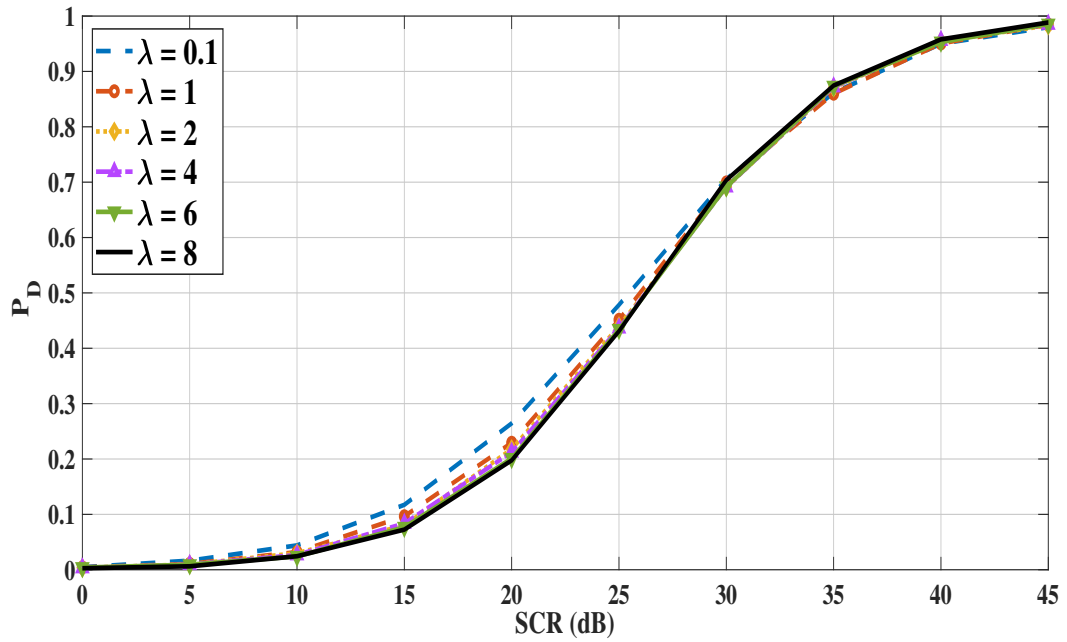


Figure 5.17 – P_D of the Max-Min detector versus the SCR using the CIG distribution.

We repeat the same simulations with the same parameters for the Var-Max-Min detector. Figures 5.18, 5.19, and 5.20 show the variations of P_D versus SCR for the three clutter models with different shape parameter values. From the obtained curves, it is clear that the Var-Max-Min detector also provides a high probability of detection.

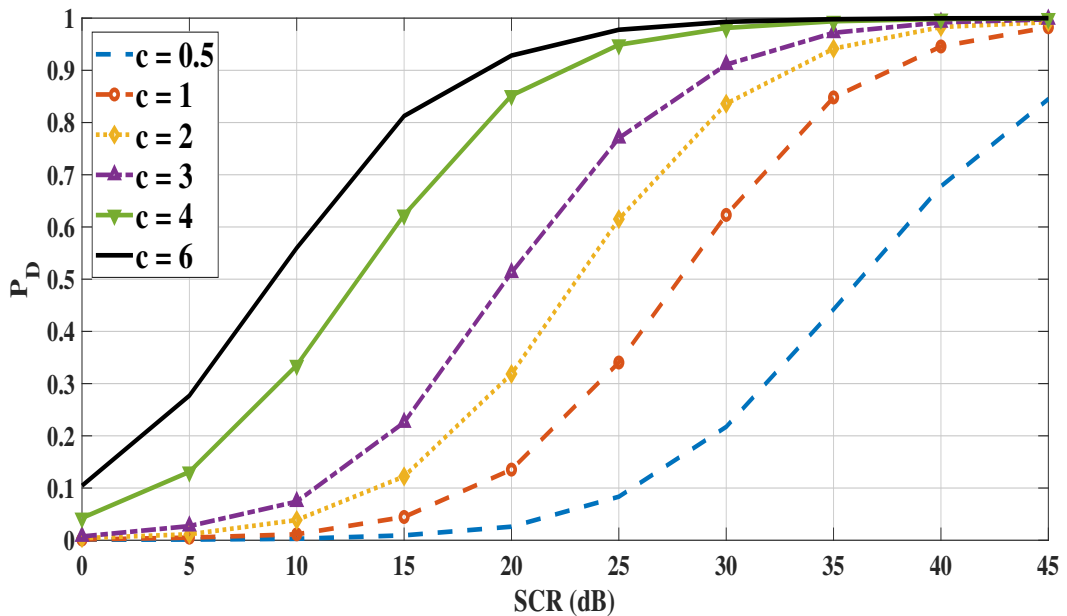


Figure 5.18 – P_D of the Var-Max-Min detector versus the SCR using the Weibull distribution.

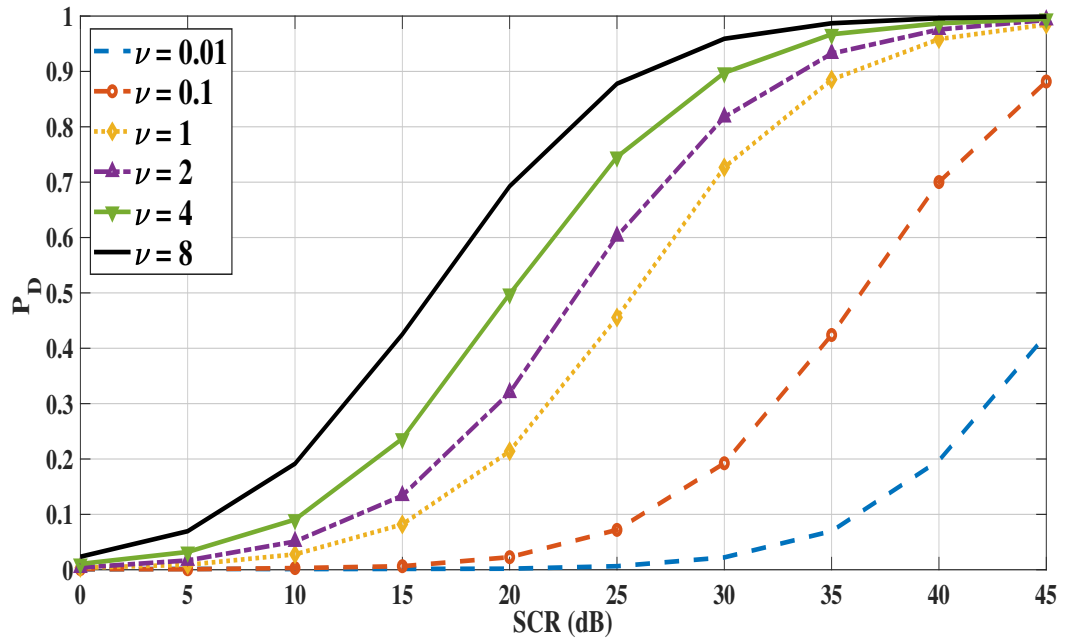


Figure 5.19 – P_D of the Var-Max-Min detector versus the SCR using the K distribution.

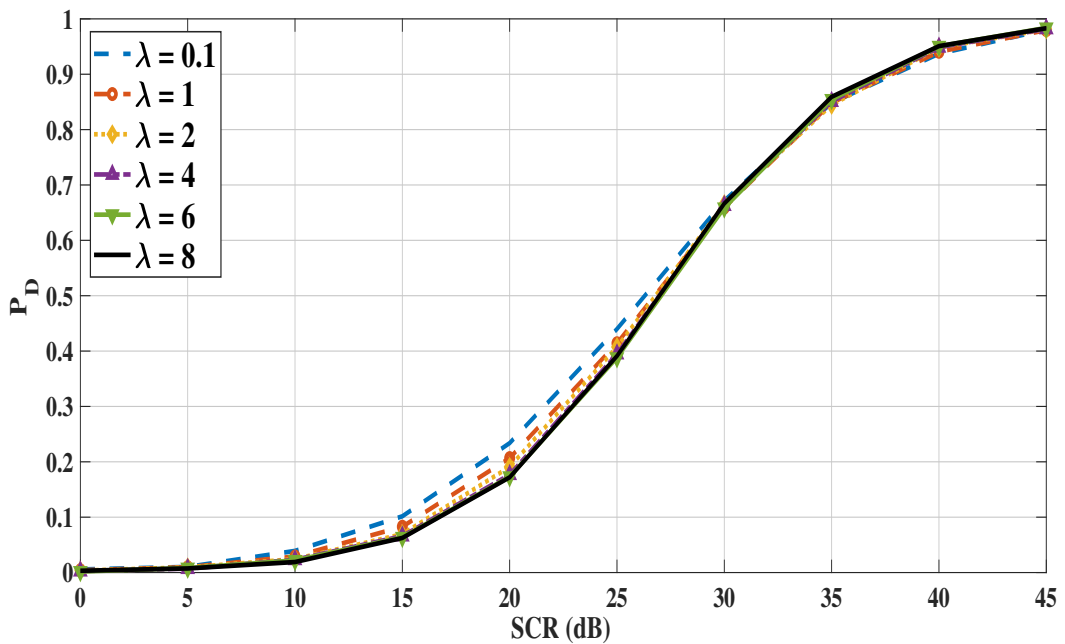


Figure 5.20 – P_D of the Var-Max-Min detector versus the SCR using the CIG distribution.

To show which detector offers the highest probability of detection performance in the case of the presence of spiky clutter, we compare P_D for the three clutter models mentioned above with different small values of the shape parameters. For the Weibull clutter model, we observe in Figure 5.21 that the Max-Min detector performs better than the Var-Max-Min detector for the three values of the shape parameter, which provides the highest probability of detection, in particular between values 10 and 40 dB.

The same results were obtained for the K and CIG clutter models, where the Max-Min detector offers the highest P_D than the Var-Max-Min detector, as shown in Figures 5.22 and 5.23, respectively.

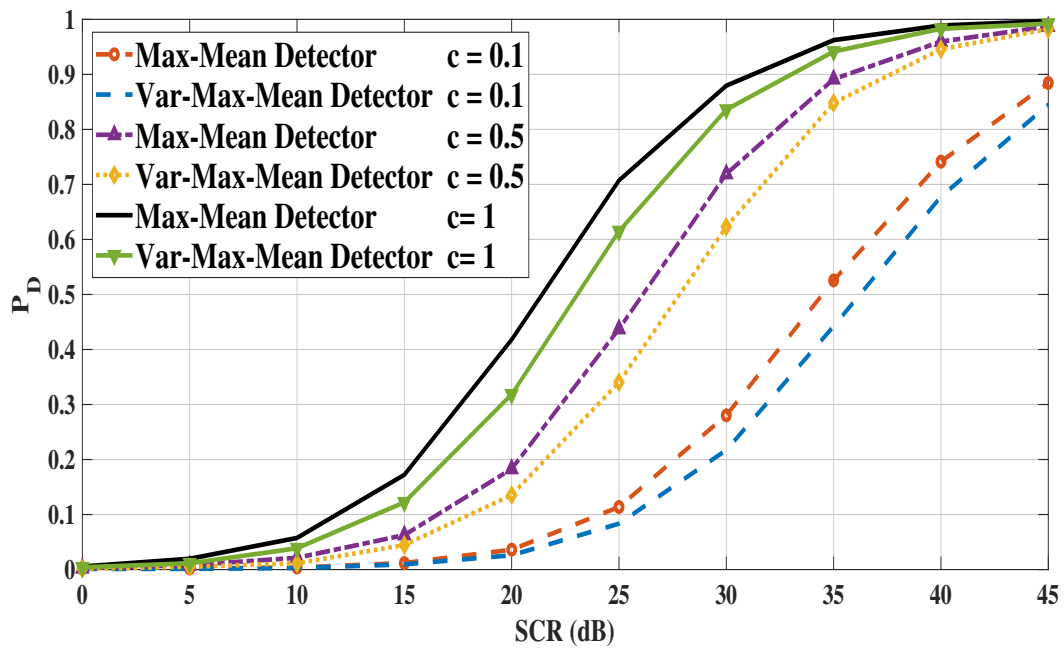


Figure 5.21 – Comparison of P_D between the two detectors using the Weibull distribution.

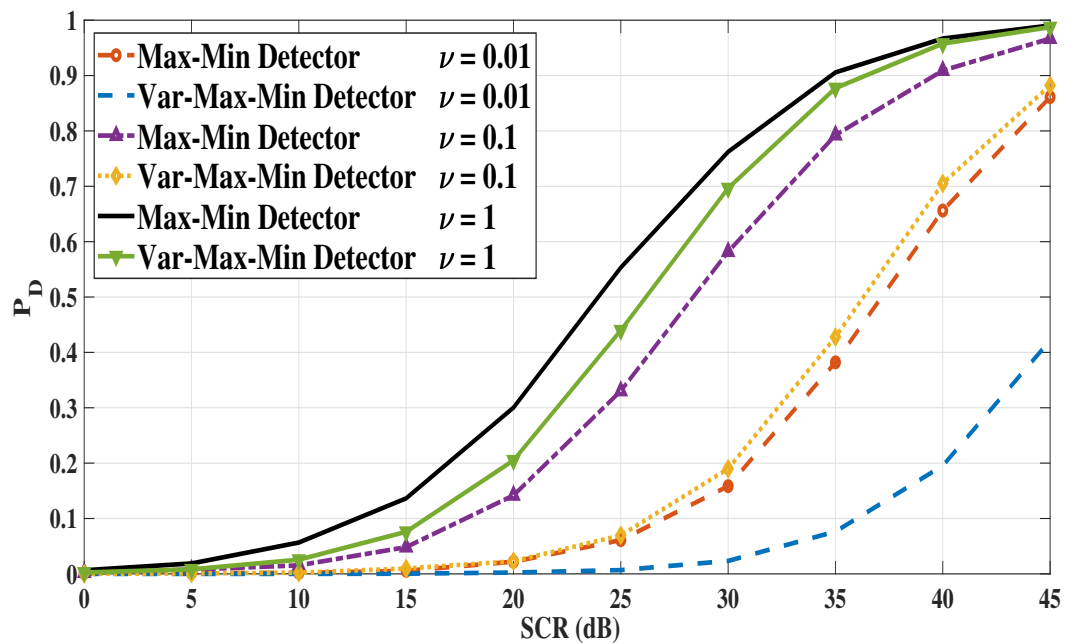


Figure 5.22 – Comparison of P_D between the two detectors using the K distribution.

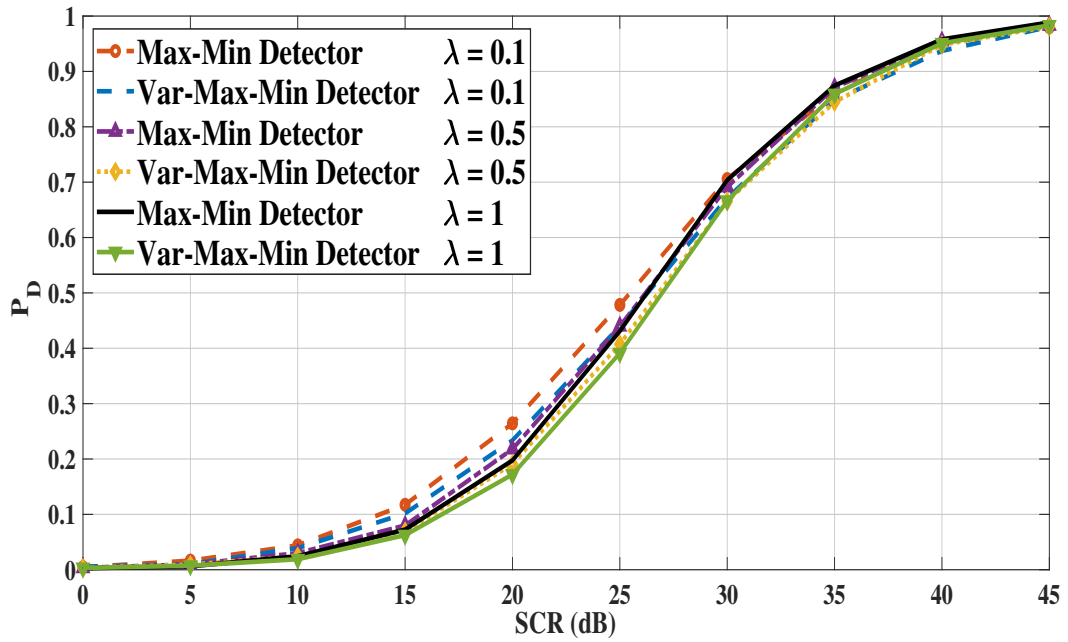


Figure 5.23 – Comparison of P_D between the two detectors using the CIG distribution.

5.4.4 Experimental Results Using Real Sea IPIX Data

To evaluate the performance of the proposed detectors with real IPIX sea data, we used three files mentioned in chapter 3, (19980204_194537_ANTSTEP), (19980204_221700_ANTSTEP), and (19980205_185111_ANTSTEP) for 30, 15, and 3m respectively, with different types of polarization modes. Figures 5.24 and 5.25 depict the variations of P_{FA} from 0 to 10^{-3} for the three resolutions with four polarization modes HH, VV, HV, and VH. We note that almost all curves overlap without any deviations. The experimental variations of P_{FA} of the actual IPIX data are similar to the theoretical variations obtained from the Weibull and the CG clutter models in the case of the presence of thermal noise and interfering targets, with almost the same threshold factor to obtain the desired P_{FA} . This means that both detectors maintain the CFAR property successfully. Finally, for P_D , Figures 5.26 and 5.27 show the detection curves for each resolution. As expected, all detection curves attain 1 for an SCR around 45 dB. This means that the proposed detectors maintain the same detection performance for experimental data successfully.

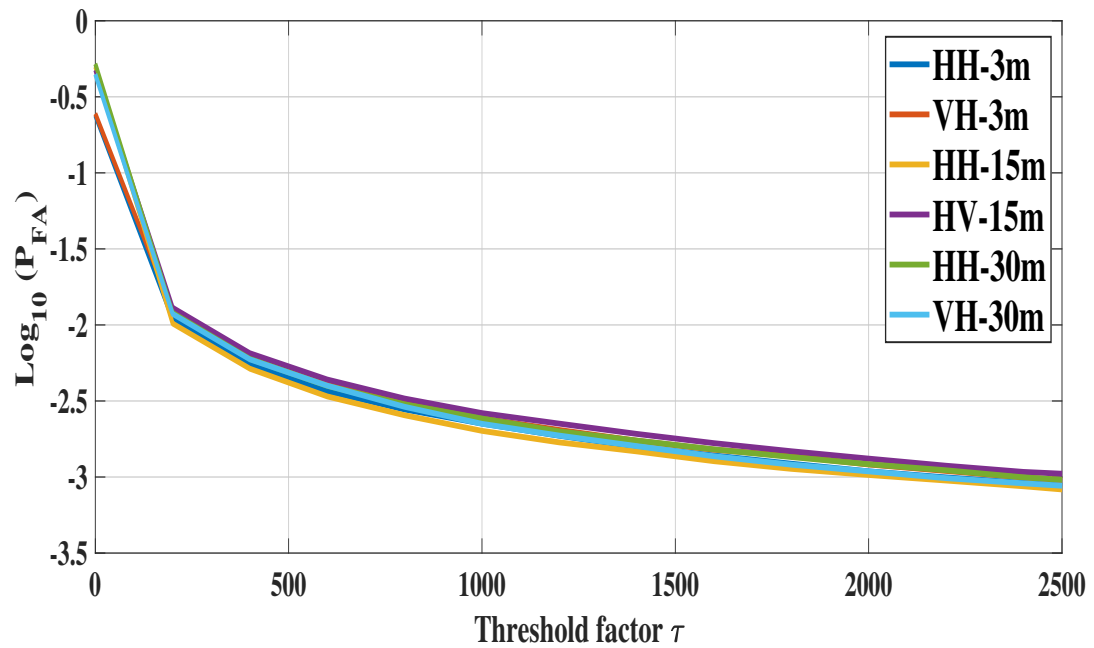


Figure 5.24 – Variation of P_{FA} of the Max-Min detector versus the threshold factor τ using the actual sea data IPIX.

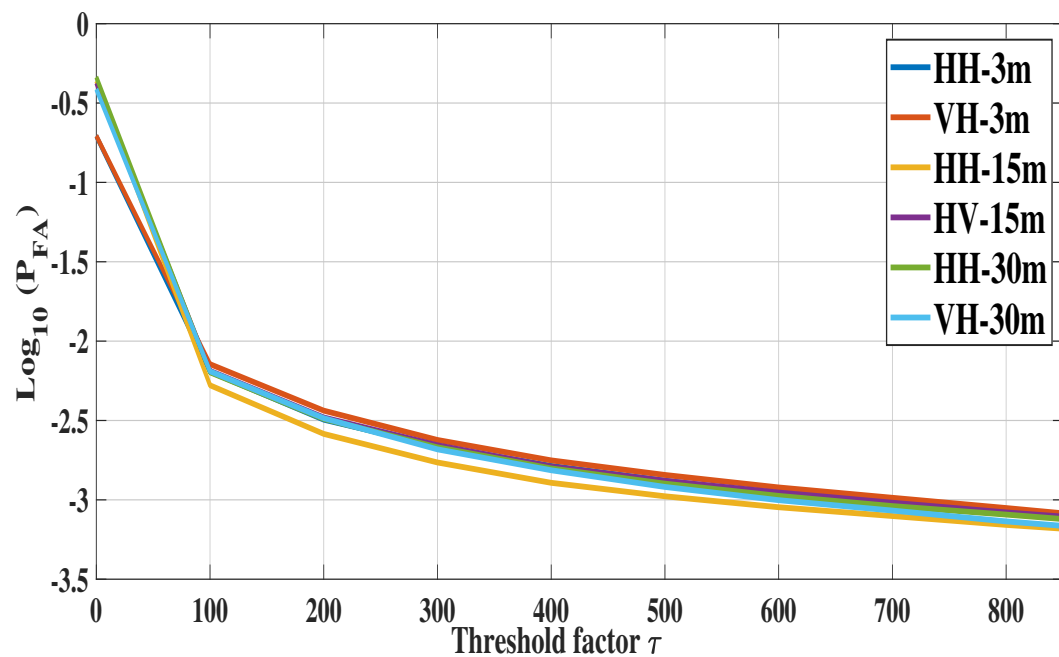


Figure 5.25 – Variation of P_{FA} of the Var-Max-Min detector versus the threshold factor τ using the actual sea data IPIX.

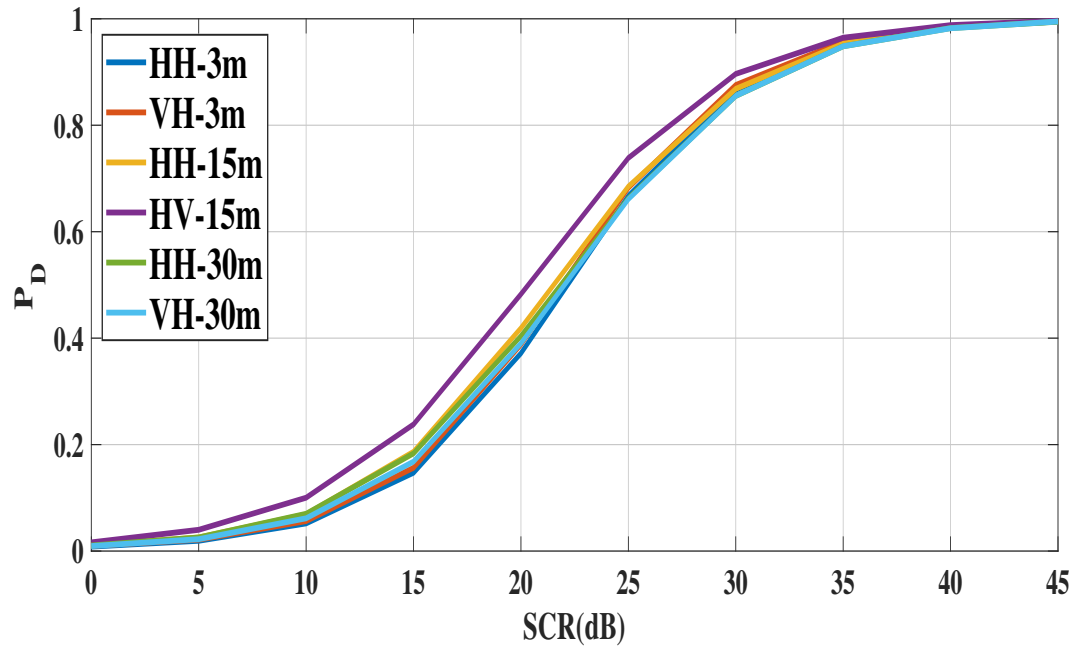


Figure 5.26 – P_D of the Max-Min detector versus the SCR using the actual sea data IPIX.

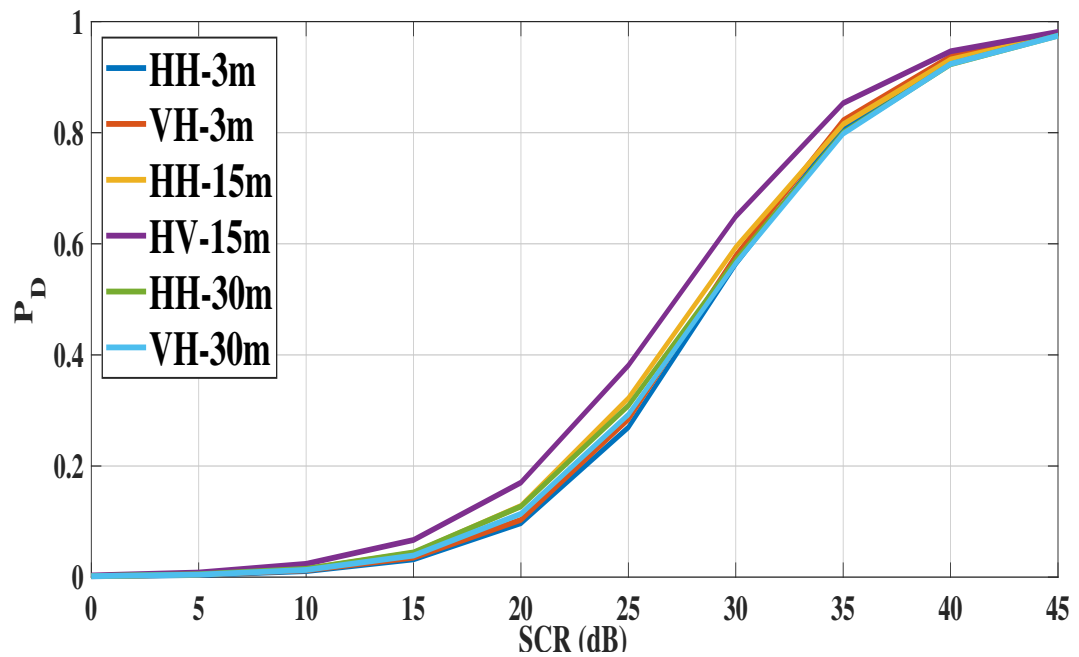


Figure 5.27 – P_D of the Var-Max-Min detector versus the SCR using the actual sea data IPIX.

5.5 Conclusions

In this chapter, we have proposed two new CFAR detectors operating in sea clutter modeled by Weibull, K, and CIG distributions. We have assumed the presence of thermal noise and interfering targets. The two detectors employ two reference cells to set up the detection threshold. The robustness of the proposed detectors is illustrated through numerical simulations performed on the Weibull and the CG models as well on actual IPIX radar data. In the case of the presence of the thermal noise, both detectors maintain a good performance in terms of false alarm regulation. We have also tested these detectors in the case where two interfering targets are present by modifying the detection algorithm and they proved to be robust. To validate these two detectors, we applied real data from the IPIX database and the results are similar to those obtained by synthetic data. Finally, it is worth pointing out that since the decision operation uses only two reference cells, these detectors are appropriate for real time applications.

Chapter 6

General Conclusions

Contents

6.1 Summary and Main Results	107
6.2 Perspectives and Future Work	108

Abstract

In this final chapter, we first briefly recall the main work of this thesis, then we discuss our contributions including the main results. Finally, we list the possible perspectives and suggestions that can serve as extensions to this research work.

6.1 Summary and Main Results

Sea clutter modeling is the critical step to design or develop a maritime radar so that it can detect with high accuracy the small targets and adjust the false alarm rates at any time and under all adverse weather conditions. This thesis is in the same context.

- Firstly, Two approximate models of Weibull plus additive thermal noise have been proposed for high-resolution sea clutter consisting of a compound distribution with speckle and a texture following a Weibull distribution. For the first Weibull model, we derived the expressions of the PDF and CCDF for single and multiple pulses. For the second model, we also derived the expression of the CCDF for single as well as multiple pulses and we provided the expression of the moments. In order to be able to estimate the parameters of the proposed models, we used the N-M algorithm. The simulations were carried out on the bases of synthesized sea data as well as on real sea data collected by the McMaster IPIX radar for multiple operating scenarios, different resolution range (60, 30, 15, 9, and 3m) and different polarization mode (HH, VV, HV, and VH mode). By plotting their PDFs and CCDFs, the proposed models showed an accurate fit to synthesized data as well as to real sea IPIX data with the best approximation in the tail region, outperforming CG models in most cases. According to all the cases studied and all the results obtained, the two proposed Weibull models are good candidates for modeling high-resolution sea clutter data.
- Then, high-resolution sea clutter modeling using a mixture of two approximate Weibull models was studied and discussed. Also, all the results showed that the mixture of Weibull plus noise models provides the best fit to real sea data, outperforming the mixture of CG plus noise models in all the cases studied.
- Finally, in the context of non-coherent detection, two new CFAR detectors are suggested for Weibull, K and CIG models with thermal noise and interfering targets. The two detectors use two reference cells to set up the detection threshold. The proposed detectors are investigated on the basis of synthetic sea data as well as real sea data of the IPIX radar database. All the obtained results exhibit a high probability of detection as well as an excellent false alarm rate regulation especially for spiky clutter.

6.2 Perspectives and Future Work

In light of the various results obtained during this thesis, different research perspectives can be considered. The axes that should be considered as perspectives for future work can be summarized as follows:

- Use the proposed Weibull models to detect targets with a constant false alarm rate (CFAR) in homogeneous and heterogeneous environments.
- Derivation of the mathematical functions of proposed Weibull models to obtain a closed-form without integration.
- It is important to find the best estimator for the proposed Weibull models such as the MLE estimator and the zlogz estimator.

Finally, as the current trend for modern radars is much more like generalized clutter models, we hope that this work has given an added value in the field of high-resolution sea clutter radar modeling.

Bibliography

- [1] C. Wolff, “Radar basics,” Radartutorial. [Online]. Available: <https://www.radartutorial.eu/index.en.html>. [Accessed: 28-Nov-2021].
- [2] M. I. Skolnik, “Radar Handbook,” New York: McGraw-Hill, 2008.
- [3] M. A. Richards, J. A. Scheer, W. A. Holm, and W. L. Melvin, “Principles of modern radar,” Raleigh: Scitech Publishing, 2010.
- [4] H. Rahman, “Fundamental principles of radar,” Boca Raton: CRC Press, 2019.
- [5] K. S. Chen, “Principles of synthetic aperture radar imaging: a system simulation approach,” Boca Raton: CRC Press/Taylor & Francis Group, 2019.
- [6] J. Bech and J. L. Chau, “Doppler radar observations: weather radar, wind Profiler, ionospheric radar, and other advanced applications,” Rijeka: InTech, 2012.
- [7] K. D. Ward, R. J. A. Tough, and S. Watts, “Sea clutter: scattering, the K distribution and radar performance,” Stevenage, Herts, United Kingdom: Institution of Engineering and Technology, 2013.
- [8] G. V. Trunk and S. F. George, “Detection of targets in non-Gaussian sea clutter,” *IEEE Transactions on Aerospace and Electronic Systems*, vol. AES-6, no. 5, pp. 620–628, 1970.
- [9] D. Schleher, “Radar detection in Weibull clutter,” *IEEE Transactions on Aerospace and Electronic Systems*, vol. AES-12, no. 6, pp. 736–743, 1976.
- [10] E. Jakeman and P. Pusey, “A model for non-Rayleigh sea echo,” *IEEE Transactions on Antennas and Propagation*, vol. 24, no. 6, pp. 806–814, 1976.
- [11] K. D. Ward, C. J. Baker, and S. Watts, “Maritime surveillance radar. part 1: Radar scattering from the ocean surface,” *IEE Proceedings F Radar and Signal Processing*, vol. 137, no. 2, p. 51, 1990.
- [12] C. Oliver and S. Quegan, *Understanding synthetic aperture radar images*. Boston, MA: Artech House, Inc., 1998.
- [13] E. Jakeman and R. J. A. Tough, “Non-Gaussian models for the statistics of scattered waves,” *Advances in Physics*, vol. 37, no. 5, pp. 471–529, 1988.

- [14] A. Balleri, A. Nehorai, and J. Wang, "Maximum likelihood estimation for compound-Gaussian clutter with inverse gamma texture," *IEEE Transactions on Aerospace and Electronic Systems*, vol. 43, no. 2, pp. 775–779, 2007.
- [15] G. V. Weinberg, "Assessing pareto fit to high-resolution high-grazing-angle sea clutter," *Electronics Letters*, vol. 47, no. 8, p. 516, 2011.
- [16] L. Rosenberg and B. Stephen, "Radar detection performance in medium grazing angle X-band sea clutter," Defence Science and Technology Group Edinburgh, South Australia. [Online]. Available: <https://apps.dtic.mil/sti/pdfs/AD1001397.pdf>. [Accessed: 05-Dec-2021].
- [17] A. Mezache, F. Soltani, M. Sahed, and I. Chalabi, "A model for non-Rayleigh sea clutter amplitudes using compound inverse Gaussian distribution," 2013 IEEE Radar Conference (RadarCon13), 2013.
- [18] A. Gouri, A. Mezache, H. Oudira, and A. Bentoumi, "Mixture of compound-Gaussian distributions for radar sea clutter modeling," 2016 4th International Conference on Control Engineering & Information Technology (CEIT), 2016.
- [19] Anastassopoulos, G. A. Lampropoulos, A. Drosopoulos, and N. Rey, "High resolution radar clutter statistics," *IEEE Transactions on Aerospace and Electronic Systems*, vol. 35, no. 1, pp. 43–60, 1999.
- [20] C. W. Helstrom, "Distribution of the sum of clutter and thermal noise," *IEEE Transactions on Aerospace and Electronic Systems*, vol. 36, no. 2, pp. 709–713, 2000.
- [21] S. Watts, "Radar detection prediction in K-distributed sea clutter and thermal noise," *IEEE Transactions on Aerospace and Electronic Systems*, vol. AES-23, no. 1, pp. 40–45, 1987.
- [22] S. Watts, K. D. Ward, and R. J. A. Tough, "The physics and modelling of discrete spikes in radar sea clutter," *IEEE International Radar Conference*, 2005.
- [23] K. D. Ward, "Radar detection performance in sea clutter with discrete spikes," 2002 International Radar Conference (Radar 2002), 2002.
- [24] E. Ollila, D. E. Tyler, V. Koivunen, and H. V. Poor, "Compound-Gaussian clutter modeling with an inverse Gaussian texture distribution," *IEEE Signal Processing Letters*, vol. 19, no. 12, pp. 876–879, 2012.
- [25] M. Greco, F. Gini, and M. Rangaswamy, "Statistical analysis of measured polarimetric clutter data at different range resolutions," *IEE Proceedings - Radar, Sonar and Navigation*, vol. 153, no. 6, p. 473, 2006.

- [26] A. Farina, F. Gini, M. V. Greco, and L. Verrazzani, "High resolution sea clutter data: statistical analysis of recorded live data," *IEE Proceedings - Radar, Sonar and Navigation*, vol. 144, no. 3, p. 121, 1997.
- [27] J. Carretero-Moya, J. Gismero-Menoyo, A. Blanco-del-Campo, and A. Asensio-Lopez, "Statistical analysis of a high-resolution sea clutter database," *IEEE Transactions on Geoscience and Remote Sensing*, vol. 48, no. 4, pp. 2024–2037, 2010.
- [28] M. Farshchian and F. L. Posner, "The Pareto distribution for low grazing angle and high resolution X-band sea clutter," *2010 IEEE Radar Conference*, 2010.
- [29] J. C. Lagarias, J. A. Reeds, M. H. Wright, and P. E. Wright, "Convergence properties of the Nelder–mead simplex method in low dimensions," *SIAM Journal on Optimization*, vol. 9, no. 1, pp. 112–147, 1998.
- [30] A. Mezache, M. Sahed, T. Laroussi, and D. Chikouche, "Two novel methods for estimating the compound K-clutter parameters in presence of thermal noise," *IET Radar, Sonar & Navigation*, vol. 5, no. 9, p. 934, 2011.
- [31] A. Mezache, F. Soltani, M. Sahed, and I. Chalabi, "Model for non-Rayleigh clutter amplitudes using compound inverse Gaussian distribution: an experimental analysis," *IEEE Transactions on Aerospace and Electronic Systems*, vol. 51, no. 1, pp. 142–153, 2015.
- [32] M. Greco, F. Bordoni, and F. Gini, "X-band sea-clutter nonstationarity: influence of long waves," *IEEE Journal of Oceanic Engineering*, vol. 29, no. 2, pp. 269–283, 2004.
- [33] T. J. Nohara and S. Haykin, "Canadian East coast radar trials and the K-distribution," *IEE Proceedings F Radar and Signal Processing*, vol. 138, no. 2, p. 80, 1991.
- [34] E. Conte, A. De Maio, and C. Galdi, "Statistical analysis of real clutter at different range resolutions," *IEEE Transactions on Aerospace and Electronic Systems*, vol. 40, no. 3, pp. 903–918, 2004.
- [35] S. Haykin, C. Krasnor, T. J. Nohara, B. W. Currie, and D. Hamburger, "A coherent dual-polarized radar for studying the ocean environment," *IEEE Transactions on Geoscience and Remote Sensing*, vol. 29, no. 1, pp. 189–191, 1991.
- [36] Y. Dong, "Distribution of X-band high resolution and high grazing angle sea clutter," *United States: Defence Science and Technology Organisation Edinburgh (Australia) Electronic Warfare and Radar Division*, 2006.
- [37] "The McMaster IPIX radar sea clutter database," [Online]. Available: <http://soma.ece.mcmaster.ca/ipix/>. [Accessed: 28-Nov-2021].

- [38] A. Younsi, M. Greco, F. Gini, and A. M. Zoubir, "Performance of the adaptive generalised matched subspace constant false alarm rate detector in non-Gaussian Noise: an experimental analysis," *IET Radar, Sonar & Navigation*, vol. 3, no. 3, p. 195, 2009.
- [39] A. W. Bowman and A. Azzalini, *Applied smoothing techniques for data analysis: the kernel approach with S-Plus illustrations*. Oxford: Clarendon Press, 2004.
- [40] "SNCTOOLS," MEXCDF. [Online]. Available: <http://mexcdf.sourceforge.net/>. [Accessed: 28-Nov-2021].
- [41] L. Rosenberg, D. J. Crisp, and N. J. Stacy, "Analysis of the KK-distribution with medium grazing angle sea clutter," *IET Radar, Sonar & Navigation*, vol. 4, no. 2, p. 209, 2010.
- [42] D. A. Abraham, J. M. Gelb, and A. W. Oldag, "K-Rayleigh mixture model for sparse active sonar clutter," *OCEANS'10 IEEE SYDNEY*, 2010.
- [43] X. Zhou, R. Peng, and C. Wang, "A two-component K-Lognormal mixture model and its parameter estimation method," *IEEE Transactions on Geoscience and Remote Sensing*, vol. 53, no. 5, pp. 2640–2651, 2015.
- [44] M. Barkat, *Signal detection and estimation*. Boston: Artech House, 2005.
- [45] H. Finn, "Adaptive detection mode with threshold control as a function of spatially sampled clutter level estimates," *Rca Rev*, vol. 29, pp. 414-465, 1968.
- [46] V. Hansen and J. Sawyers, "Detectability loss due to 'greatest of' selection in a cell-averaging CFAR," *IEEE Transactions on Aerospace and Electronic Systems*, vol. AES-16, no. 1, pp. 115–118, 1980.
- [47] M. Weiss, "Analysis of some modified cell-averaging CFAR processors in multiple-target situations," *IEEE Transactions on Aerospace and Electronic Systems*, vol. AES-18, no. 1, pp. 102–114, 1982.
- [48] G. V. Trunk, "Range resolution of targets using automatic detectors," *IEEE Transactions on Aerospace and Electronic Systems*, vol. AES-14, no. 5, pp. 750–755, 1978.
- [49] P. P. Gandhi and S. A. Kassam, "Analysis of CFAR processors in nonhomogeneous background," *IEEE Transactions on Aerospace and Electronic Systems*, vol. 24, no. 4, pp. 427–445, 1988.
- [50] S. D. Himonas and M. Barkat, "Automatic censored CFAR detection for nonhomogeneous environments," *IEEE Transactions on Aerospace and Electronic Systems*, vol. 28, no. 1, pp. 286–304, 1992.

- [51] H. Rohling, "Radar CFAR thresholding in clutter and multiple target situations," IEEE Transactions on Aerospace and Electronic Systems, vol. AES-19, no. 4, pp. 608–621, 1983.